

NASA CONTRACTOR REPORT 177435

AMES GRANT  
IN-02  
157096  
P-117

Investigation of Helicopter Rotor Blade/Wake Interactive Impulsive Noise

Dr. S. J. Miley  
Dr. G. F. Hall  
Dr. E. von Lavante

(NASA-CR-177435) INVESTIGATION OF  
HELICOPTER ROTOR BLADE/WAKE INTERACTIVE  
IMPULSIVE NOISE (Texas A&M Univ.) 117 p

N88-28882

CSCL 01A

Unclass

G3/02 0157096

CONTRACT NCA2-OR773-301  
January 1987



**NASA CONTRACTOR REPORT 177435**

**Investigation of Helicopter Rotor Blade/Wake Interactive Impulsive Noise**

Dr. S. J. Miley  
Dr. G. F. Hall  
Dr. E. von Lavante

Prepared for  
Ames Research Center  
under Contract NCA2-OR773-301  
January 1987



National Aeronautics and  
Space Administration

**Ames Research Center**  
Moffett Field, California 94035

## SUMMARY

An analysis of the Tip Aerodynamic/Aeroacoustic Test (TAAT) data was performed to identify possible aerodynamic sources of blade/vortex interaction (BVI) impulsive noise. The identification is based upon correlation of measured blade pressure time histories with predicted blade/vortex intersections for the flight condition(s) where impulsive noise was detected. Due to the location of the recording microphones, only noise signatures associated with the advancing blade were available, and the analysis was accordingly restricted to the first and second azimuthal quadrants.

The results show that the blade tip region is operating transonically in the azimuthal range where previous BVI experiments indicated the impulsive noise source to be. No individual blade/vortex encounter is identifiable in the pressure data, however, there is indication of multiple intersections in the roll-up region which could be the origin of the noise. Discrete blade/vortex encounters are indicated in the second quadrant, however, if impulsive noise was produced here, the directivity pattern would be such that it was not recorded by the microphones. It is demonstrated that the TAAT data base is a valuable resource in the investigation of rotor aerodynamic/aeroacoustic behavior, particularly when coupled with suitable analytical models.

## INTRODUCTION

The objective of the research program was to determine the aerodynamic mechanism of blade/wake interaction impulsive noise. This was to be accomplished through the study of existing flight test rotor blade aerodynamic data and the development of supporting analytical models. The anticipated results were to include a definition of the aerodynamic mechanism of the impulsive noise source and analytical models which would provide the necessary means of developing practical solutions to the problem.

Due to the unavailability of funding to continue the program beyond the first year, the analytical model development tasks were only partially completed. The analysis of the flight test data was completed, however, and is reported in the following.

## ANALYTICAL MODEL DEVELOPMENT

### Free Wake Analysis

Two different free wake model computer codes were acquired and installed on the university Amdahl computer. These are the methods of Crimi<sup>1</sup> and of Sadler<sup>2</sup>. The methods are similar, differing primarily in the model of the tip vortex formation. Sadler utilizes a discrete vortex sheet immediately aft of the blade, switching to a single tip vortex element for the remainder of the wake. Crimi employs a single vortex emanating from the tip. The Crimi method

was selected for this reason, and its demonstrated success in correlating with flight data as shown by Charles<sup>3</sup>.

The current status of the method, identified as TAMUWAKE, is that it is operational, utilizing Crimi's original relations for the strength of the tip vortex segment formed at the respective azimuthal intervals. The azimuthal interval is presently constrained to be no smaller than 10 degrees. The blade aerodynamic loading is determined by simple lifting line theory, utilizing published data from the NACA 0012 airfoil. Resulting blade motion is determined using a rigid blade with specified flapping hinge and stiffness parameters. The TAMUWAKE code was used to generate the blade/wake geometry and azimuthal angle of attack variation plots discussed in the flight test data analysis section.

Improvements which were planned for TAMUWAKE included a vortex dissipation model, reduction in azimuthal segment length to enhance the effective frequency of the blade/vortex encounter modeling, addition of the Operational Load Survey (OLS) airfoil aerodynamic data, and an improved aerodynamic loading analysis method. The program was terminated before these modifications could be made, and TAMUWAKE is presently in its original form

#### Navier-Stokes Solution Method

The objective of this effort was to investigate the aerodynamic mechanism of blade/wake interaction impulsive noise using an "accurate" mathematical model in the form of

the time dependent Navier-Stokes equations. The initial development was for the two-dimensional problem, with extension to three dimensions planned as a future activity.

The Navier-Stokes equations were expressed in nondimensional conservation law form in general body fitted coordinates, then linearized in time, giving the delta form of the original equations, as shown by Steger<sup>4</sup>, among others. After the approximate factorization of the implicit part, the resulting set of equations were discretized in space using central differencing, producing in a block triagonal set of algebraic equations, which were in a form readily amenable to solution.

The treatment of the viscous terms was given special attention. The common approach in solving the Navier-Stokes equations is to neglect the streamwise viscous terms, resulting in the so-called thin layer approximation. The resulting scheme is significantly more efficient. However, it has been shown by Chyu and Kuwahara<sup>5</sup> that in the case of transonic flows, this simplification results in incorrect time history of the shock position and strength. The results obtained using the full Navier-Stokes equations are far superior to the thin shear layer results. Therefore, the full Navier-Stokes equations were used the explicit part of the algorithm. In the implicit part, the simplified thin shear layer terms were used for simplicity.

The method was tested on several steady and unsteady two-dimensional flow geometries. These included prediction of separated laminar and turbulent flows in supersonic

diffusers and nozzles, and the flow about the NACA 0012 airfoil at an angle of attack of 0 degrees. The reference Reynolds numbers varied between  $3 \times 10^5$  and  $9 \times 10^6$ . Generally, good agreement with experimental data and numerical predictions by other authors was achieved.

Based on these results, it was decided to proceed with the computation of the unsteady transonic viscous flow about the helicopter rotor blade approximated by the NACA 0012 airfoil at several moderate angles of attack. It was anticipated that after a fully developed steady state flow was obtained, the two-dimensional component of a vortex would be introduced at various positions relatively close to the airfoil leading edge.

However, the nature of the predicted flow dictated very high computational grid resolution. Unfortunately, it was found that none of the computer systems currently available at Texas A&M University was capable of the high execution speeds required to reach a solution within a practical time period. At the termination of the project, the code was being transferred to the NASA computer system for implementation.

#### Quasi-Steady Transonic Method

A quasi-steady method utilizing the existing TRANDES code is also under development. While having no time dependent representation, it is believed that useful information can be obtained concerning the blade/vortex encounter. The importance of this approach is the low

execution time and cost compared to time accurate procedures. A detailed report of this activity, is given by N. Gwinn<sup>6</sup>.

#### ANALYSIS OF TAAT FLIGHT TEST DATA

Utilizing the DATAMAP system<sup>7</sup>, an analysis of blade pressure data was performed. Based upon a noise data tape provided by the NASA collaborator, the flight condition of 65 knots airspeed and 400 feet-per-minute (fpm) rate of descent was the only consistent wake interaction impulsive noise condition of the TAAT test matrix. Impulsive noise also occurred at the end of the 200 fpm rate of descent condition, but this part of the record was not included in the present DATAMAP file. For comparison purposes, data from the 65 knot airspeed run for 0, 200 fpm and 400 fpm rates of descent were used. These conditions are identified as run numbers 3050, 3051 and 3052 respectively.

To assist in the interpretation of the blade pressure data, results from the free wake analysis TAMUWAKE are provided first. Figures 1-36 show the blades and corresponding predicted tip vortex geometries for the 65 knot airspeed flight condition. The solid-line blade is the instrumented blade, and is the reference for the azimuth position. The tip vortices are given in either solid line or dash line depending on the originating blade. Also, spanwise stations of pressure instrumentation for the 40, 60, 75, 86, 91 and 95 percent radius points are shown on the

solid blade. As discussed previously, the free wake analysis is presently limited to a minimum azimuth increment of 10 degrees. Free wake analysis computed azimuthal angle of attack variations for the 60, 75, 86 and 92 percent radius stations are given in figures 37-44. Figures 37, 39, 41 and 43 show the full 360 degree azimuth variation, while figures 38, 40, 42 and 44 show the same variation in an expanded azimuth scale for the region of interest on the advancing side. Each figure contains five curves, representing rates of descent of 0, 200, 400, 600 and 800 fpm respectively. The variation in angle of attack is largest for the inboard 60 percent station because of the relatively lower local blade velocity in relation to the vortex induced vertical velocity components. The angle of attack variation reduces as one proceeds towards the tip. The blade wake interaction is evident on the advancing side between 40 degrees and 100 degrees azimuth. The requirement for a reduced azimuthal increment model is evident here. The peak angle of attack points near 290 degrees azimuth agree well with blade pressure data, however the details of the local variation (peaks and valleys) were not specifically compared with the pressure data. Using an empirical shock number criterion for comparison with acoustic data, Charles<sup>3</sup> indicates that the Crimi based model free wake analysis tends to be biased towards larger blade/vortex vertical separation than actually exists, i.e., predicted interaction occurs at higher rates of descent than experiment. The calculated angle of attack variations given in figures 37-44

must be viewed with this in mind.

The objective of the analysis of blade pressure data was to identify the possible source(s) of impulsive noise. Previous flight investigations, reported by Charles<sup>3</sup>, supported the possibility of transonic shock waves as the noise source. The approach taken here was to generate the azimuthal variation of specific blade pressures using DATAMAP, and attempt to identify behavior which could be related to the presence of shock waves.

To isolate the behavior responsible for the impulsive noise, the azimuthal variations for run numbers 3050, 3051 and 3052 are graphed together. This provides a comparison of two non-impulsive noise cases (3050 and 3051) with an impulsive noise case (3052). The comparison is also of increasing blade/wake interaction for the 65 knot airspeed condition, i.e., from 3050 to 3052. It was a priori expected to see behavior in the 3052 data distinct from the other two runs.

Blade pressure data for the 75 percent radius station are given in figures 45-62. Azimuthal variations at chordwise stations of 3, 8, and 15 percent on the upper and lower surfaces are shown for the full 360 degree revolution, and for the range 55 degrees to 150 degrees in an expanded scale. The boundary for the critical pressure coefficient is shown as the dash curve. The pressure coefficient at the 3 percent chordwise station will tend to follow the local blade angle of attack, acting similarly to a flow vector probe. Comparing figure 45 with figure 39, the free wake

predicted angle of attack peaks at 270 degrees and 310 degrees azimuth are shown in the pressure data. The peak at 310 degrees occurs only at the higher descent rates for both predicted and experimental cases. There is also the indication that the predicted blade/vortex interaction is biased toward higher descent rates as previously mentioned. Referring to figures 25-32, the angle of attack and pressure peaks correspond to tip vortex interactions at the 75 percent radius blade station. The predicted angle of attack variation between 0 degrees and 130 degrees azimuth is not well defined in the pressure data. However, the pressure data indicates transonic flow near the leading edge on the upper surface between 100 degrees and 150 degrees azimuth. Referring to figures 7-13, the 75 percent station interacts with two vorticities in this azimuth range. Referring to the expanded range plots in figures 51-62, the effects of the different descent rates are seen. There is a pressure fluctuation on both upper and lower surfaces between 60 degree and 110 degrees azimuth. This fluctuation increases with descent rate. There is a much larger pressure fluctuation between 110 degrees and 160 degrees azimuth, however, this fluctuation occurs only on the upper surface, and only for the level flight condition. Figures 7-16 show the blade/wake geometry for this azimuth range. The vortex interaction with the 75 percent radius station is predicted to have passed by 120 degrees azimuth. There is at present no explanation for this pressure fluctuation which is restricted to the upper surface only. There, also

is no evidence of impulsive noise associated with this fluctuation in the measured acoustic data. Based upon previous tests reported by Charles<sup>3</sup>, if impulsive were created by this interaction, its directivity would project forward of the blade in a chordwise direction and, quite possibly, upward. If this interaction is a source of impulsive noise, it has been missed by the relatively limited measurements to date.

Pressure data for the 86 percent radius station are given in figures 63-80. Figures 63-68 show a definite transonic flow region on the upper surface between 40 degrees and 160 degrees azimuth. This is most evident for the 15 percent chordwise station in figure 67. Referring to the corresponding blade/wake geometry, figures 4-16, this behavior does not appear to be the result of a discrete blade/vortex interaction. It is possible, however, that this is due to the roll-up of the wake, i.e., a fixed-wing type vortex flow which exists on the lateral boundaries of the helical wake. The expanded scale plots in figures 69-80 show pressure fluctuations associated with the blade/vortex interactions between 60 degrees and 100 degrees azimuth. The corresponding geometries are given in figures 6-10. As with the 75 percent radius data, the upper surface is most active for the level flight condition, and the lower surface is most active for the 400 fpm rate of descent condition.

Pressure data for the 91 percent radius station are given in figures 81-89. The data are restricted to the upper surface due to the absence of lower surface data from

the DATAMAP file. The transonic flow region on the advancing side is evident. The pressure fluctuations shown in the expanded scale plots, figures 81-89, again show flight condition dependent behavior. There is a large amplitude peak at 15 percent chord for the level flight condition. As the descent rate is increased, higher frequency fluctuations occur earlier in azimuth.

Specific pressure fluctuations were further investigated to search for evidence of wave propagation. The resulting plots are shown in figures 90-101. As in the previous plots, the critical pressure coefficient boundary is represented by the dash curve. Figures 90-93 show a relatively large amplitude fluctuation at the 75 percent radius station which occurs only on the upper surface, and only for the level flight condition. This fluctuation does not correspond to a predicted blade/wake interaction, and no explanation is immediately available. For the 86 percent radius station shown in figures 94-97, the fluctuation coincides with predicted blade/wake interaction geometry. The fluctuation increases in frequency and duration as the rate-of-descent increases. The chordwise extent of the fluctuation coincides with the region of supersonic flow. Examining the relative position of the amplitude peaks in figure 96 suggests that the fluctuation is propagating forward with respect to the blade. The fluctuation also appears on the lower surface, which is fully subsonic, and like the upper surface, indicates forward propagation. At the 91 percent radius station, the fluctuation changes

a multiple disturbance occurs at the 400 fpm rate-of-descent condition. The disturbance also shifts azimuthal position, suggesting that different mechanisms are in effect. Unlike the 86 percent radius station, the activity is restricted to the upper surface. In figures 98 and 100, the disturbance propagation appears to be rearward.

## CONCLUSIONS

Based upon the analysis of blade pressure data, the following conclusions are offered:

1. There is generally good agreement between free wake analysis predicted blade/wake interactions and pressure data indications. As previous experience has shown, the current free wake method tends to predict interactions at higher descent rates than experiment.
2. In comparing the form of the observed pressure fluctuations with flight condition, and correspondingly with the generation of impulsive noise, it appears that the aerodynamic mechanism is a multiple peak disturbance, which may be due to an interaction with the wake roll-up process rather than an encounter with a particular vortex.

3. Blade/wake interaction impulsive noise on the advancing side may be due to an encounter where the vortex is (vorticities are) aligned chordwise with respect to the blade, rather than spanwise. This has important ramifications concerning the direction of current BVI research activity.
4. Experience has shown that blade/wake interaction impulsive noise is highly directional. The other pressure fluctuations identified, particularly those isolated to the upper surface, may be producing impulsive noise which is beaming upward, out of the region where normal observations are made.

In summary, analysis of the TAAT flight test program blade pressure data has identified possible aerodynamic sources of impulsive noise. The identification is based upon correlation with the measured noise producing flight condition(s). Previous experience, reported by Charles<sup>3</sup>, supports the correlation with respect to the azimuthal range where the impulsive noise signal originates. Attention should now be directed to the OLS flight test program, where blade azimuthal position and acoustic data are available with the blade pressure data. It is important now to establish the connection between the observed pressure fluctuations and the impulsive noise signal.

## REFERENCES

1. Crimi, P., "Theoretical Prediction of the Flow in Wake of a Helicopter Rotor," Cornell Aeronautical Laboratory Report Cal BB-1994-S-1, September, 1963.
2. Sadler, S.G., "Development and Application of a Method for Predicting Rotor Free Wake Positions and Resulting Rotor Blade Air Loads," NASA CR-1911, December, 1971.
3. Charles, B.D., "Acoustic Effects of Rotor-Wake Interaction During Low Power Descent," presented at the National Symposium on Helicopter Efficiency, Hartford, Connecticut, March, 1975.
4. Steger, J.L., "Implicit Finite-Difference Simulation of Flow about Arbitrary Two-Dimensional Geometries," AIAA Journal, Vol. 16, July, 1978, pp.679-686.
5. Chyu, W.J., and Kuwahara, K., "Computations of Transonic Flow Over an Oscillating Airfoil with Shock-Induced Separation," AIAA Paper No. 82-0350, 1982.
6. Gwinn, N., "A Quasi-Steady Model of Blade/Vortex Interaction," Aerospace Engineering Department, Texas A&M University, April, 1984.
7. Philbrick, R.B. and Eubanks, A.L., "Operational Loads Survey Data Management System. Volumes I & II," USARTL-TR-78-52A/B, January 1979.

$R/C = -500$   $MU = 0.158$   $PSI = 10$

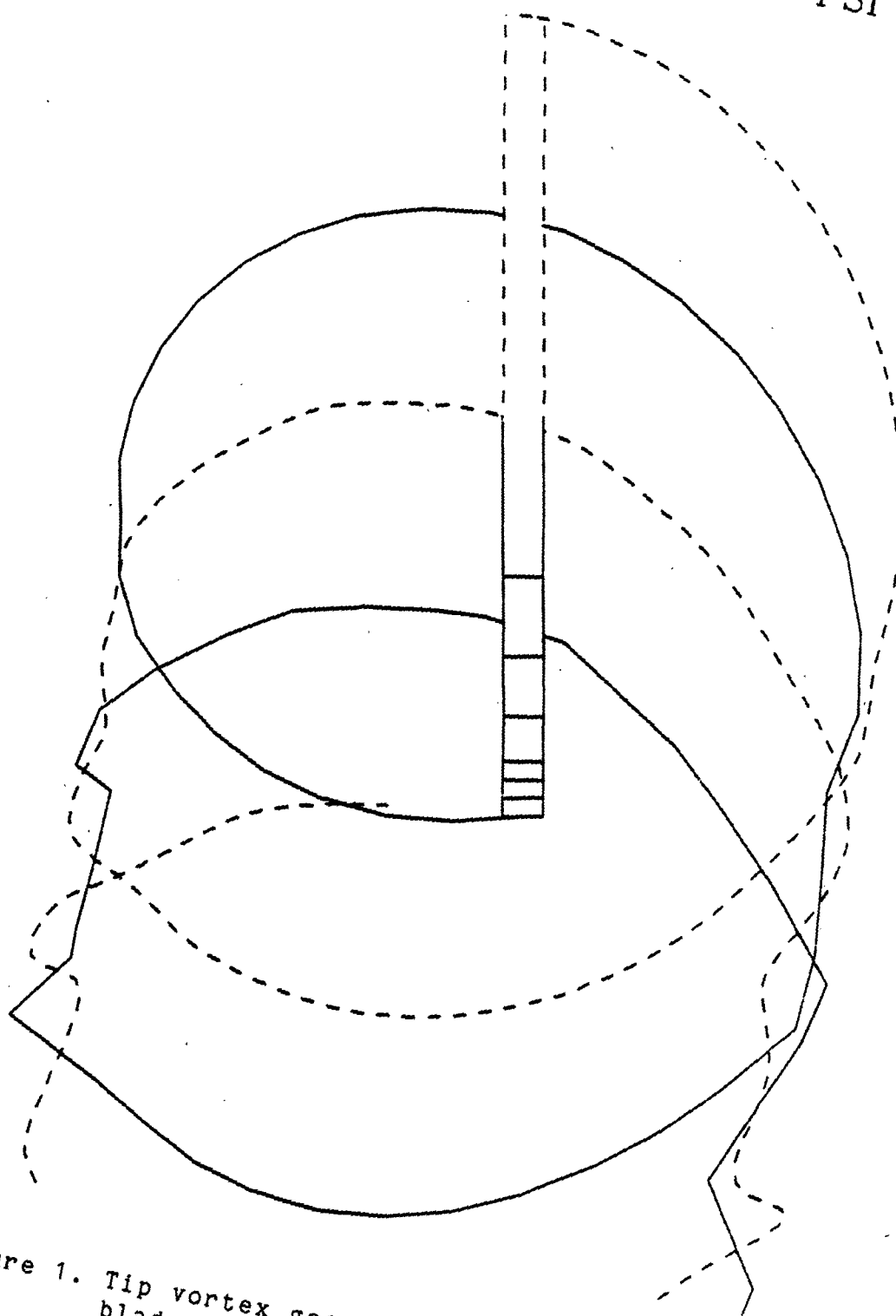


Figure 1. Tip vortex geometry for instrumented  
blade azimuth of 10 degrees.

R/C = -500 MU = 0.158 PSI = 20

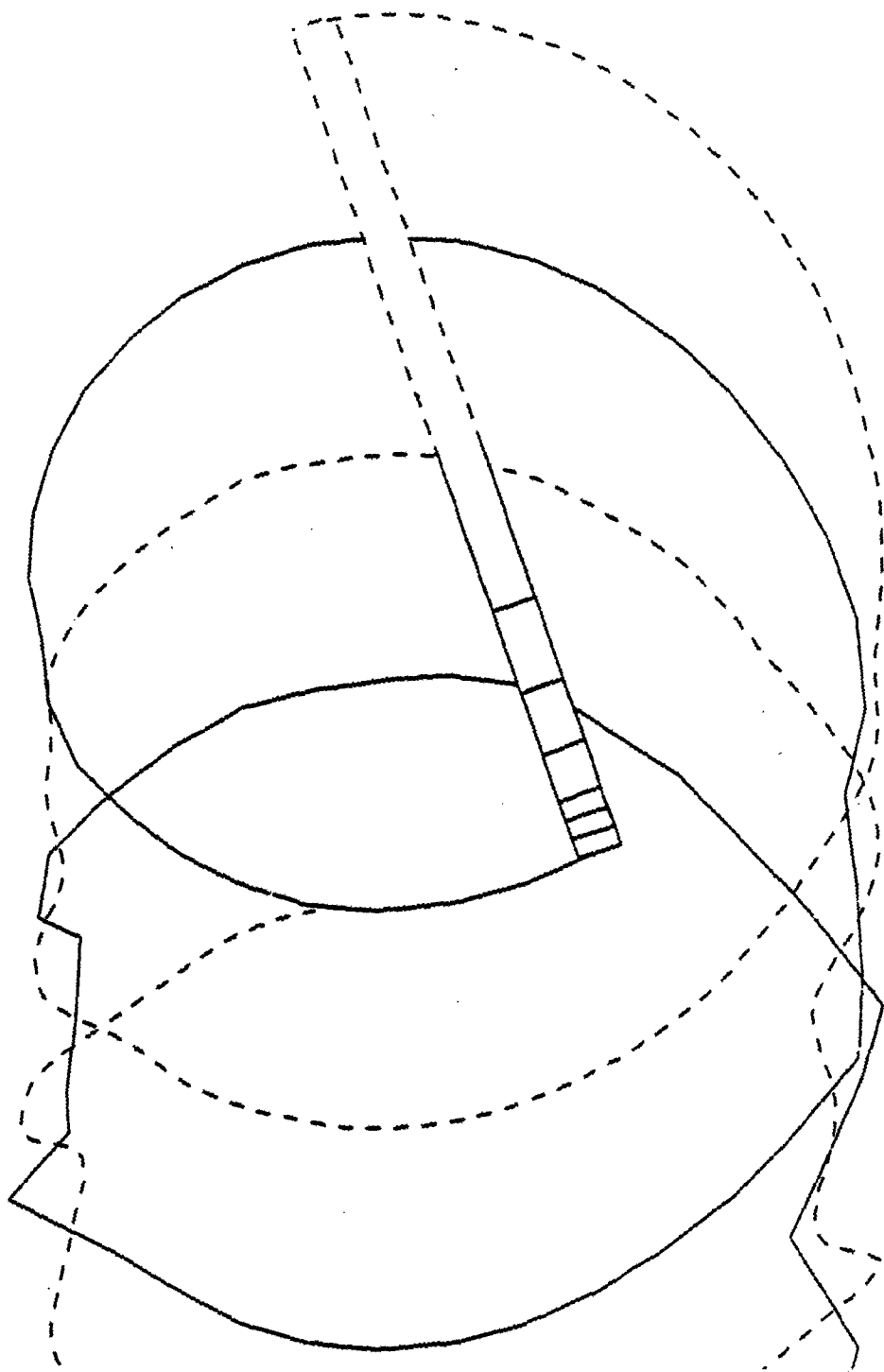


Figure 2. Tip vortex geometry for instrumented  
blade azimuth of 20 degrees.

$R/C = -500$  MU = 0.158 PSI = 30

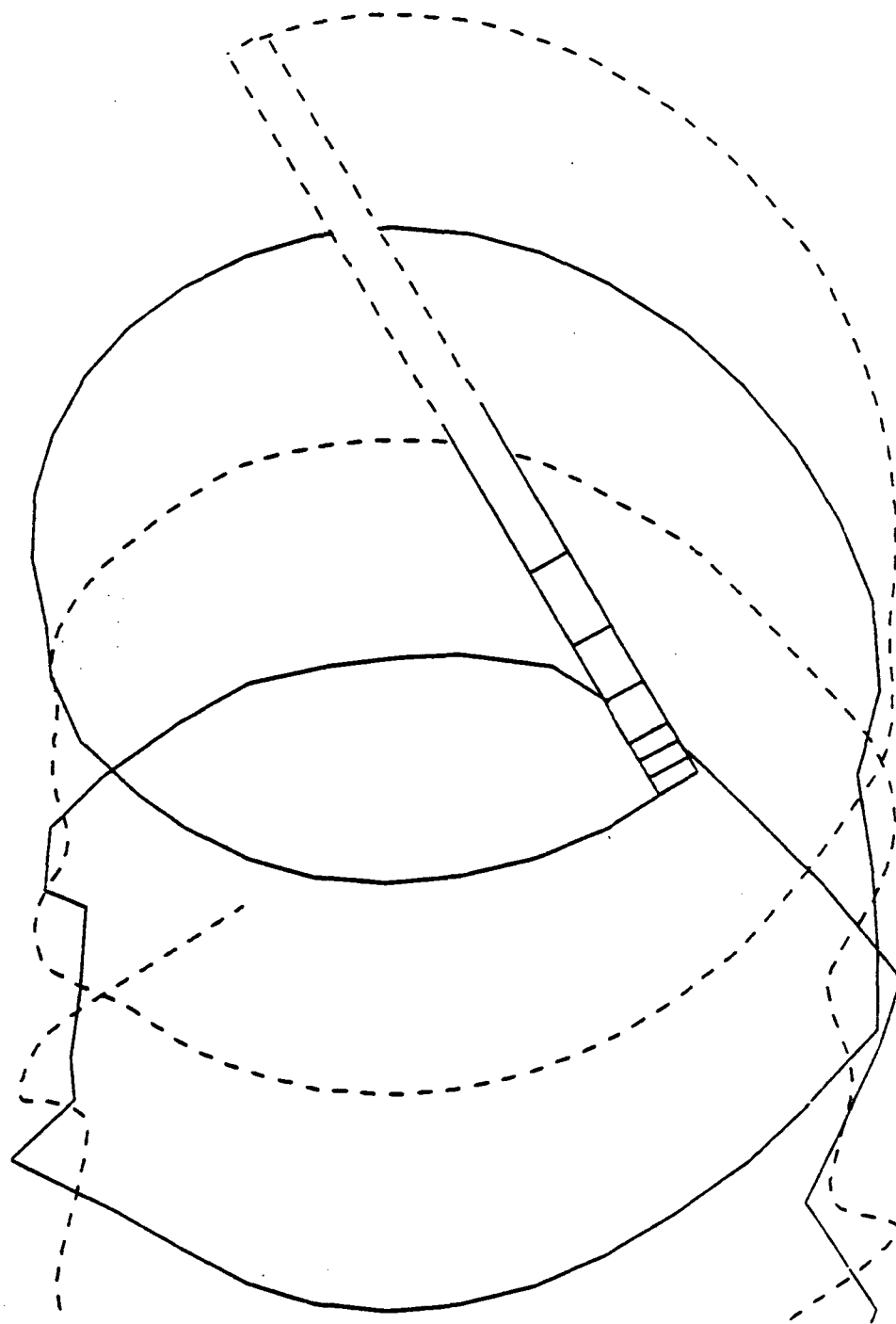


Figure 3. Tip vortex geometry for instrumented blade azimuth of 30 degrees.

$R/C = -500$  MU = 0.158 PSI = 40

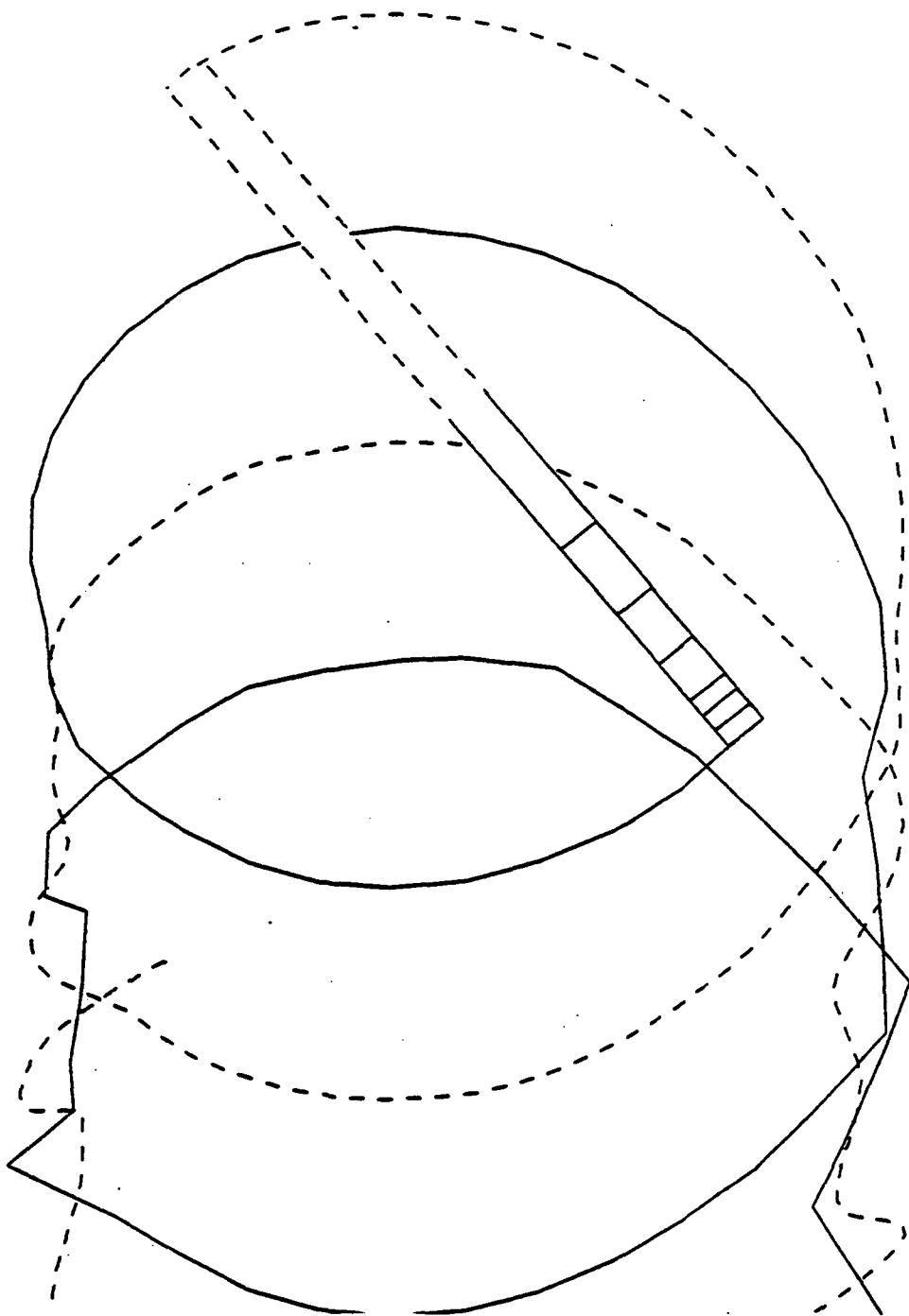


Figure 4. Tip vortex geometry for instrumented blade azimuth of 40 degrees.

$R/C = -500$   $MU = 0.158$   $PSI = 50$

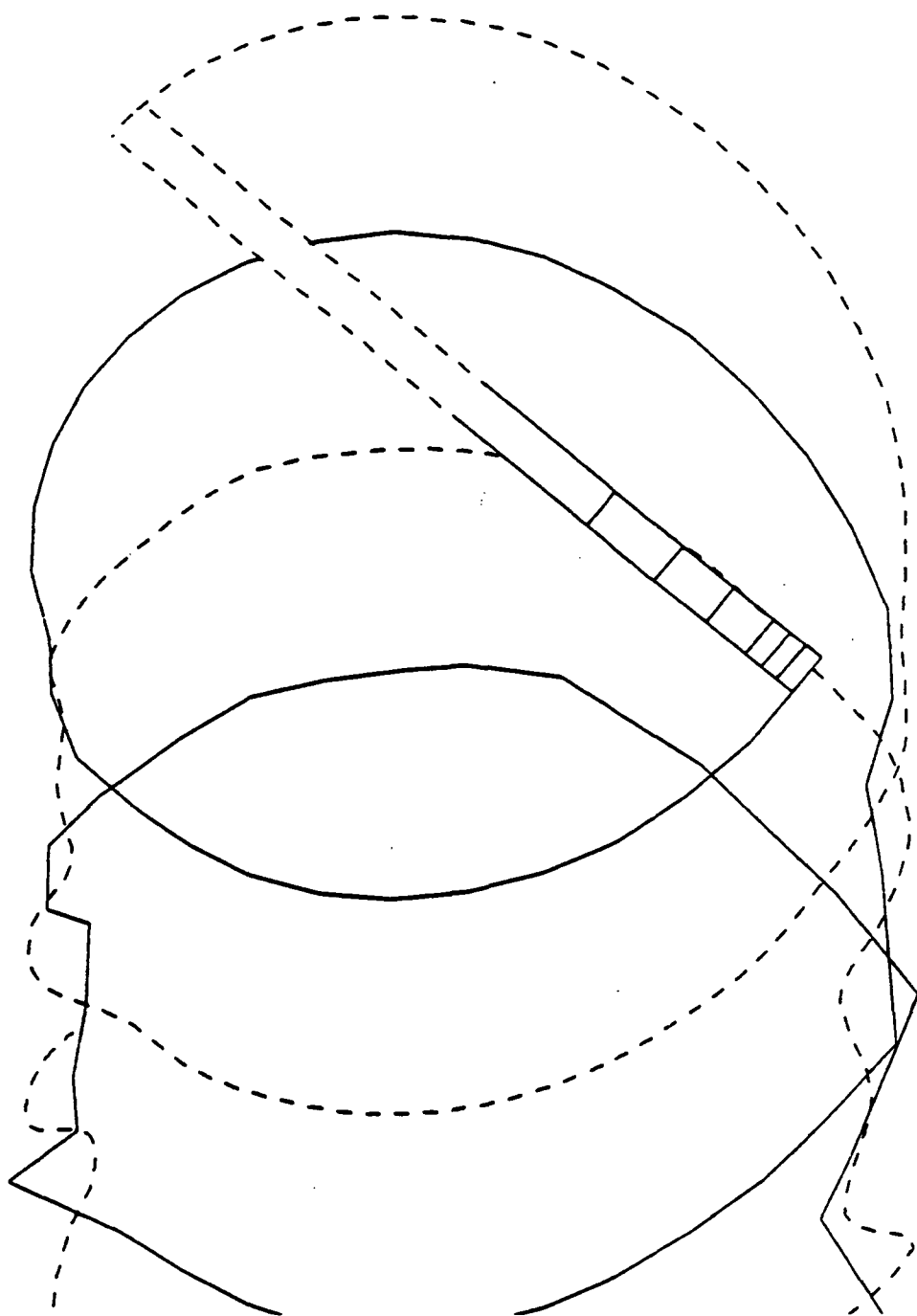


Figure 5. Tip vortex geometry for instrumented blade azimuth of 50 degrees.

$R/C = -500$  MU = 0.158 PSI = 60

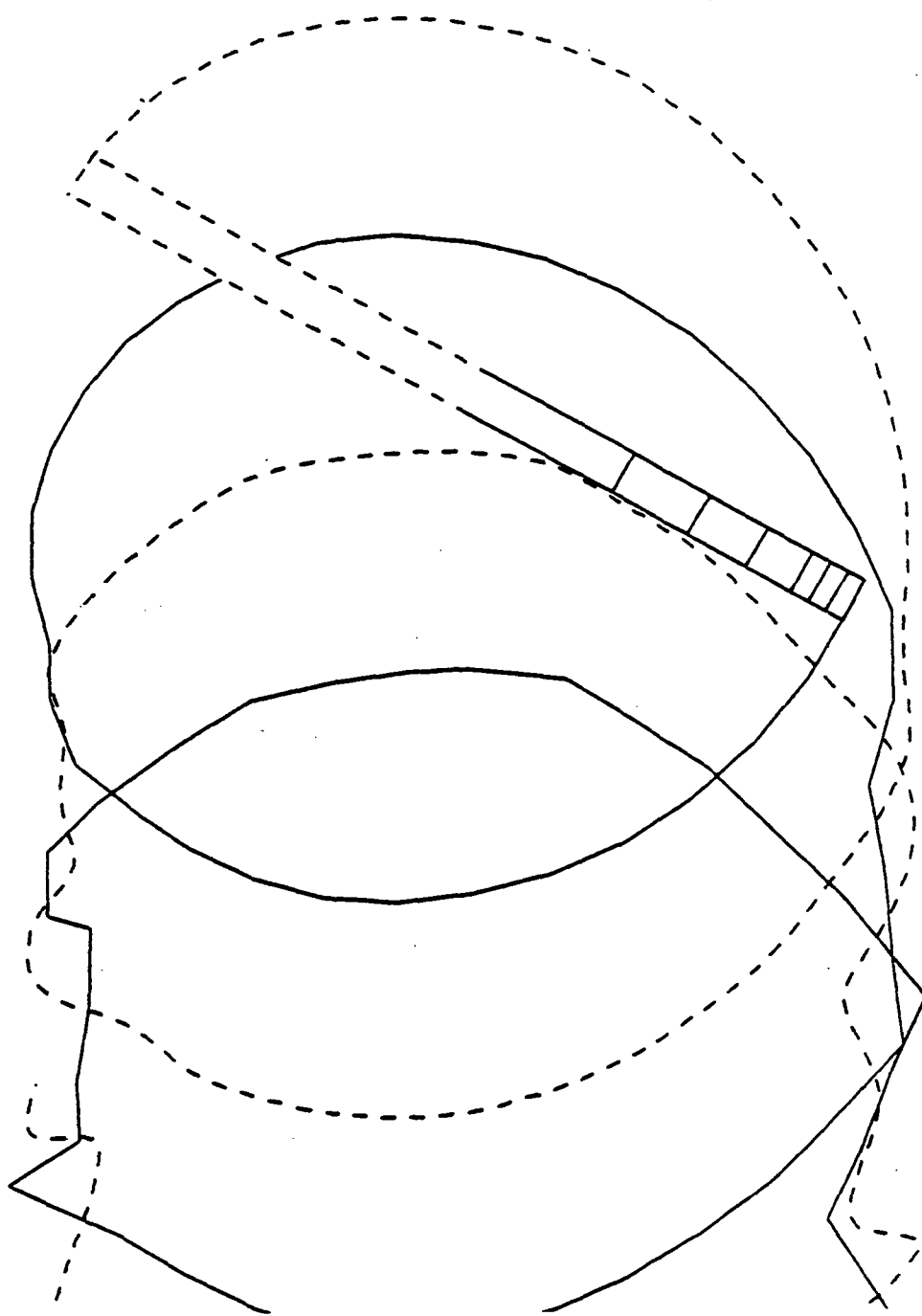


Figure 6. Tip vortex geometry for instrumented blade azimuth of 60 degrees.

R/C = -500 MU = 0.158 PSI = 70

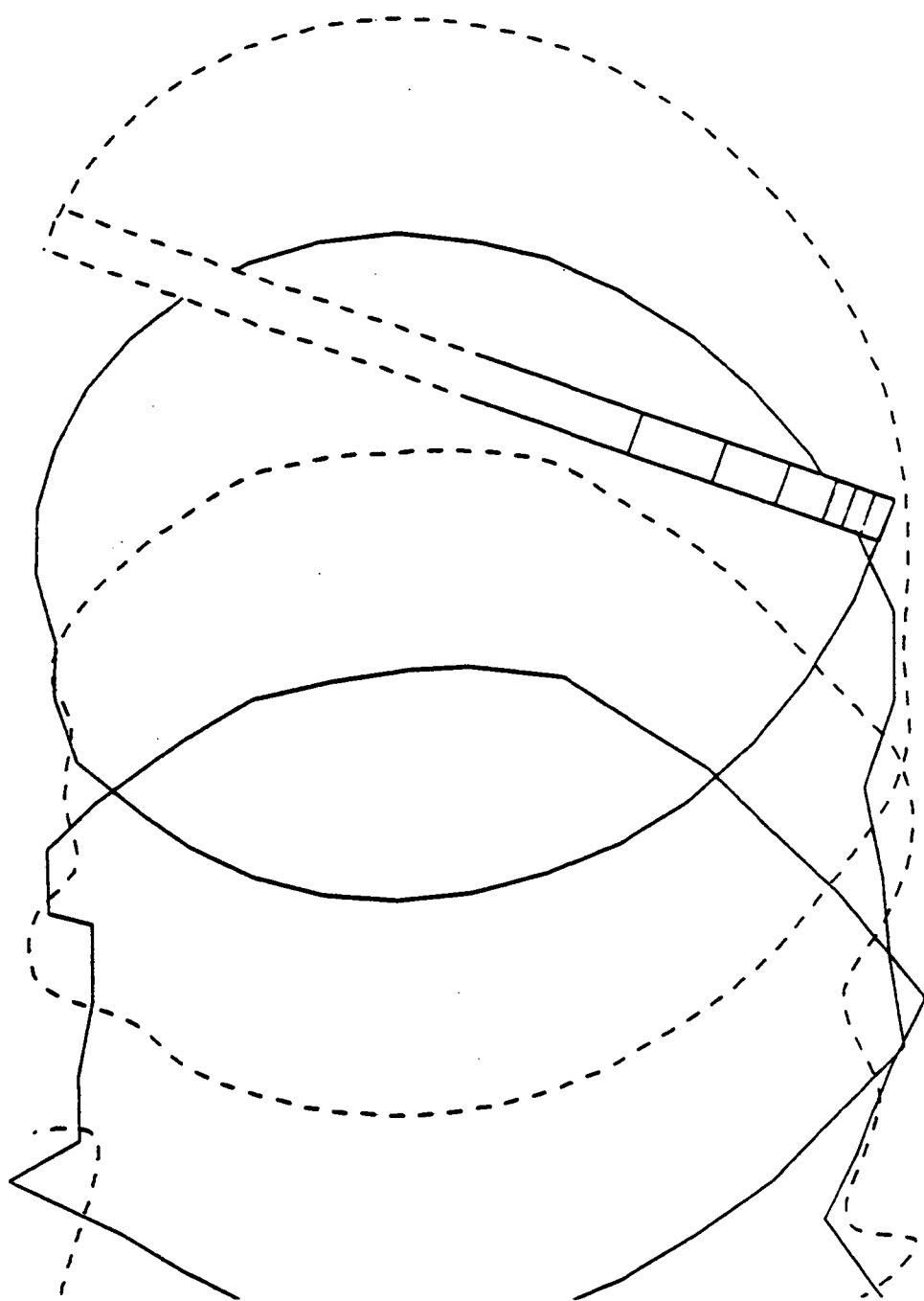


Figure 7. Tip vortex geometry for instrumented blade azimuth of 70 degrees.

$R/C = -500$   $MU = 0.158$   $PSI = 80$

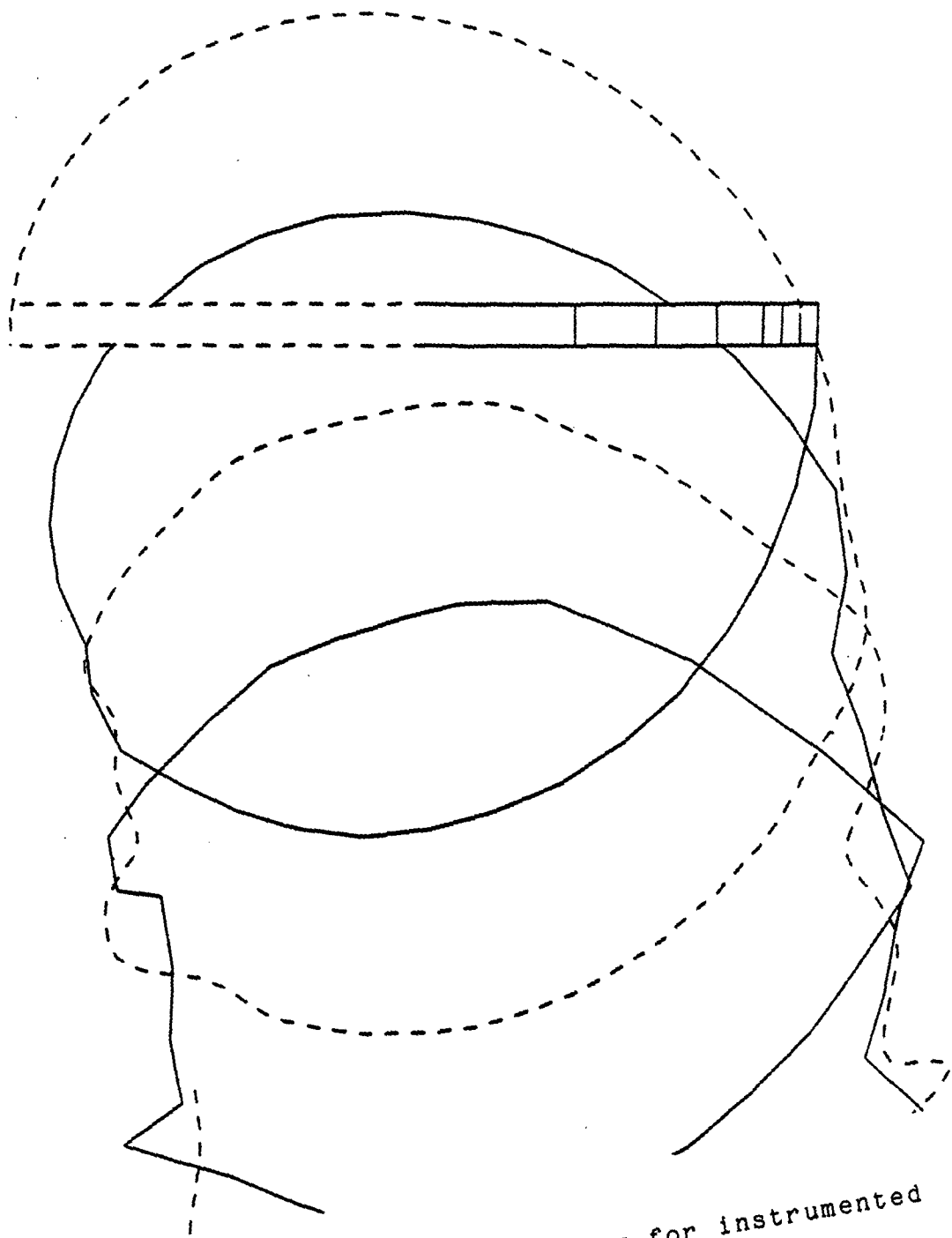


Figure 8. Tip vortex geometry for instrumented  
blade azimuth of 80 degrees.

R/C = -500 MU = 0.158 PSI = 90

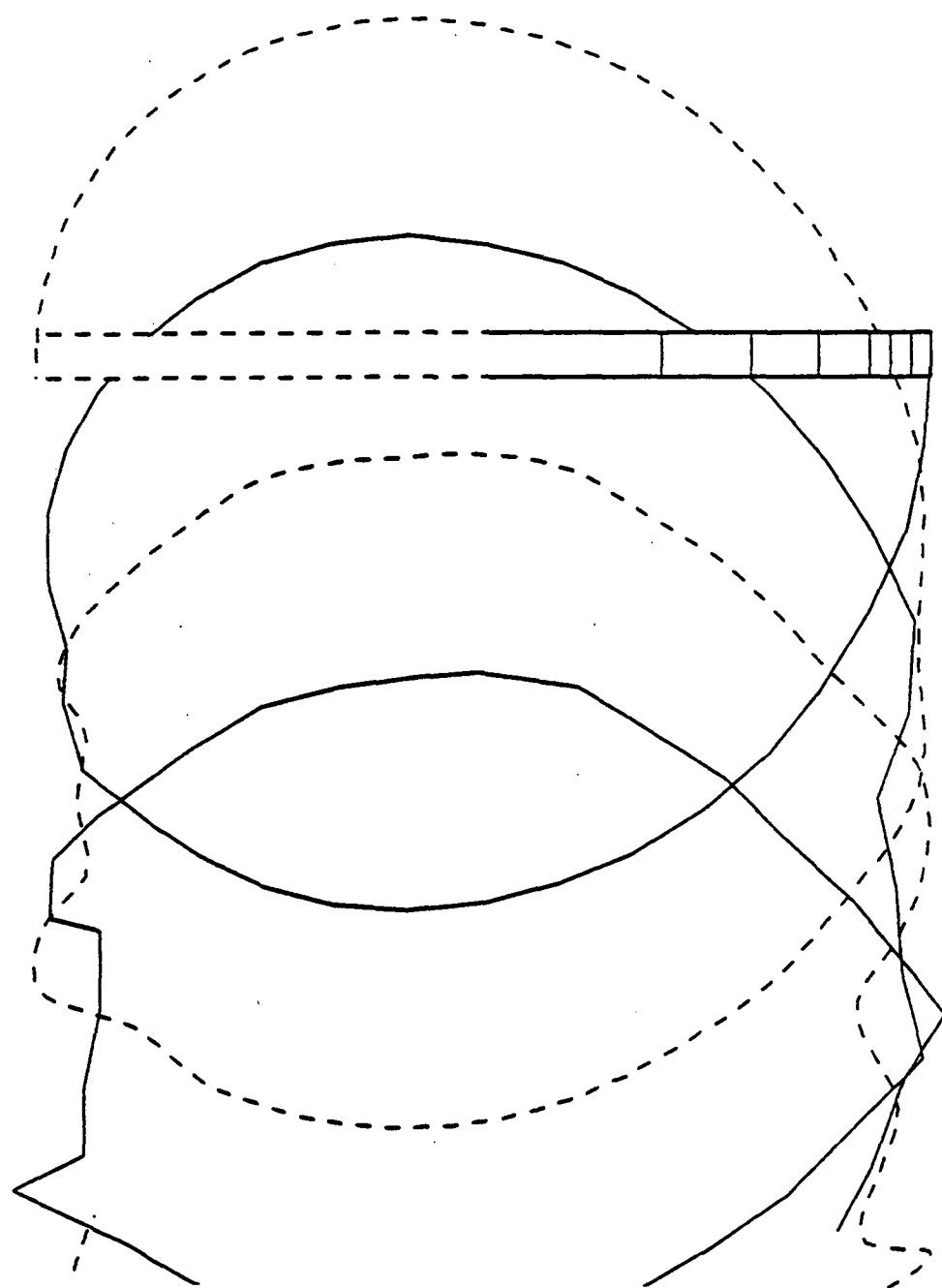


Figure 9. Tip vortex geometry for instrumented blade azimuth of 90 degrees.

$R/C = -500$   $MU = 0.158$   $PSI = 100$

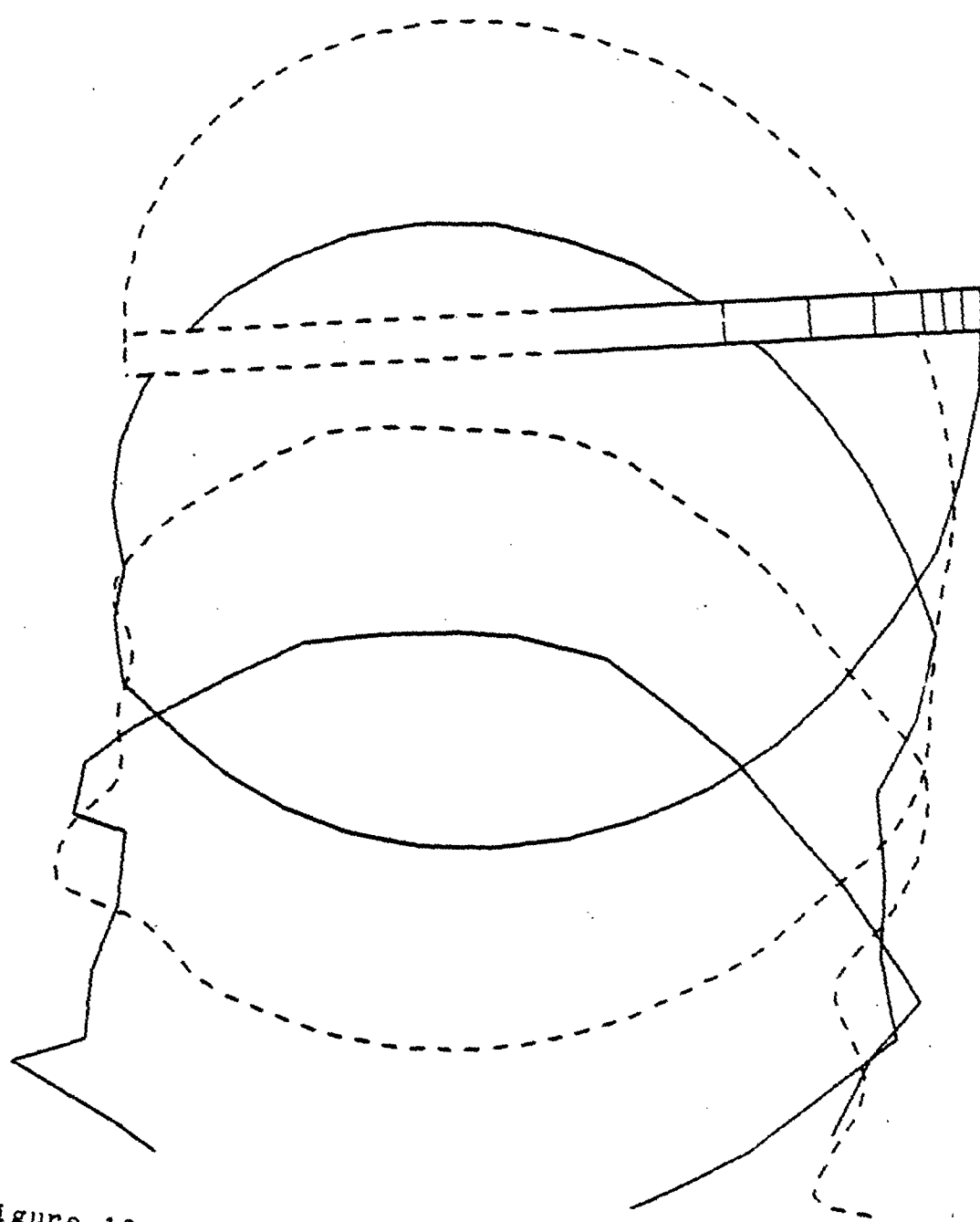


Figure 10. Tip vortex geometry for instrumented blade azimuth of 100 degrees.

R/C = -500 MU = 0.158 PSI = 110

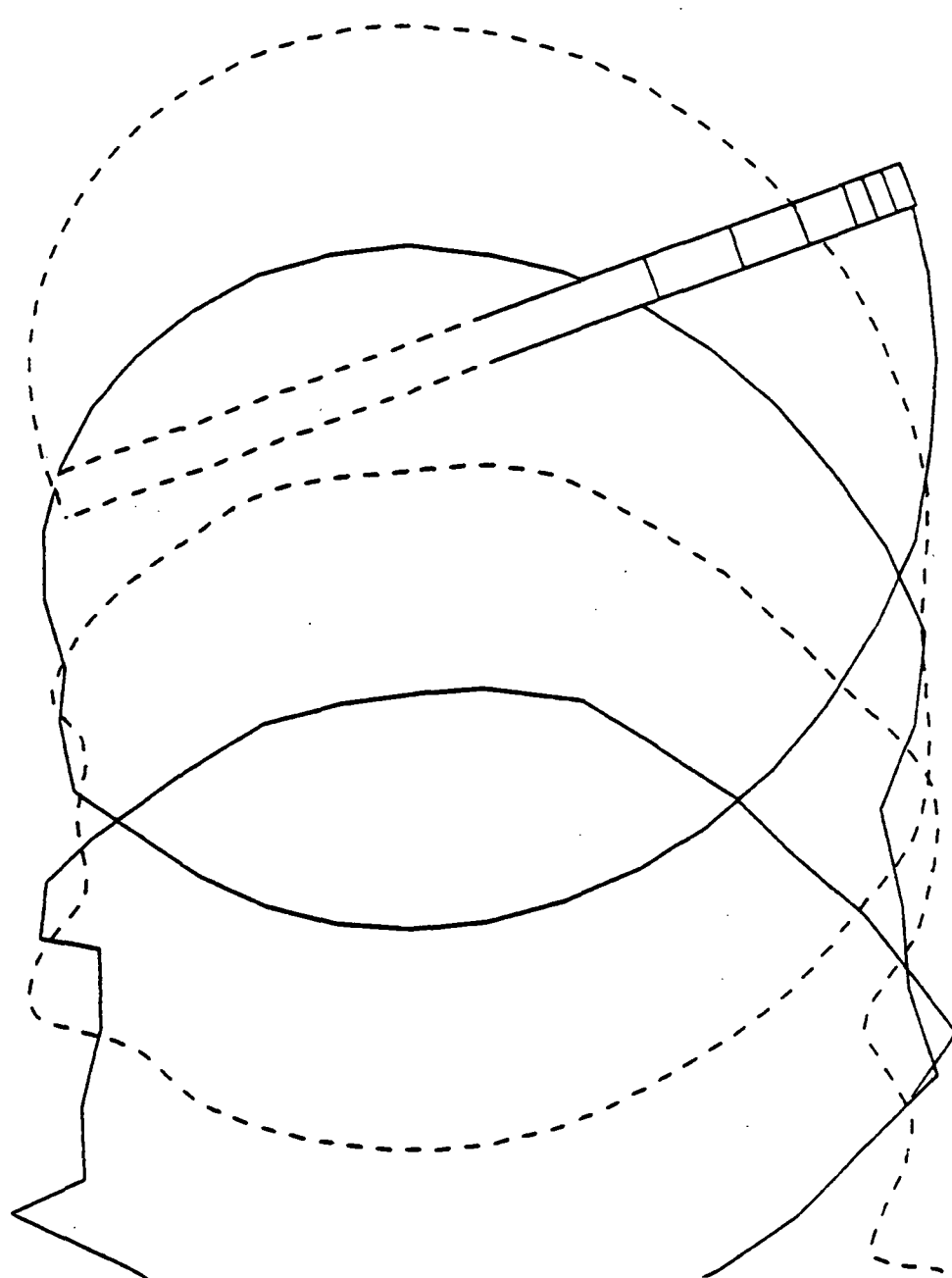


Figure 11. Tip vortex geometry for instrumented blade azimuth of 110 degrees.

$R/C = -500$  MU = 0.158 PSI = 120

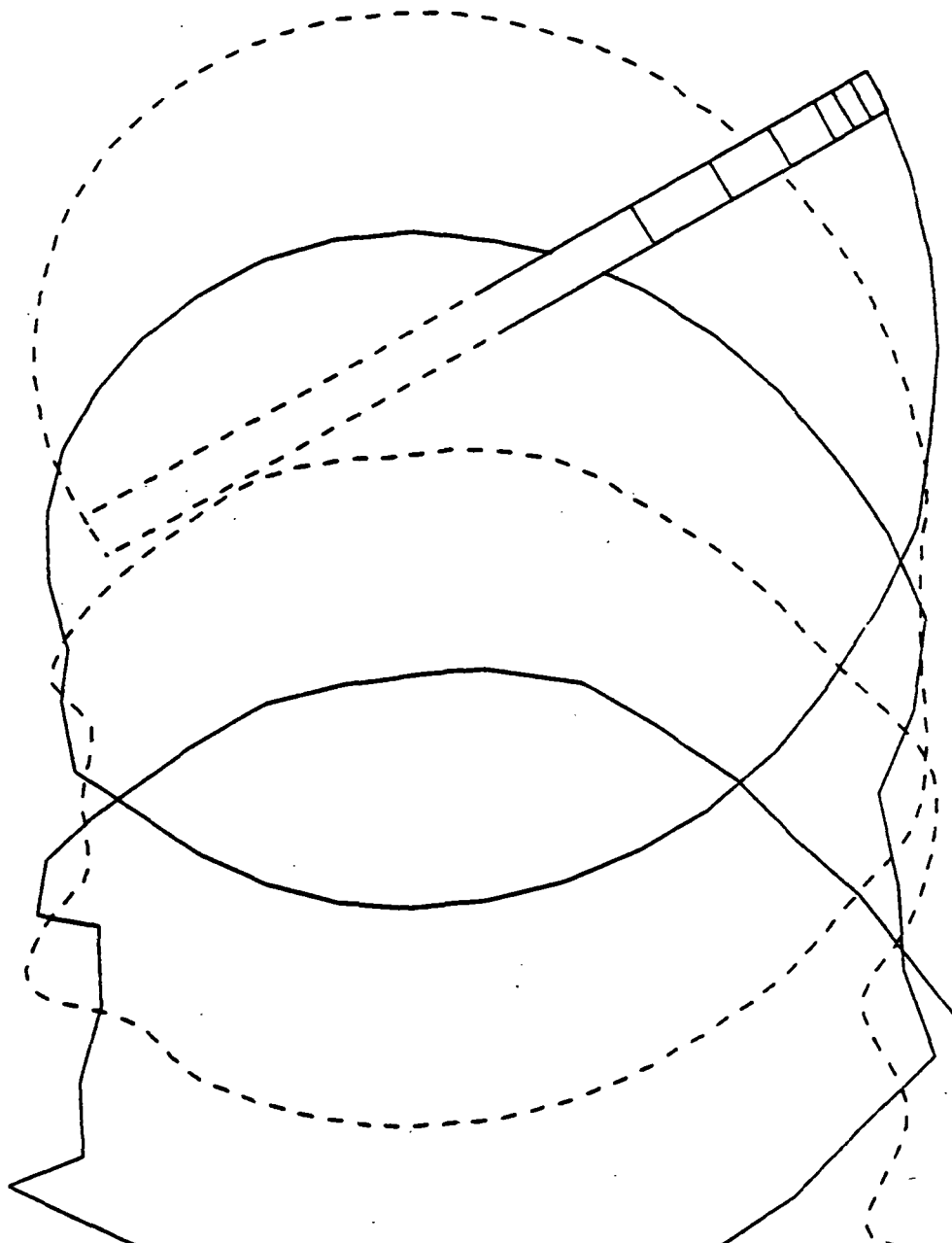


Figure 12. Tip vortex geometry for instrumented blade azimuth of 120 degrees.

R/C = -500 MU = 0.158 PSI = 130

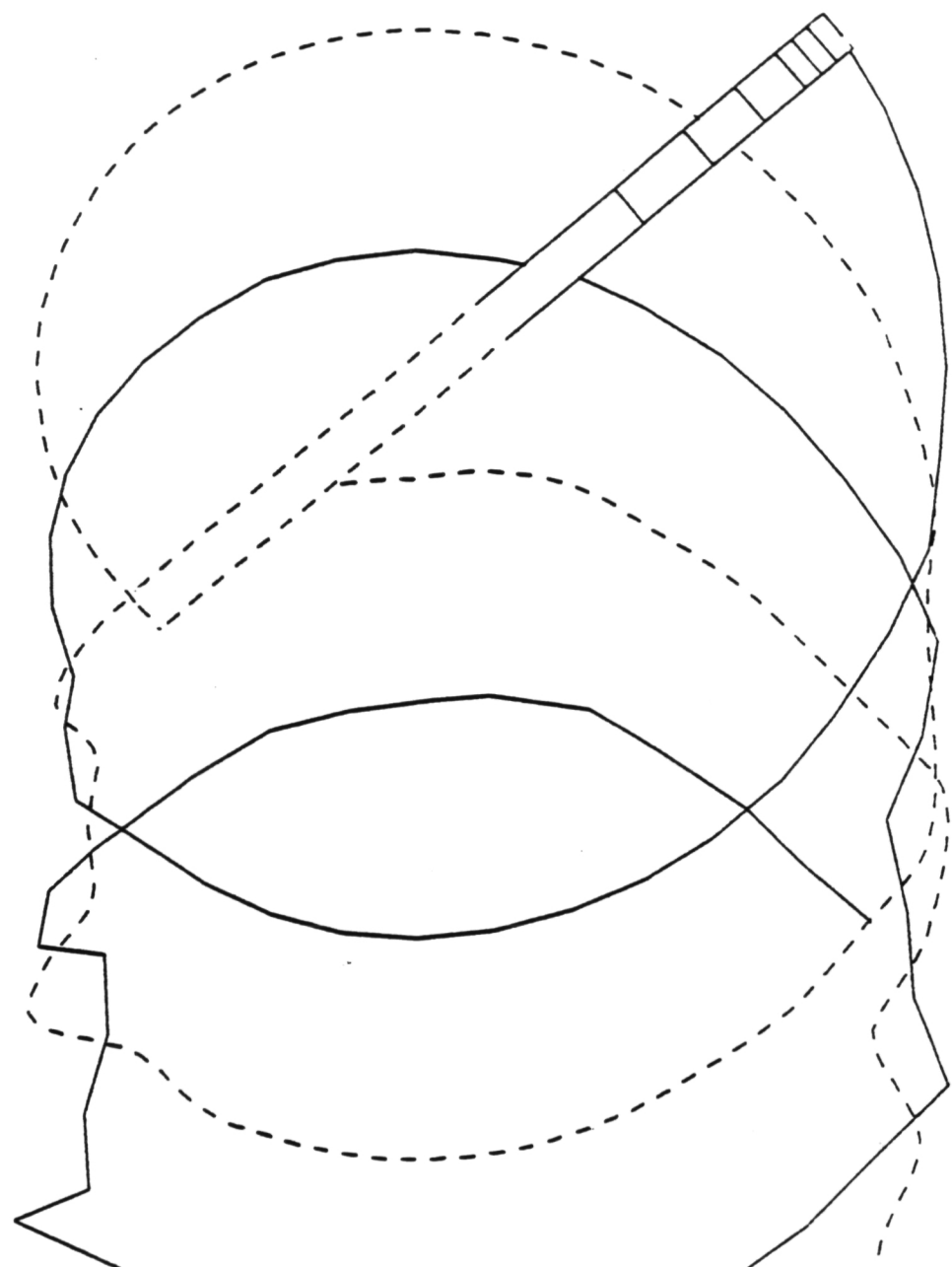


Figure 13. Tip vortex geometry for instrumented blade azimuth of 130 degrees.

$R/C = -500$   $MU = 0.158$   $PSI = 140$

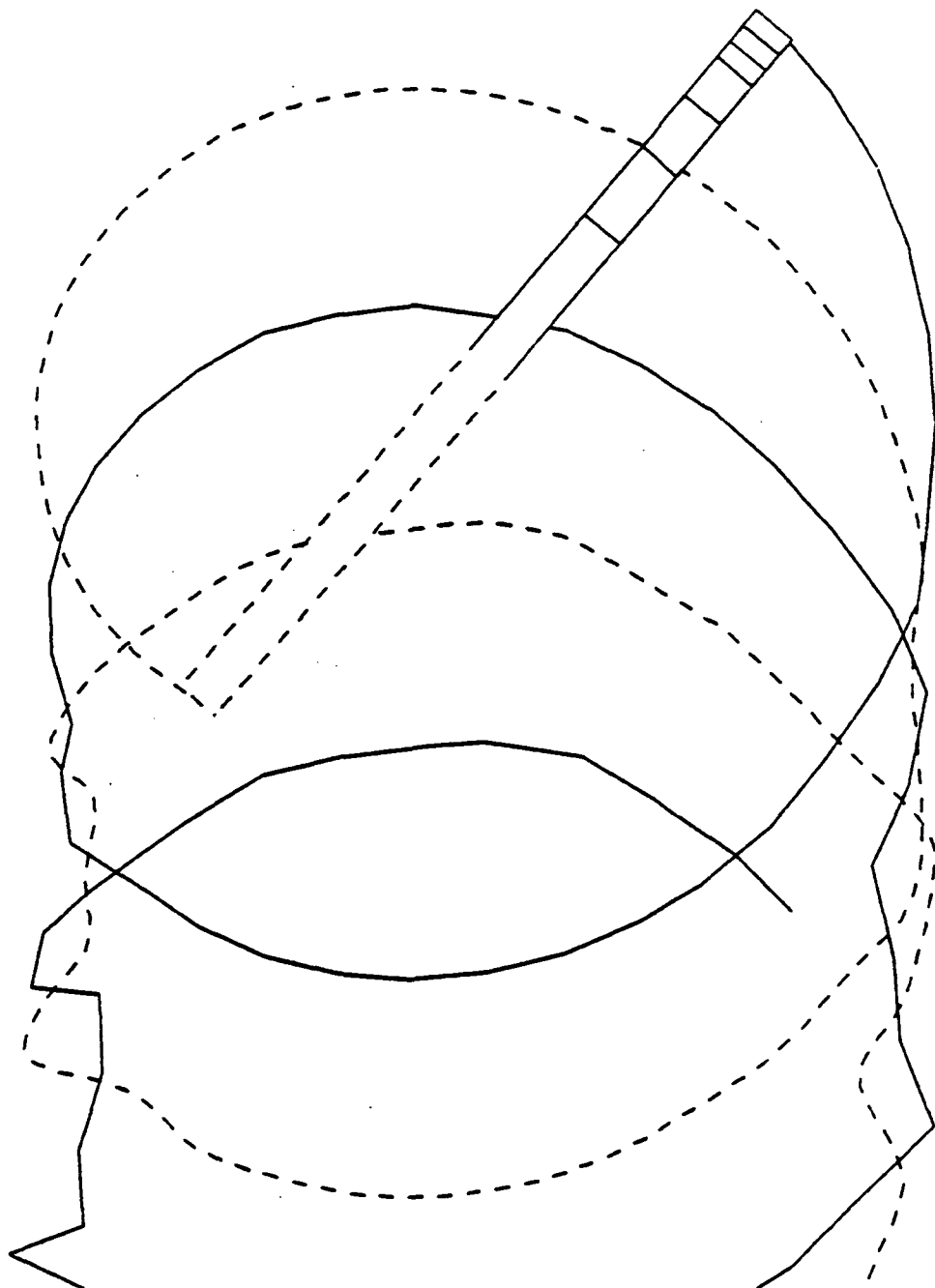


Figure 14. Tip vortex geometry for instrumented blade azimuth of 140 degrees.

R/C = -500 MU = 0.158 PSI = 150

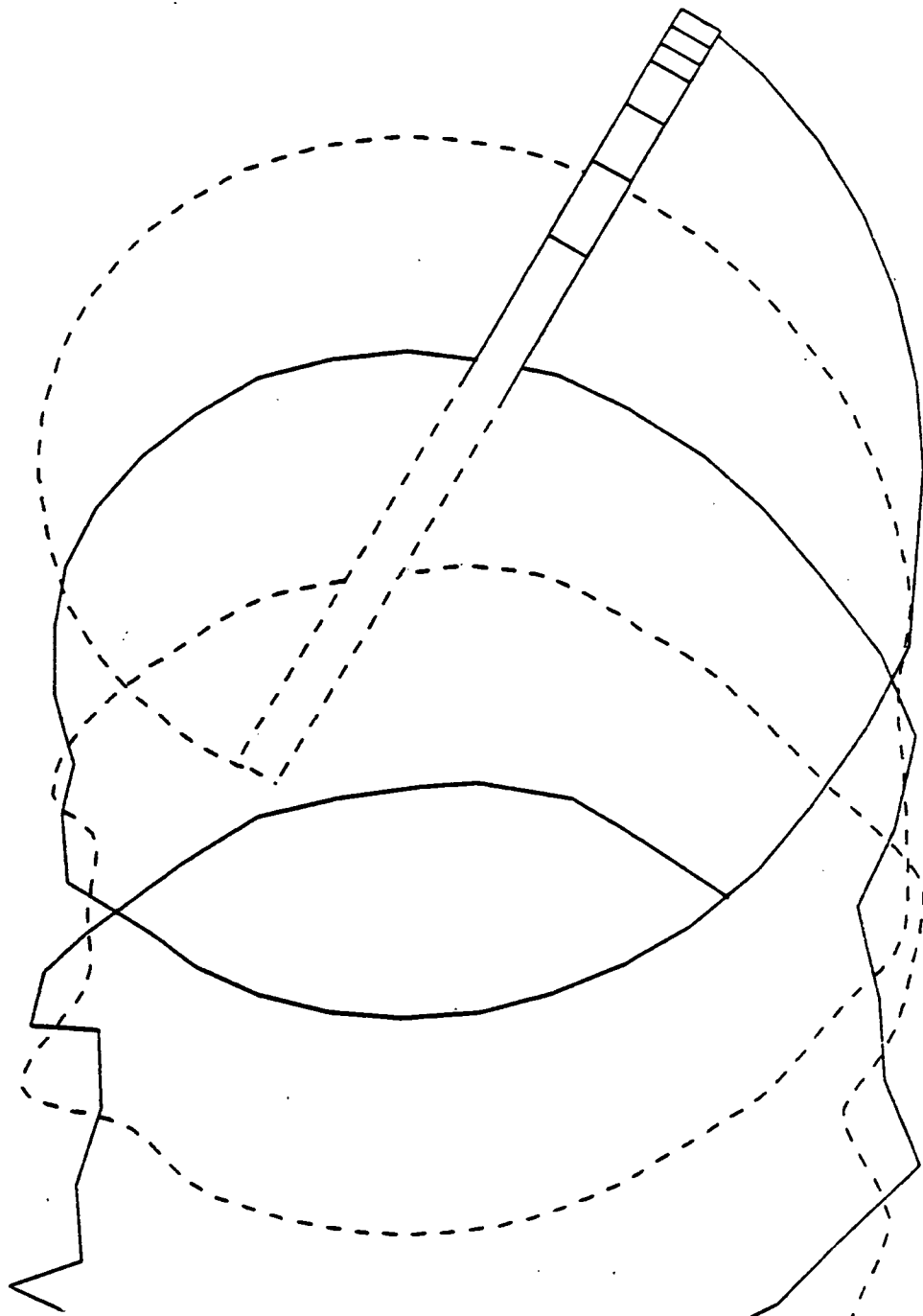


Figure 15. Tip vortex geometry for instrumented blade azimuth of 150 degrees.

$R/C = -500$  MU = 0.158 PSI = 160

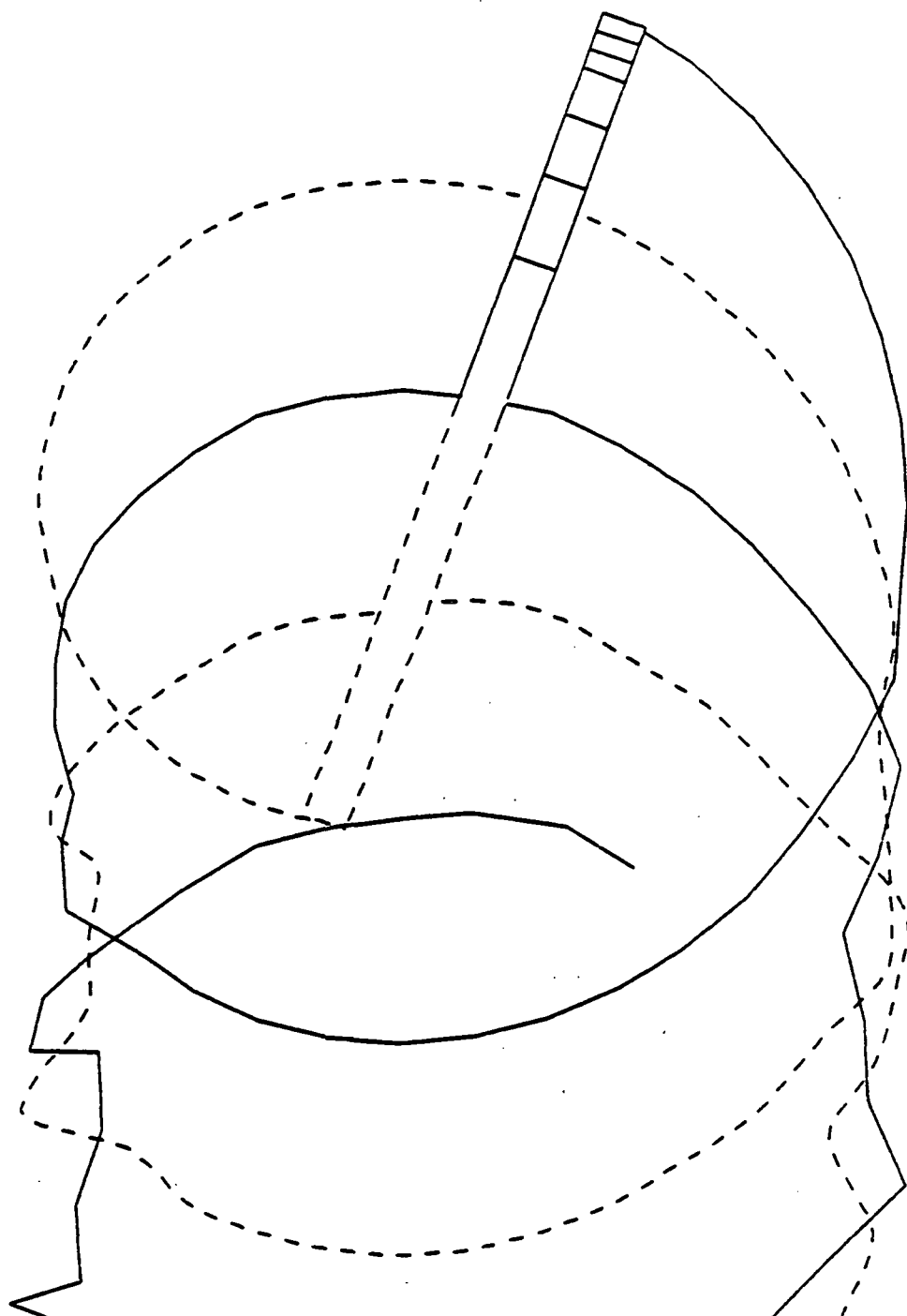


Figure 16. Tip vortex geometry for instrumented blade azimuth of 160 degrees.

$R/C = -500$   $MU = 0.158$   $PSI = 170$

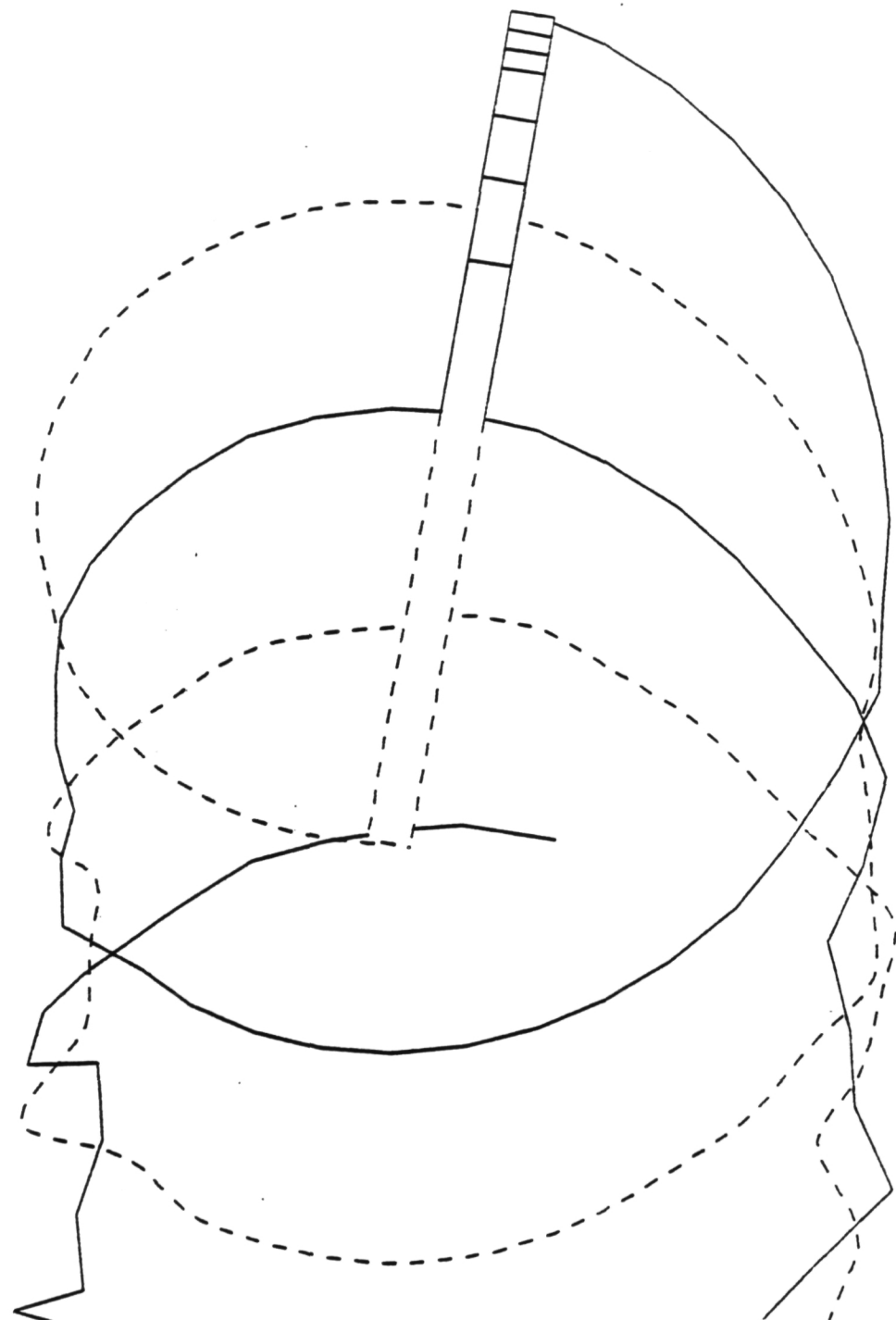


Figure 17. Tip vortex geometry for instrumented blade azimuth of 170 degrees.

$R/C = -500$  MU = 0.158 PSI = 180

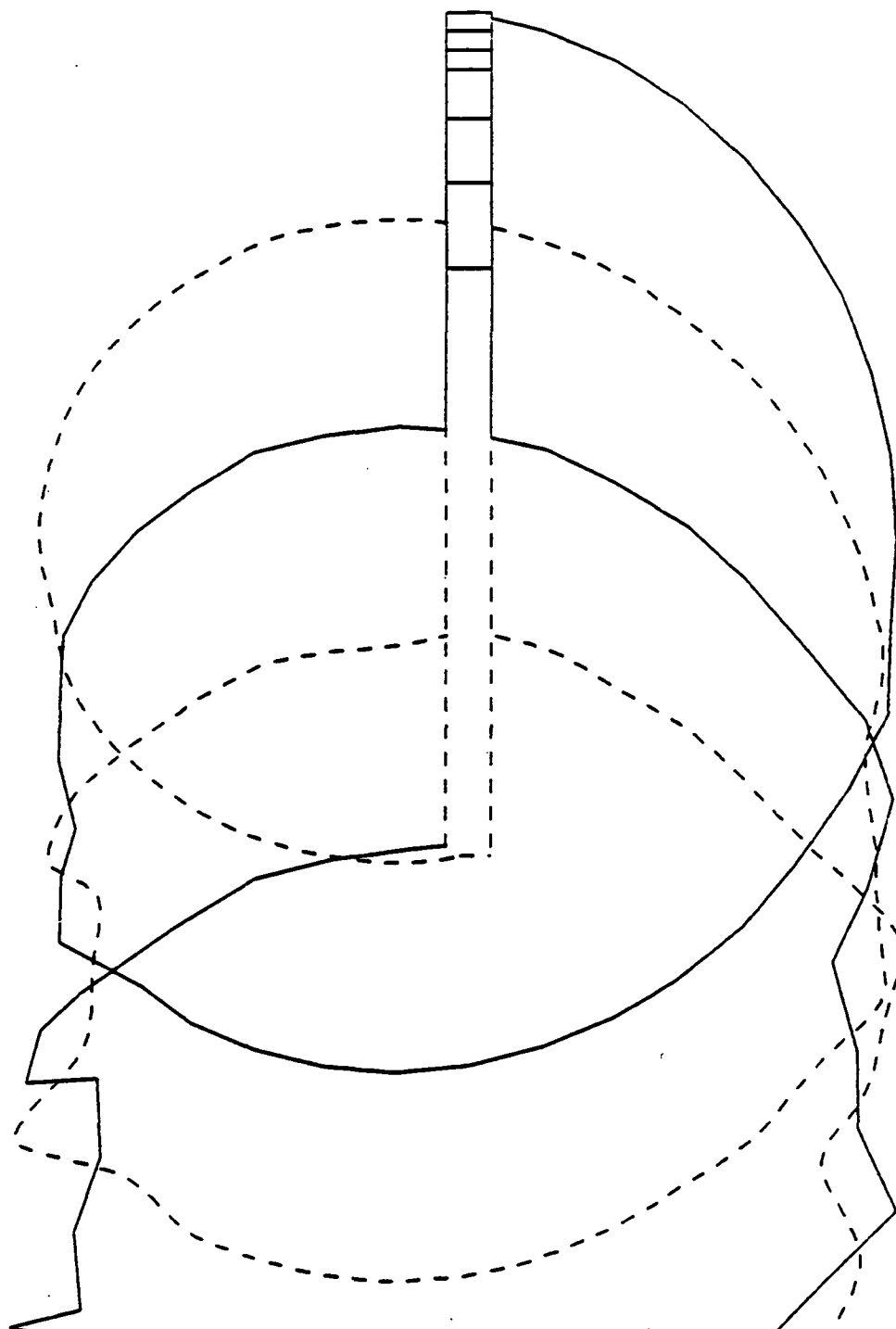


Figure 18. Tip vortex geometry for instrumented blade azimuth of 180 degrees.

$R/C = -500$  MU = 0.158 PSI = 190

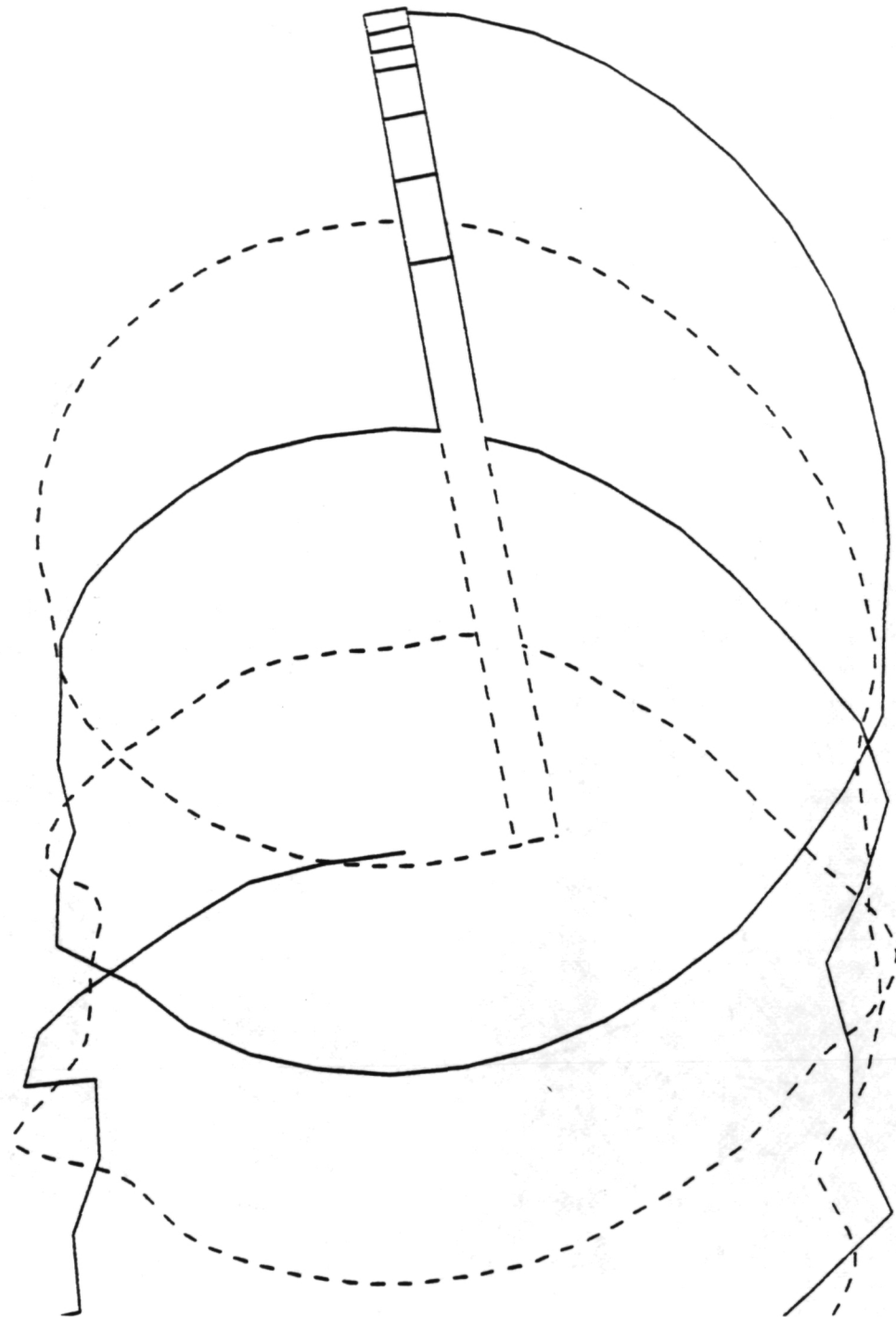


Figure 19. Tip vortex geometry for instrumented blade azimuth of 190 degrees.

$R/C = -500$  MU = 0.158 PSI = 200

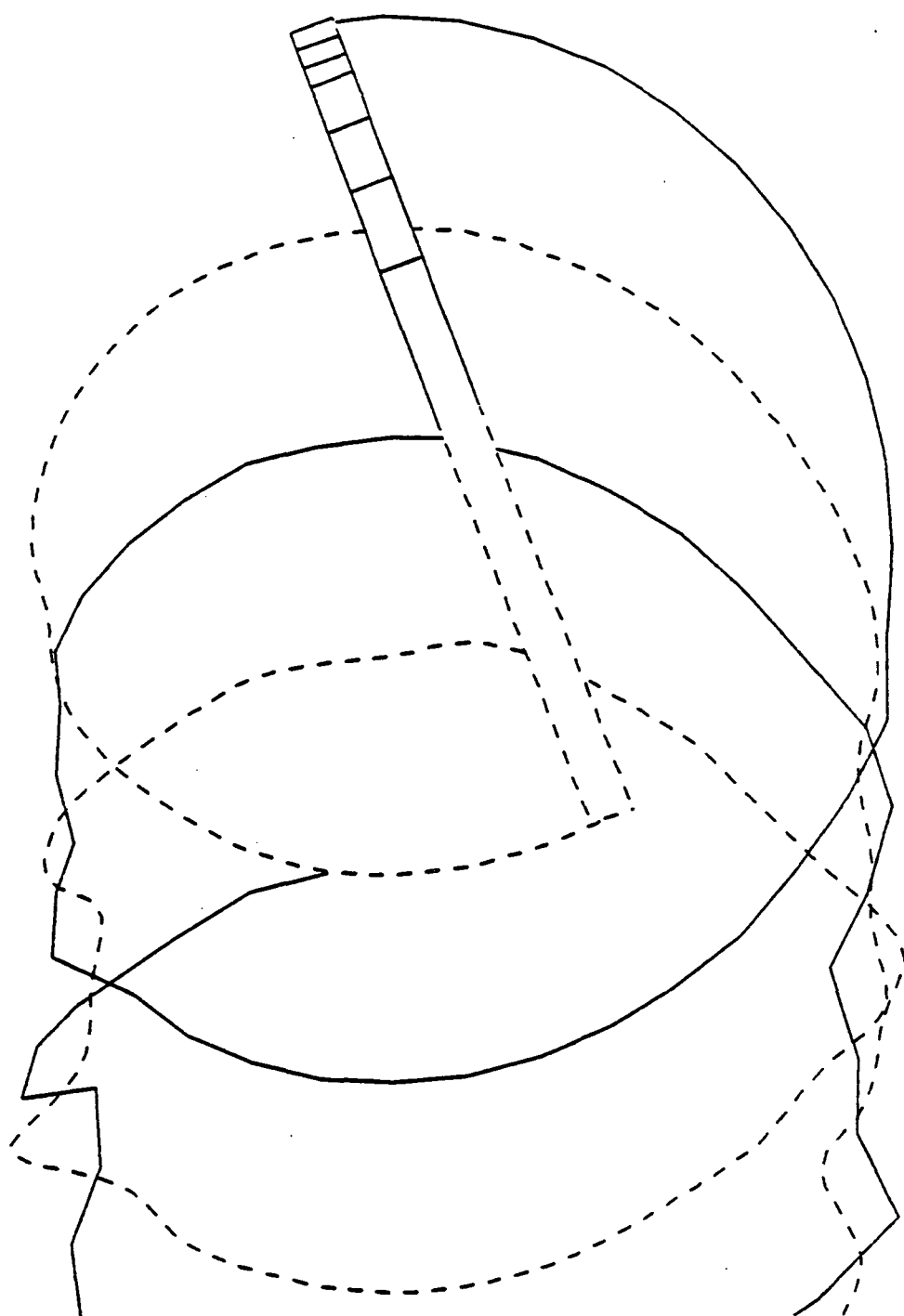


Figure 20. Tip vortex geometry for instrumented blade azimuth of 200 degrees.

R/C = -500 MU = 0.158 PSI = 210

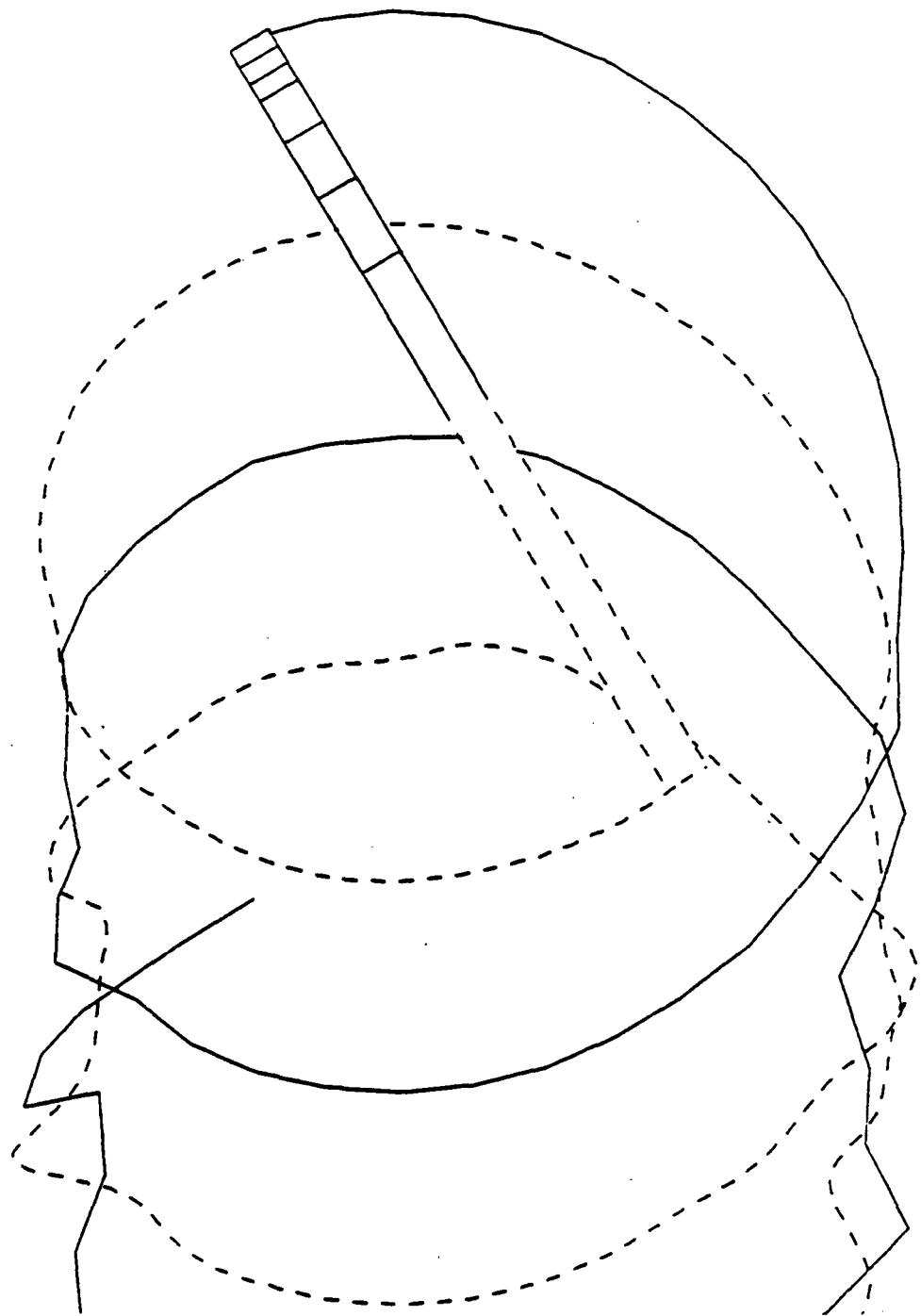


Figure 21. Tip vortex geometry for instrumented blade azimuth of 210 degrees.

$R/C = -500$  MU = 0.158 PSI = 220

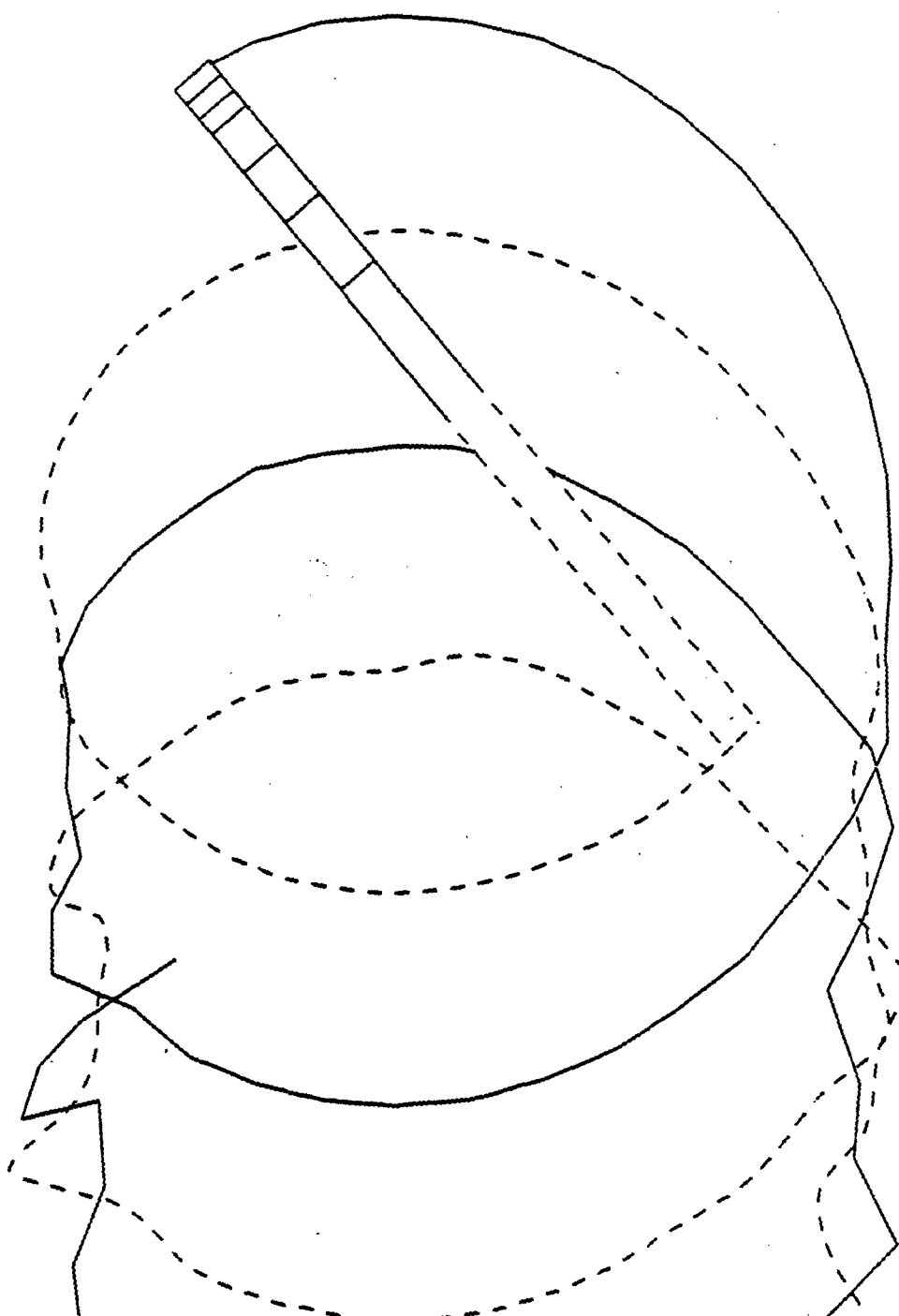


Figure 22. Tip vortex geometry for instrumented blade azimuth of 220 degrees.

R/C = -500 MU = 0.158 PSI = 230

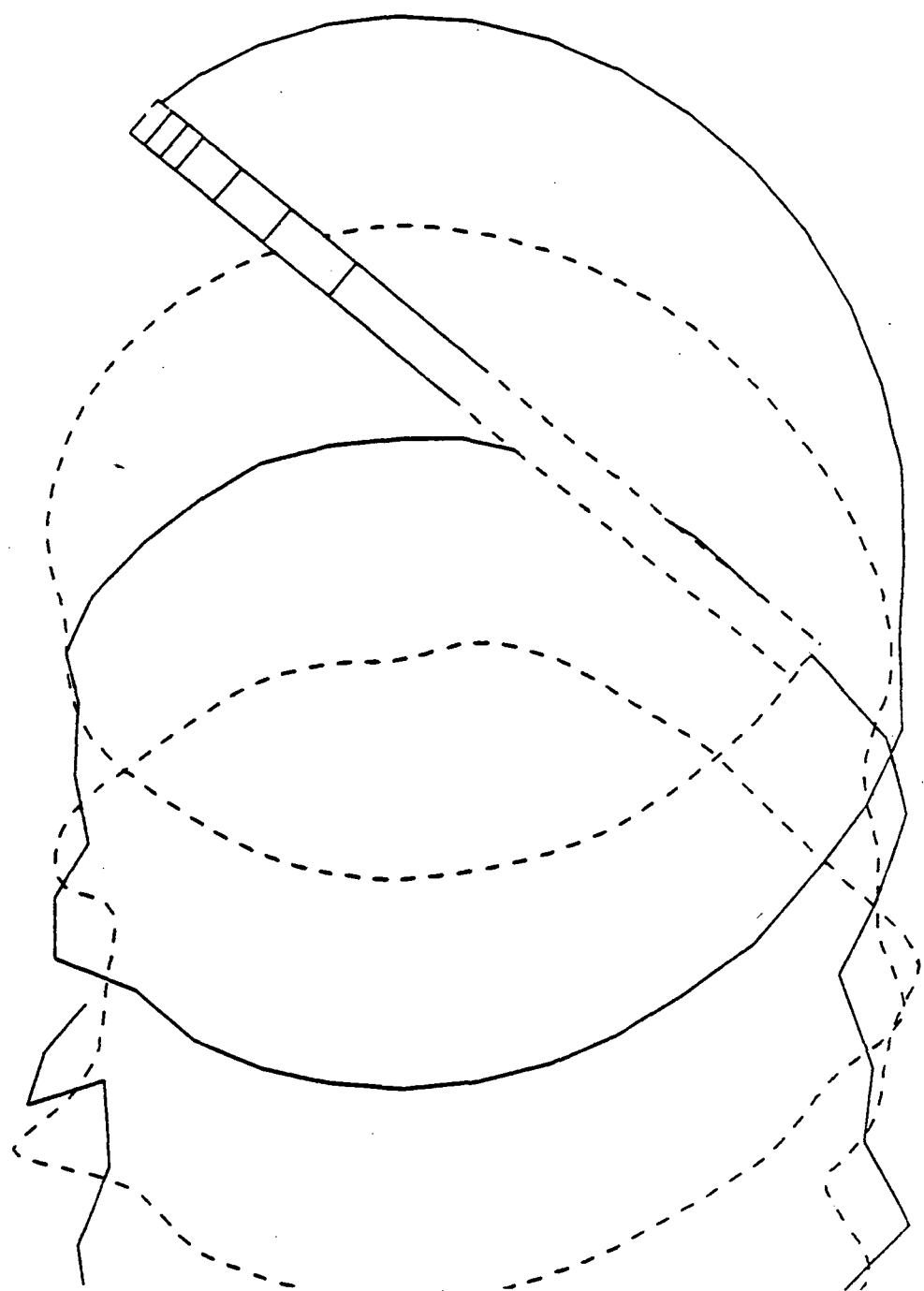


Figure 23. Tip vortex geometry for instrumented blade azimuth of 230 degrees.

$R/C = -500$  MU = 0.158 PSI = 240

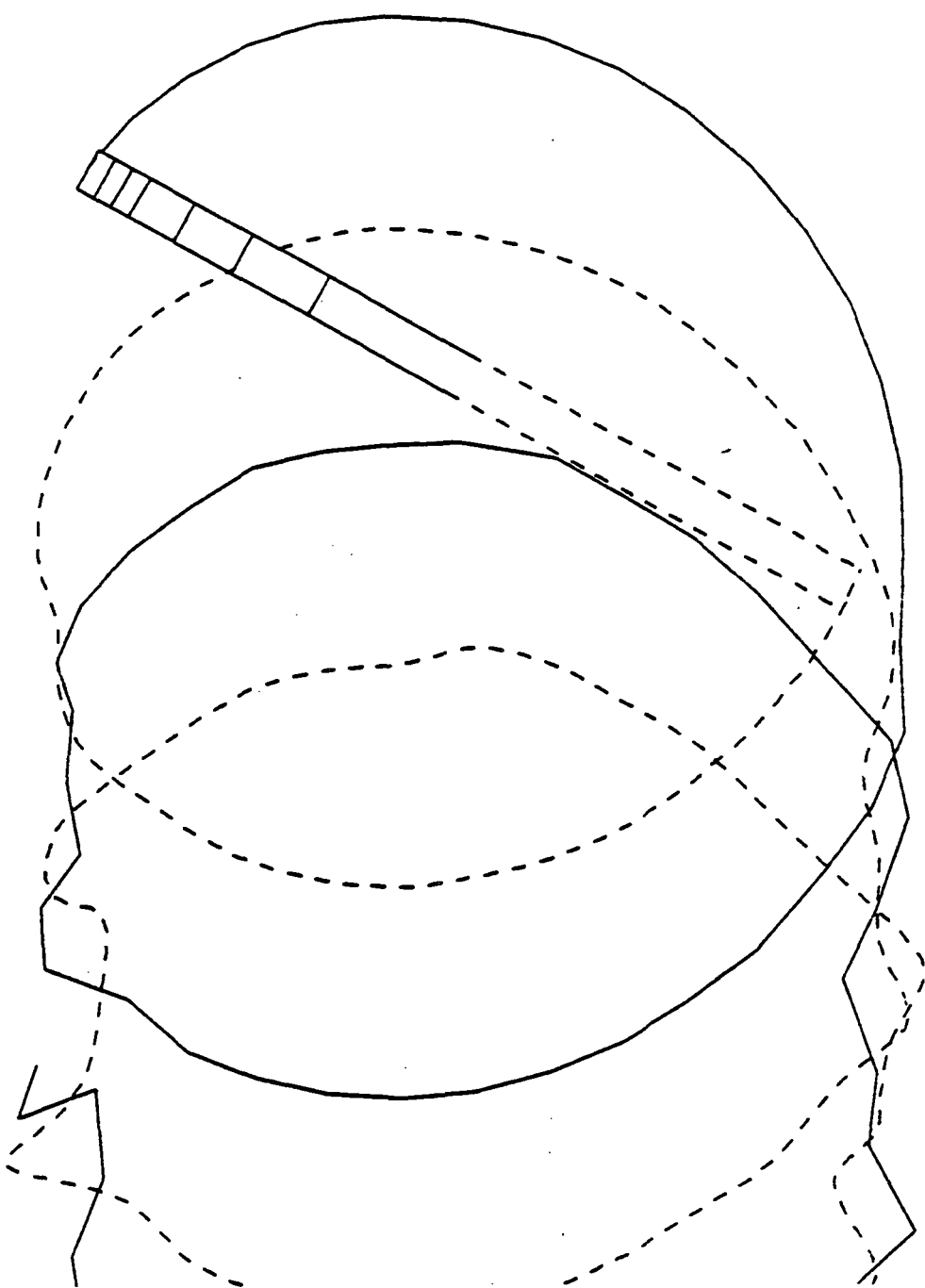


Figure 24. Tip vortex geometry for instrumented blade azimuth of 240 degrees.

R/C = -500 MU = 0.158 PSI = 250

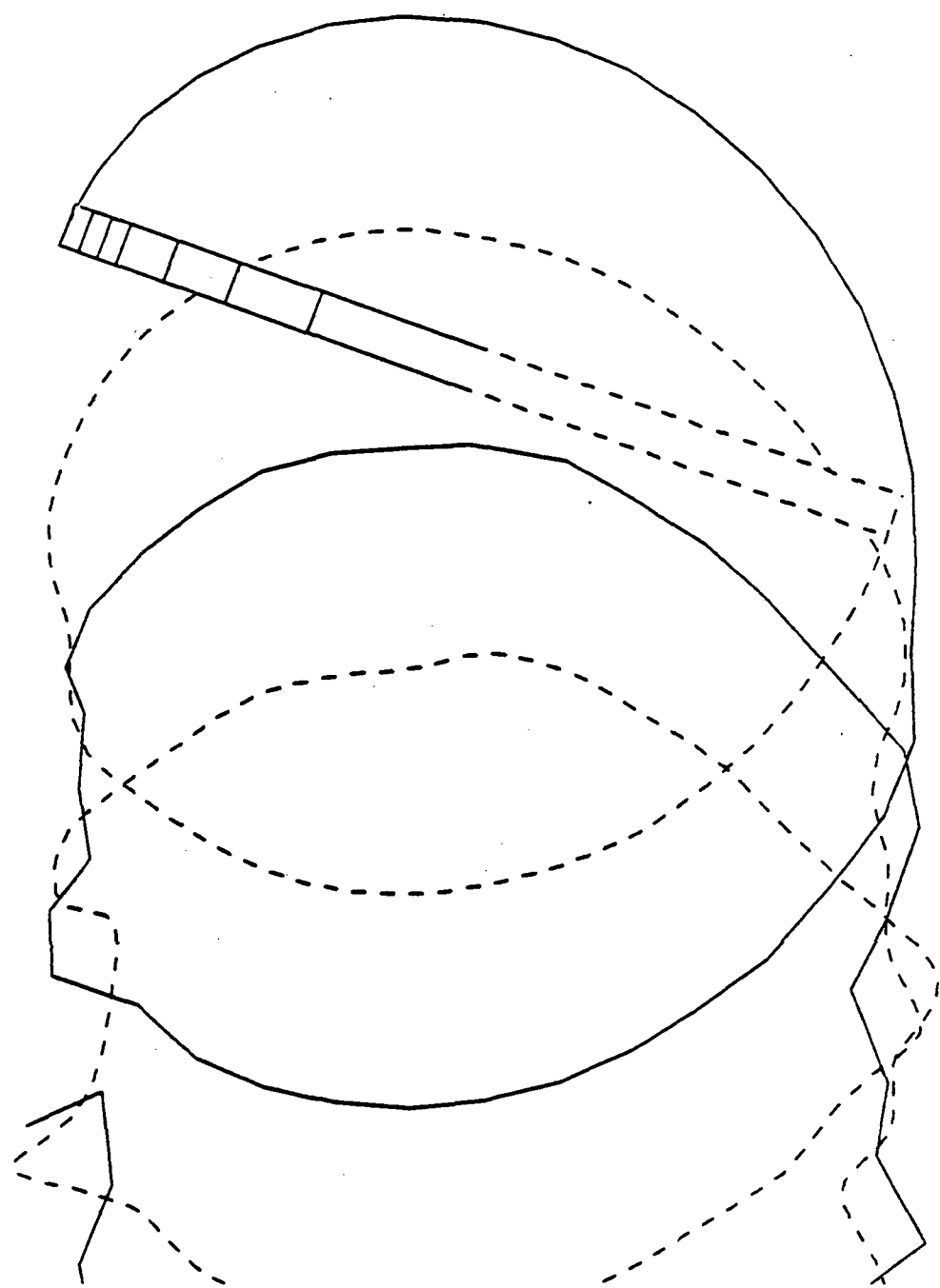


Figure 25. Tip vortex geometry for instrumented blade azimuth of 250 degrees.

$R/C = -500$   $MU = 0.158$   $PSI = 260$

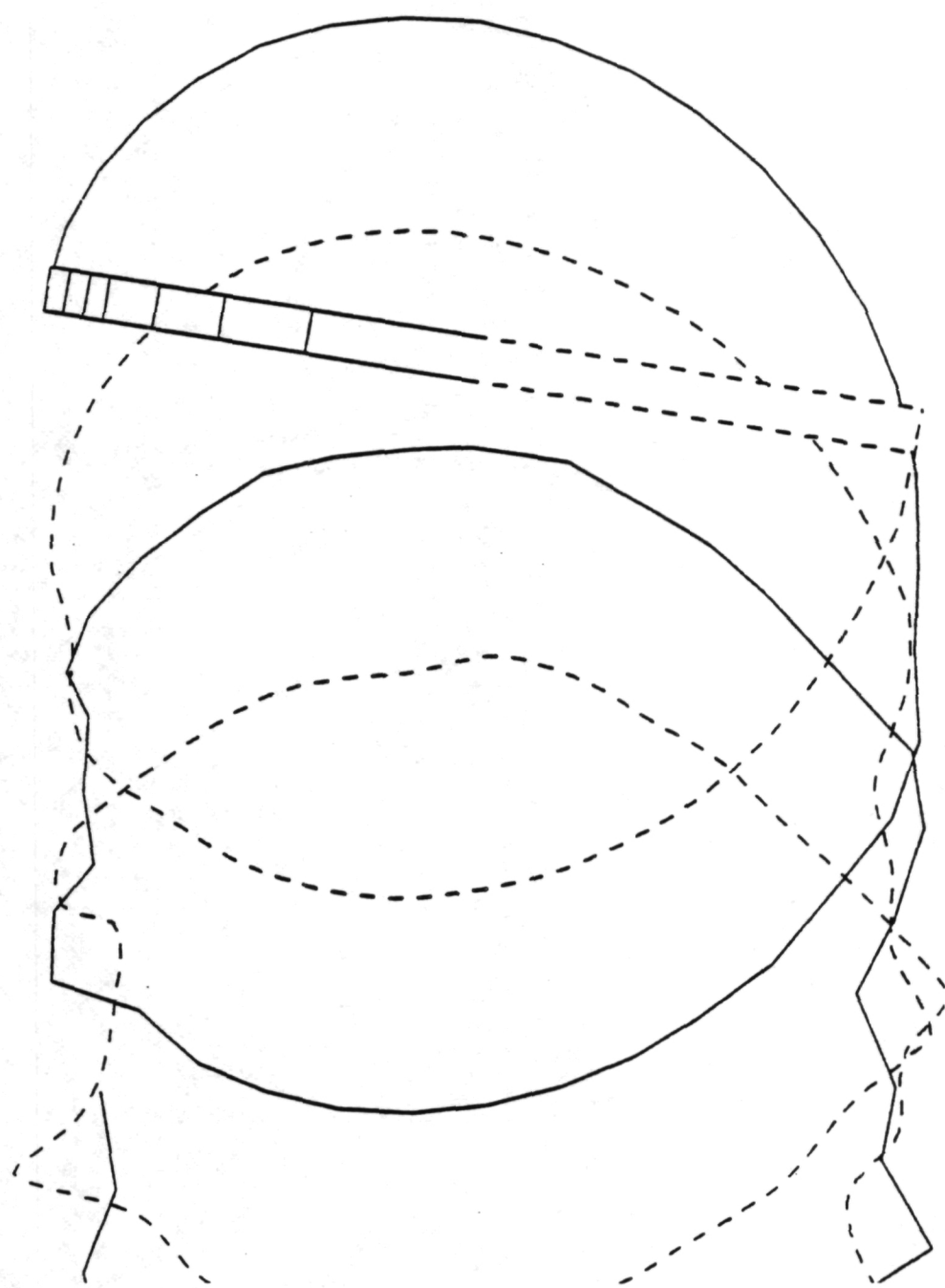


Figure 26. Tip vortex geometry for instrumented blade azimuth of 260 degrees.

$R/C = -500$  MU = 0.158 PSI = 270

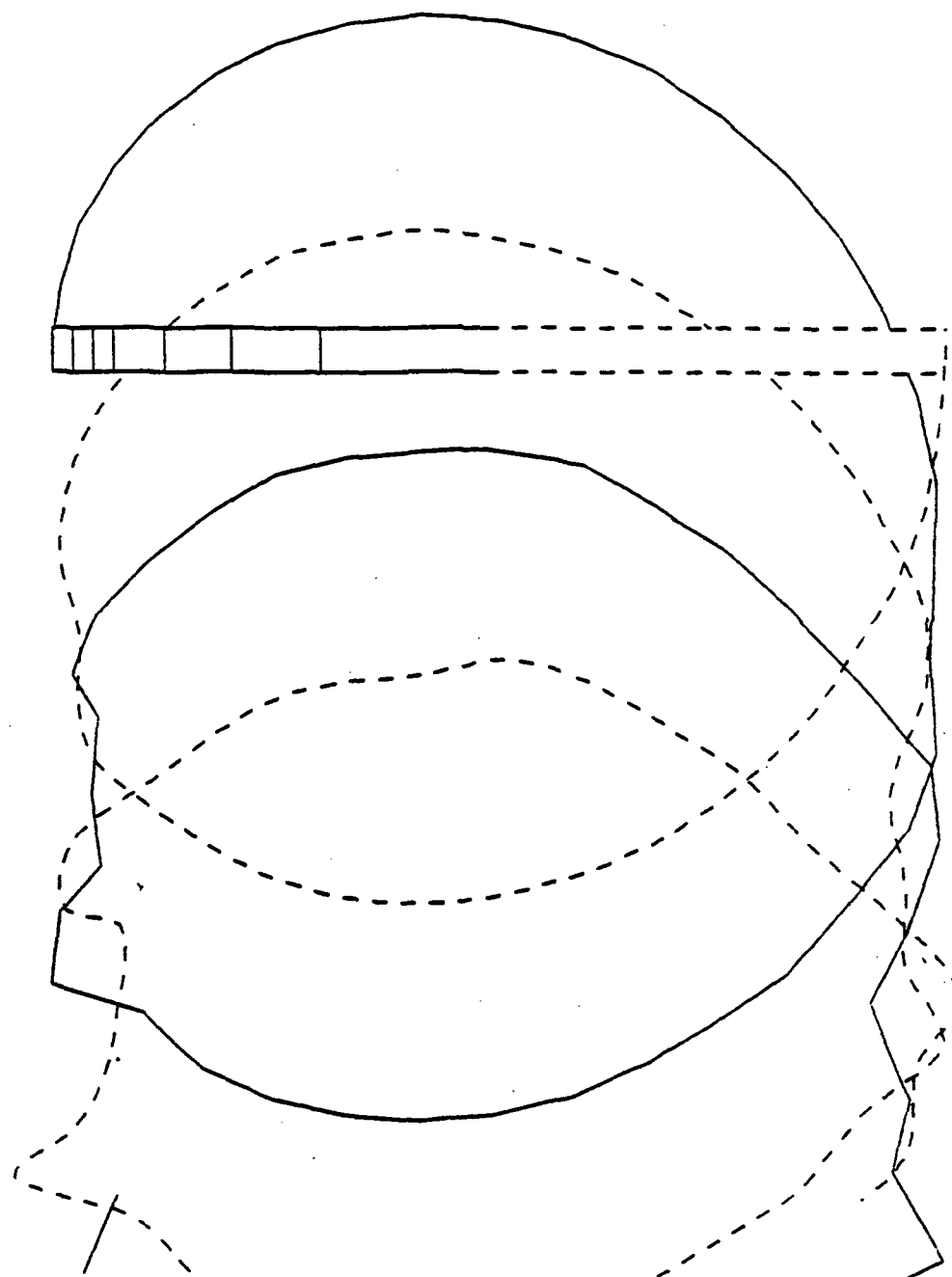


Figure 27. Tip vortex geometry for instrumented blade azimuth of 270 degrees.

$R/C = -500$   $MU = 0.158$   $PSI = 280$

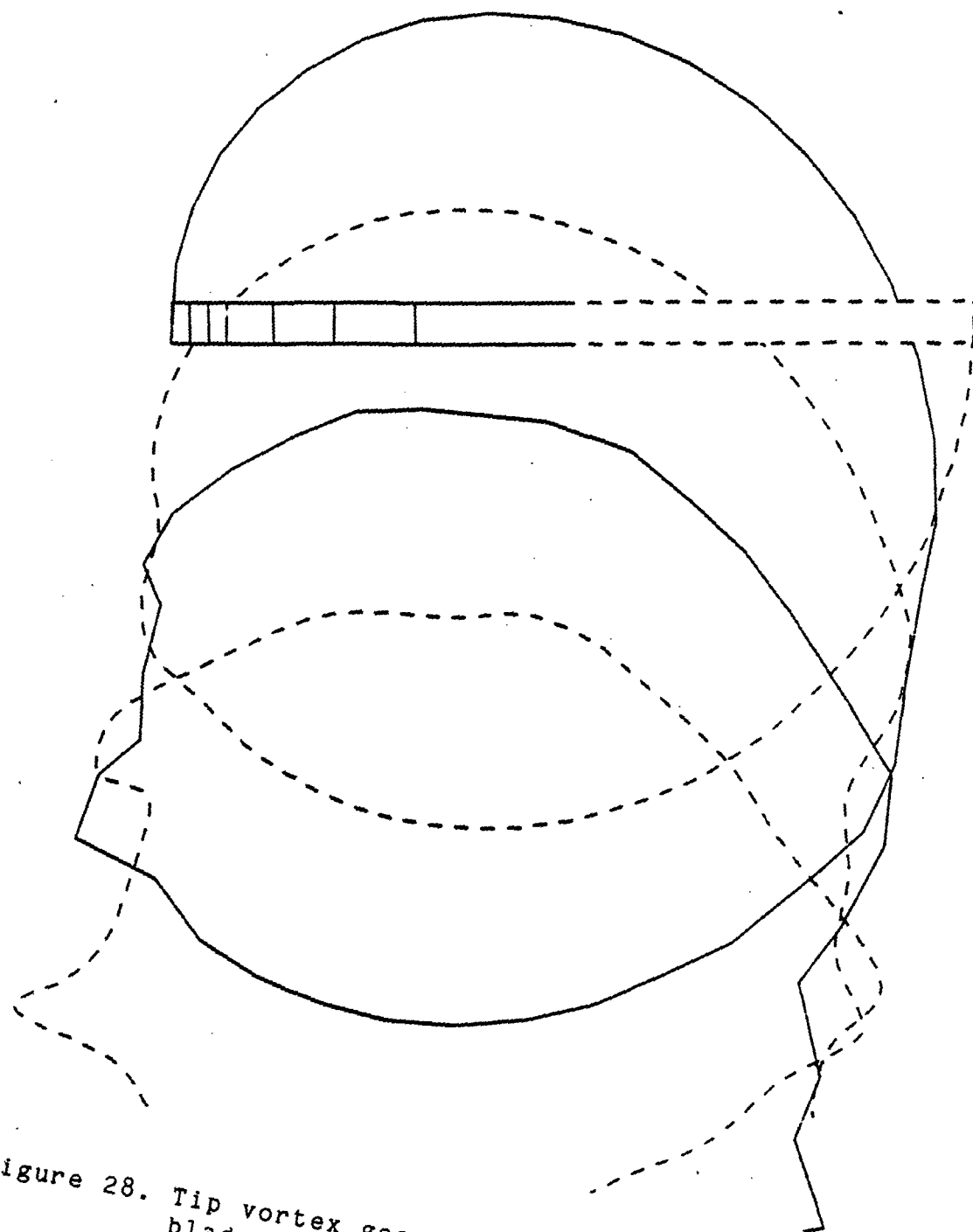


Figure 28. Tip vortex geometry for instrumented blade azimuth of 280 degrees.

R/C = -500 MU = 0.158 PSI = 290

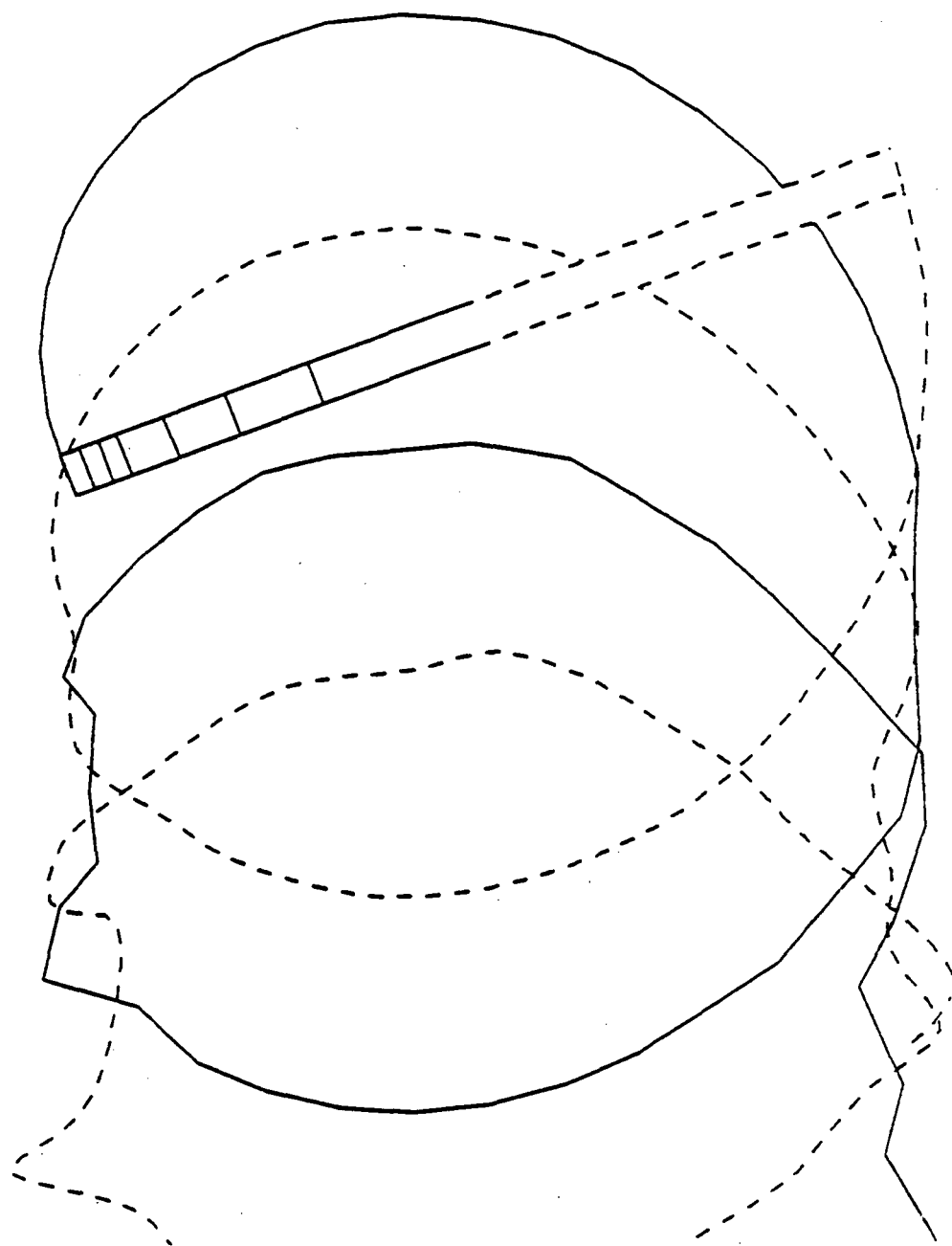


Figure 29. Tip vortex geometry for instrumented blade azimuth of 290 degrees.

R/C = -500 MU = 0.158 PSI = 300

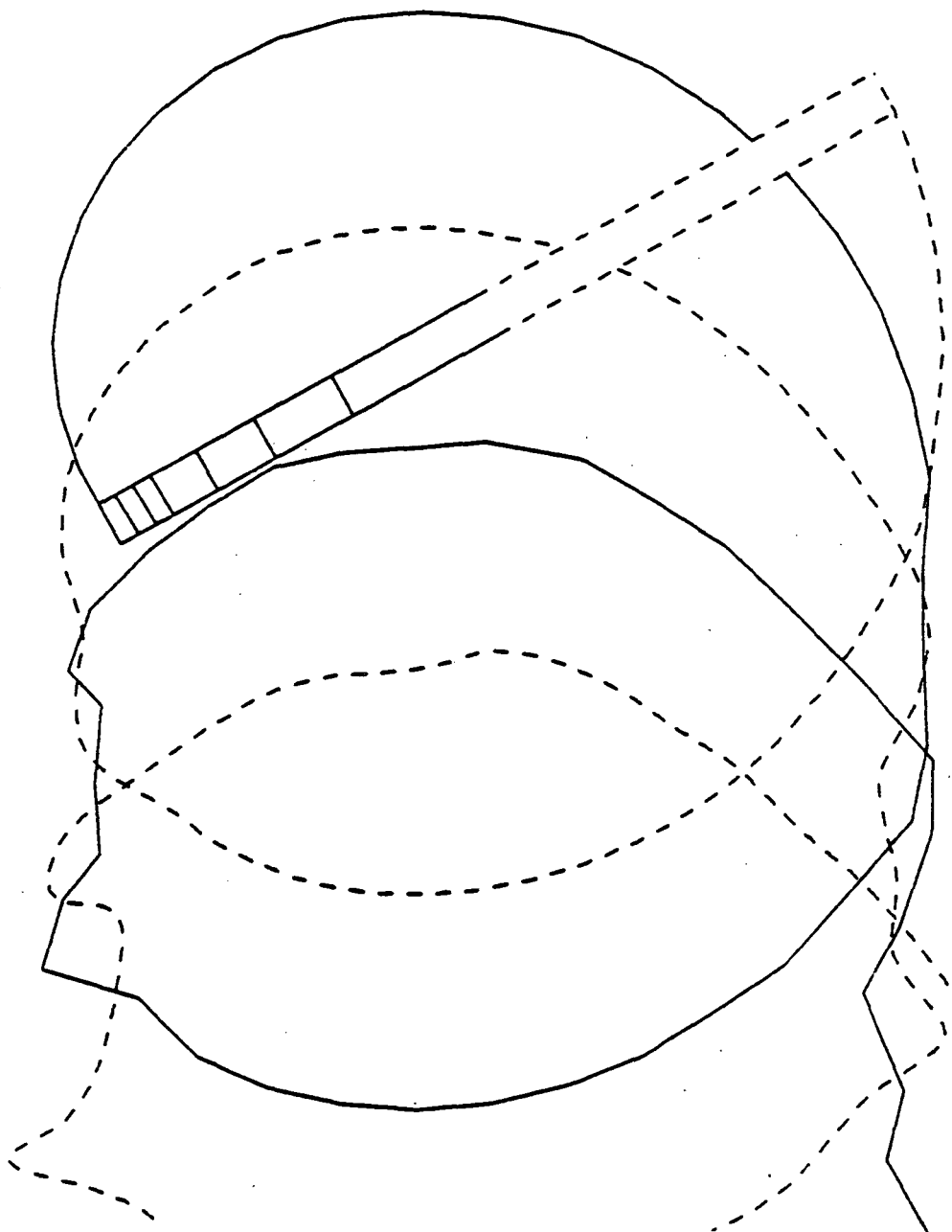


Figure 30. Tip vortex geometry for instrumented blade azimuth of 300 degrees.

$R/C = -500$  MU = 0.158 PSI = 310

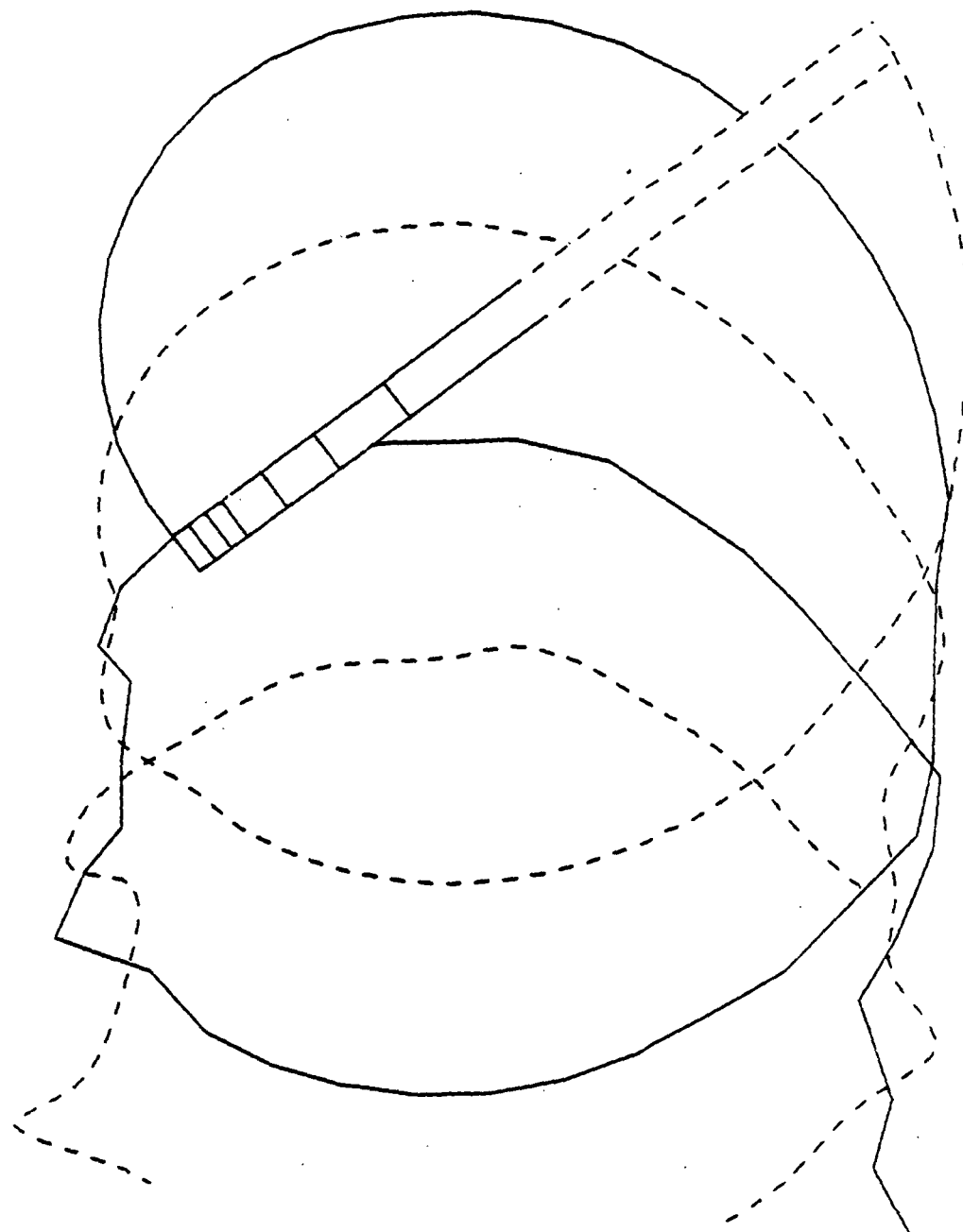


Figure 31. Tip vortex geometry for instrumented blade azimuth of 310 degrees.

R/C = -500 MU = 0.158 PSI = 320

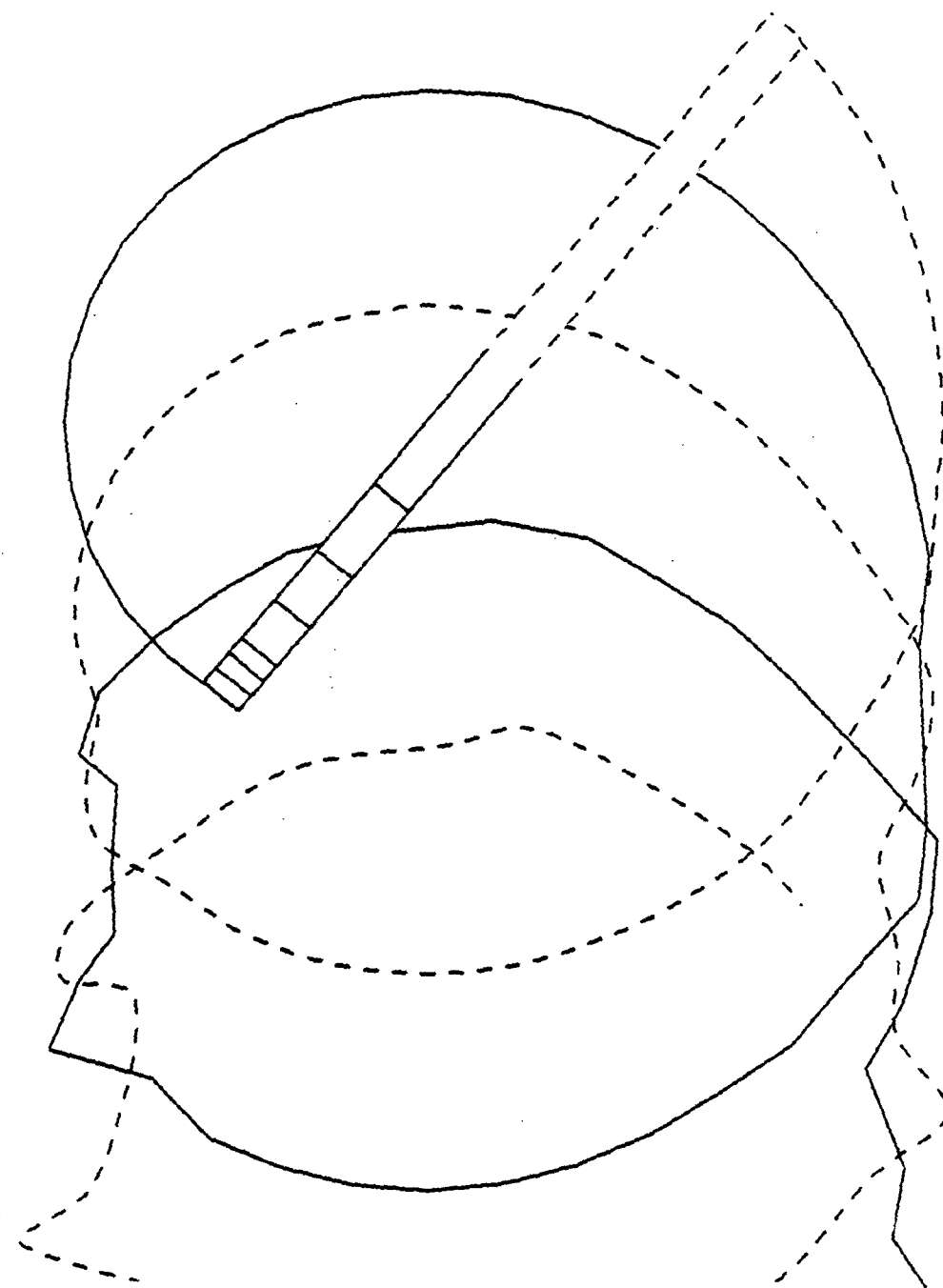


Figure 32. Tip vortex geometry for instrumented blade azimuth of 320 degrees.

R/C = -500 MU = 0.158 PSI = 330

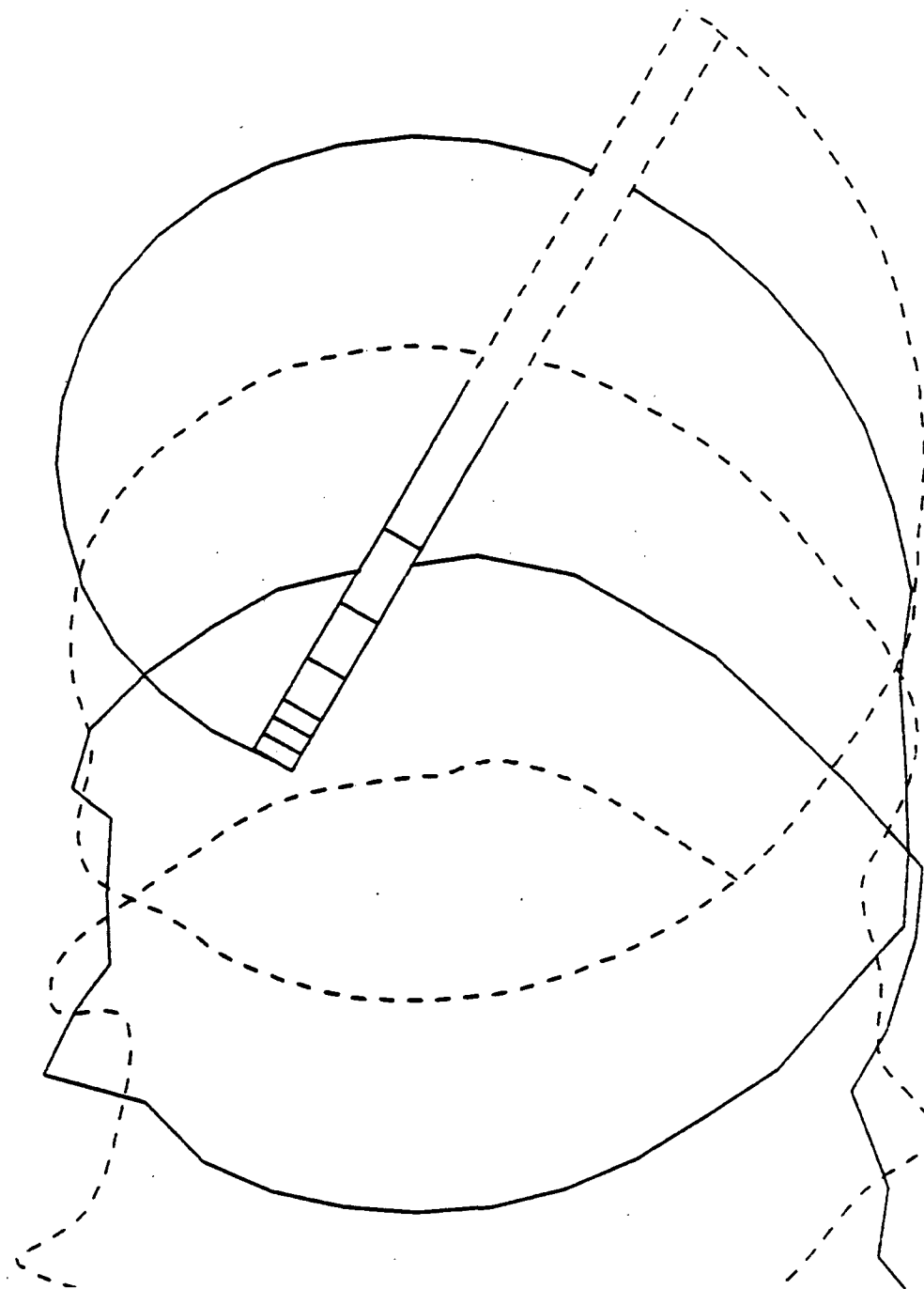


Figure 33. Tip vortex geometry for instrumented blade azimuth of 330 degrees.

R/C = -500 MU = 0.158 PSI = 340

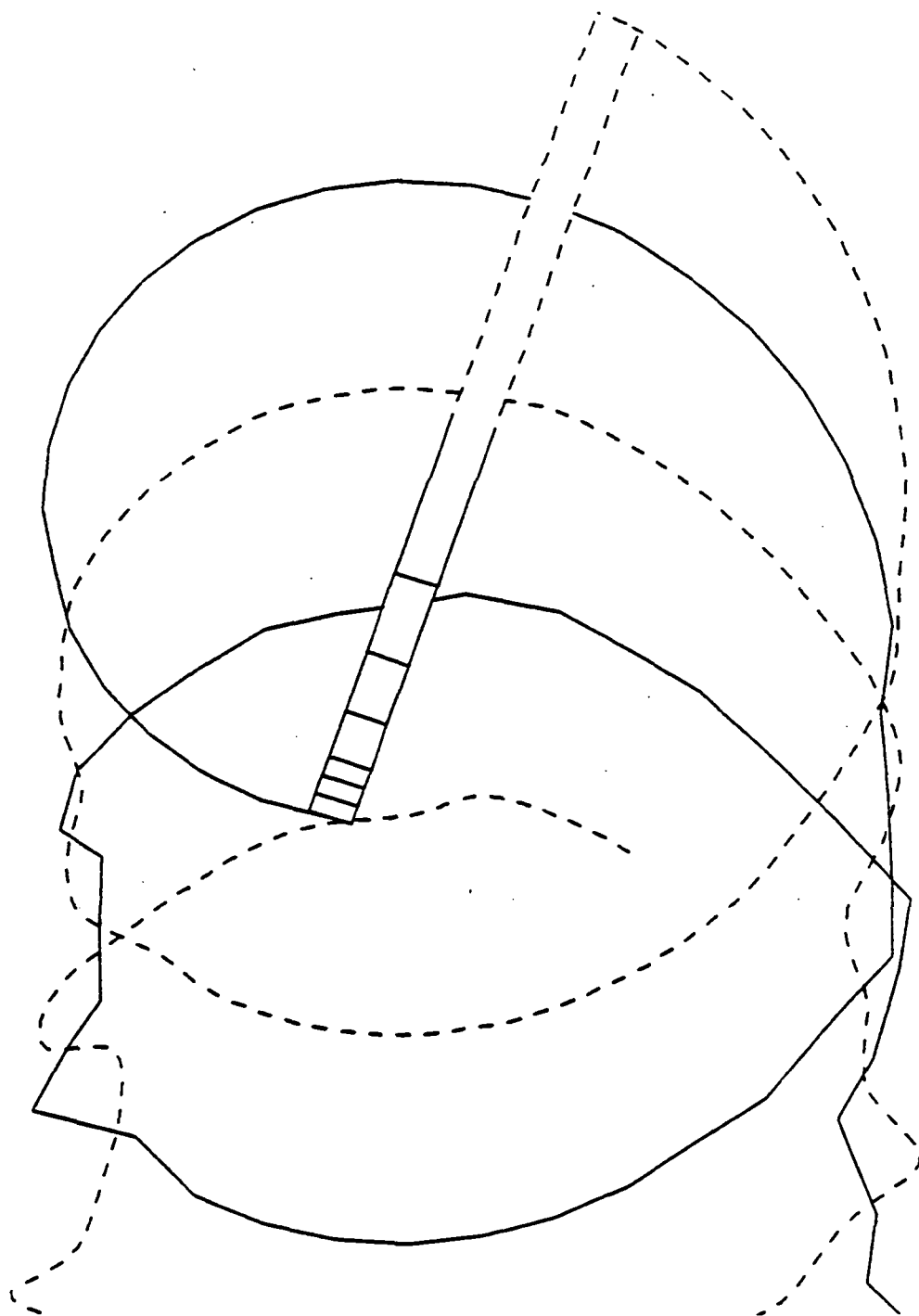


Figure 34. Tip vortex geometry for instrumented blade azimuth of 340 degrees.

$R/C = -500$  MU = 0.158 PSI = 350

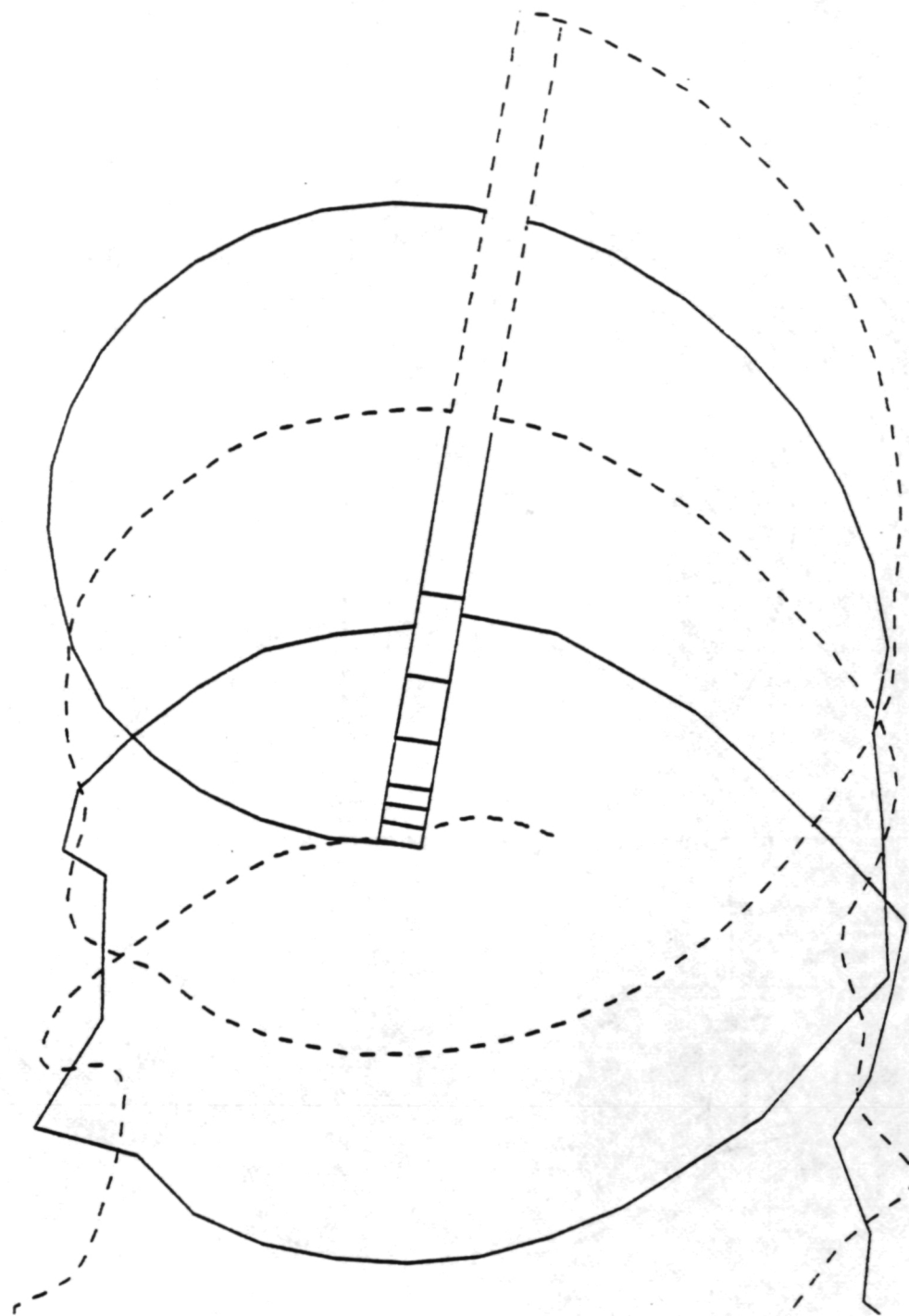


Figure 35. Tip vortex geometry for instrumented blade azimuth of 350 degrees.

$R/C = -500$  MU = 0.158 PSI = 360

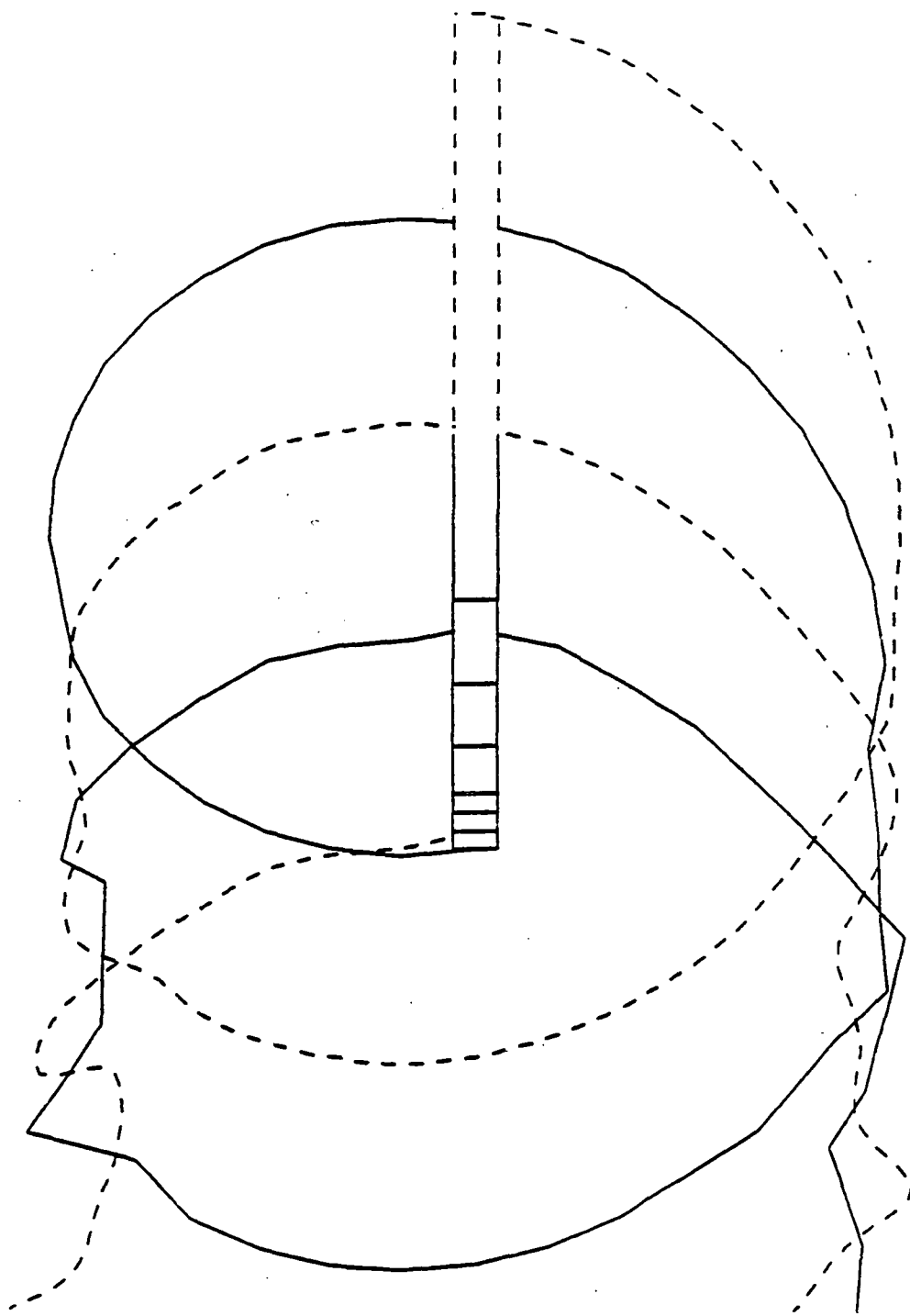


Figure 36. Tip vortex geometry for instrumented blade azimuth of 360 degrees.

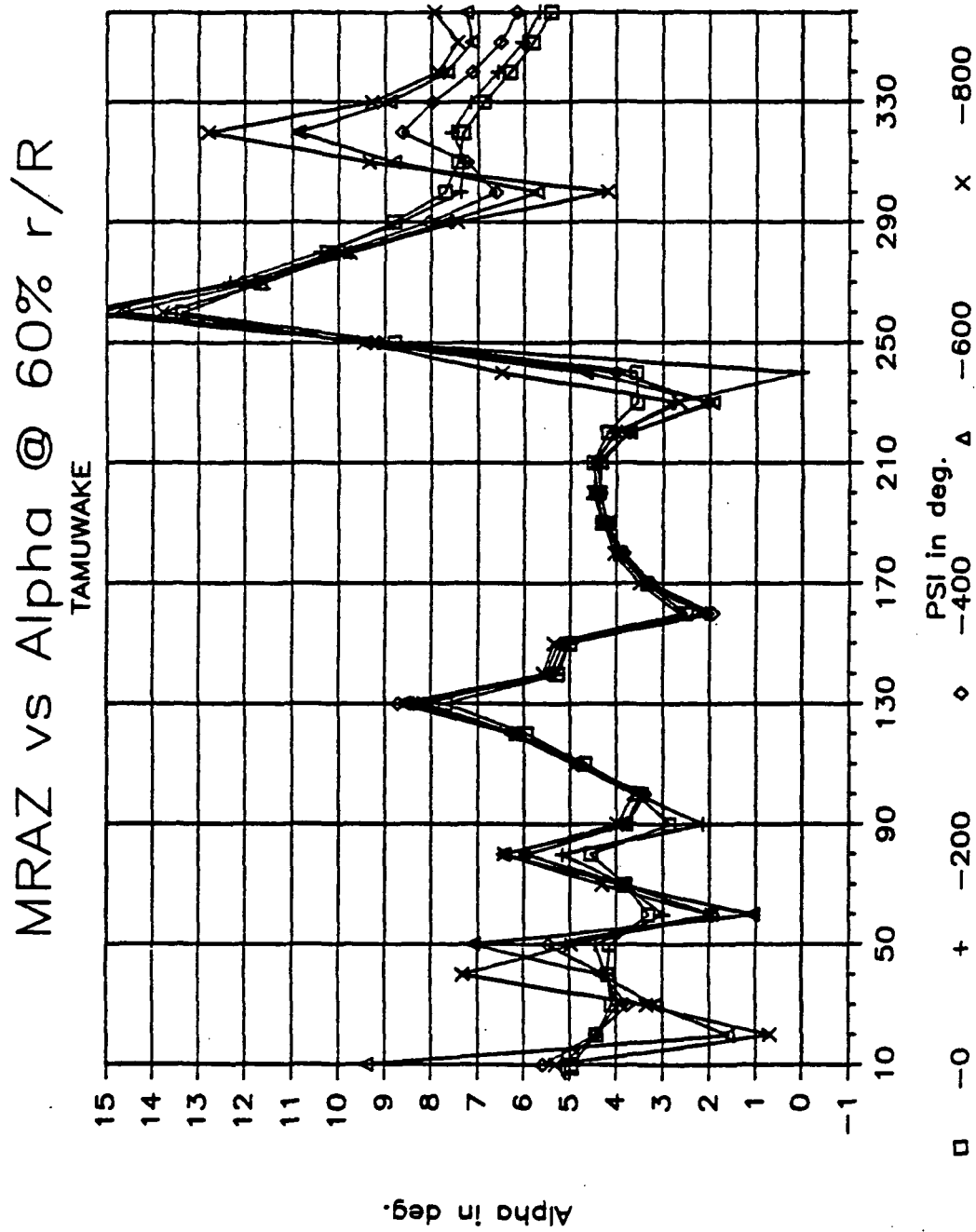


Figure 37. Free wake analysis predicted azimuthal angle of attack variation for different rates of descent. 60 percent blade radius station.

# MRAZ vs Alpha @ 60% r/R

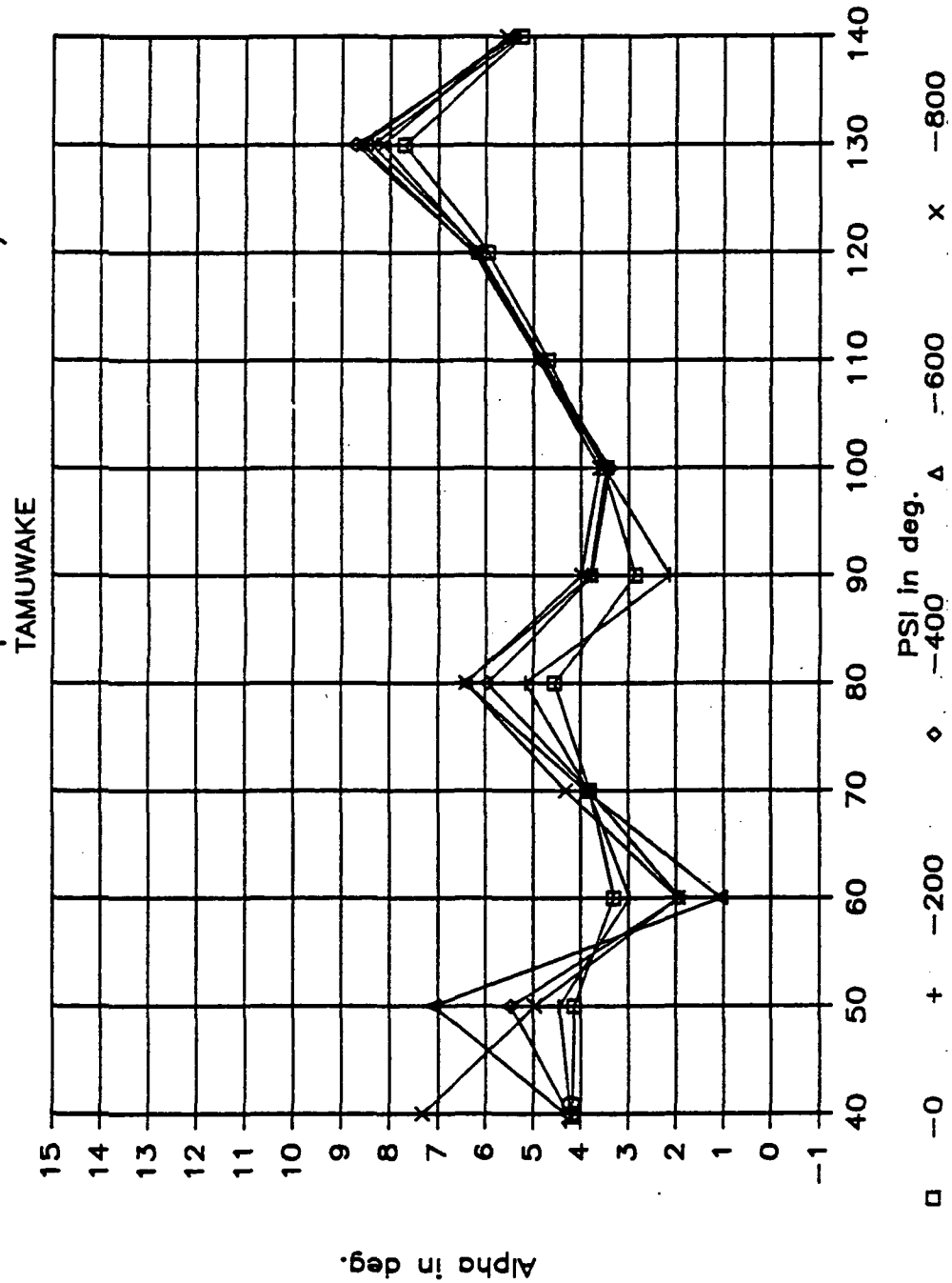


Figure 38. Free wake analysis predicted azimuthal angle of attack variation for different rates of descent. Expanded scale. 60 percent blade radius station.

MRAZ vs Alpha @ 75% r/R  
TAMUWAKE

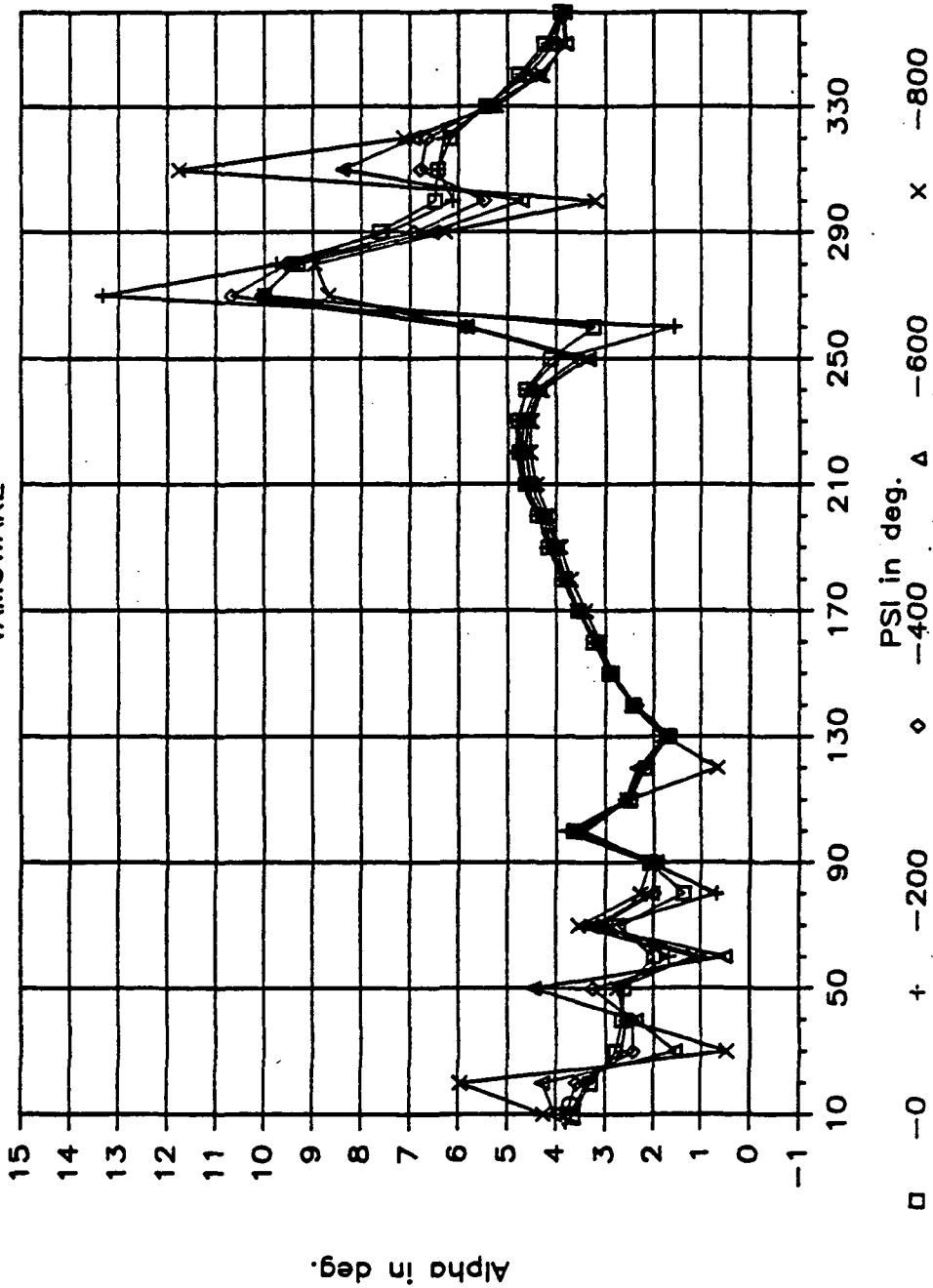


Figure 39. Free wake analysis predicted azimuthal angle of attack variation for different rates of descent. 75 percent blade radius station.

# MRAZ vs Alpha @ 75% r/R

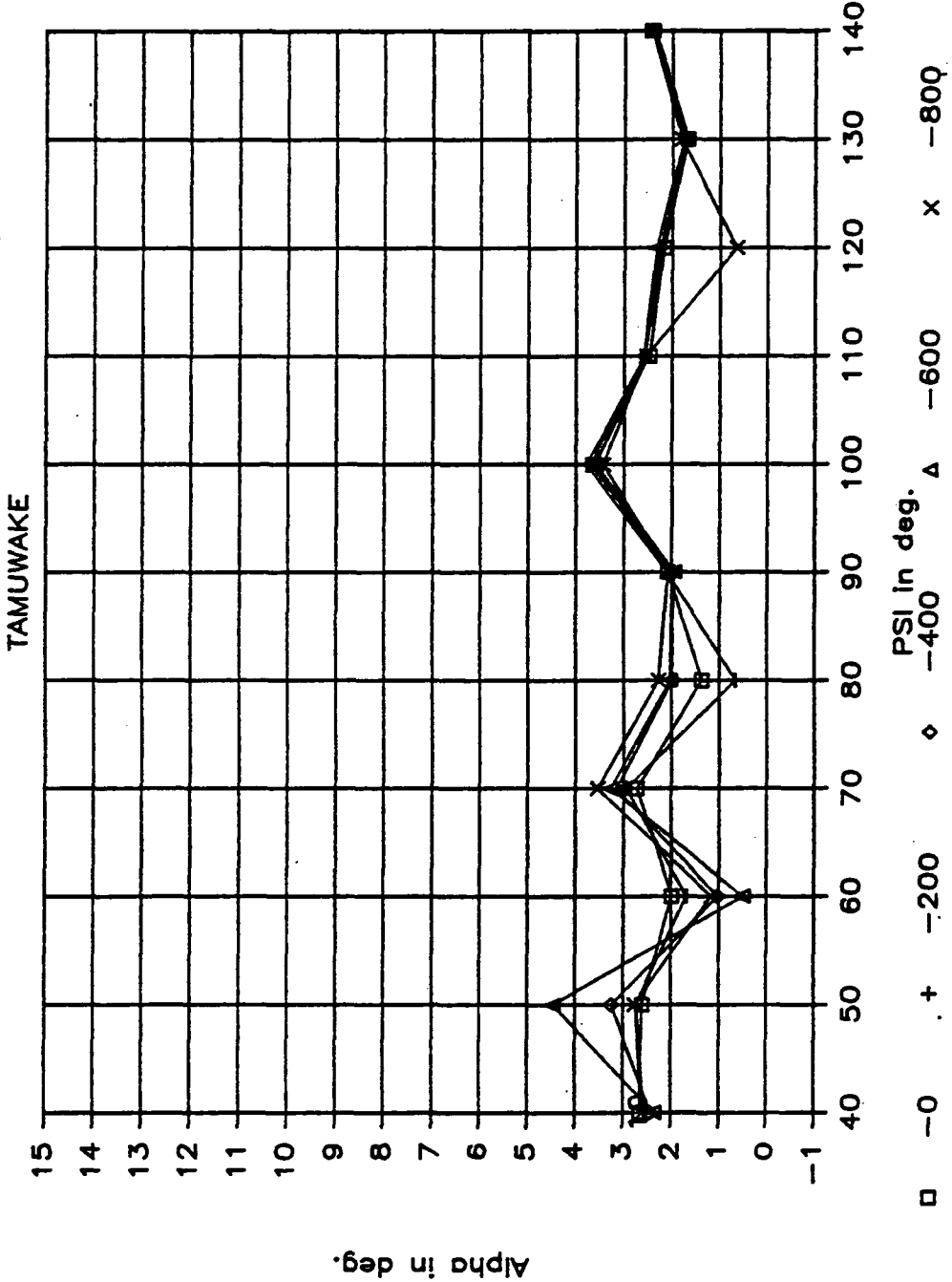


Figure 40. Free wake analysis predicted azimuthal angle of attack variation for different rates of descent. Expanded scale. 75 percent blade radius station.

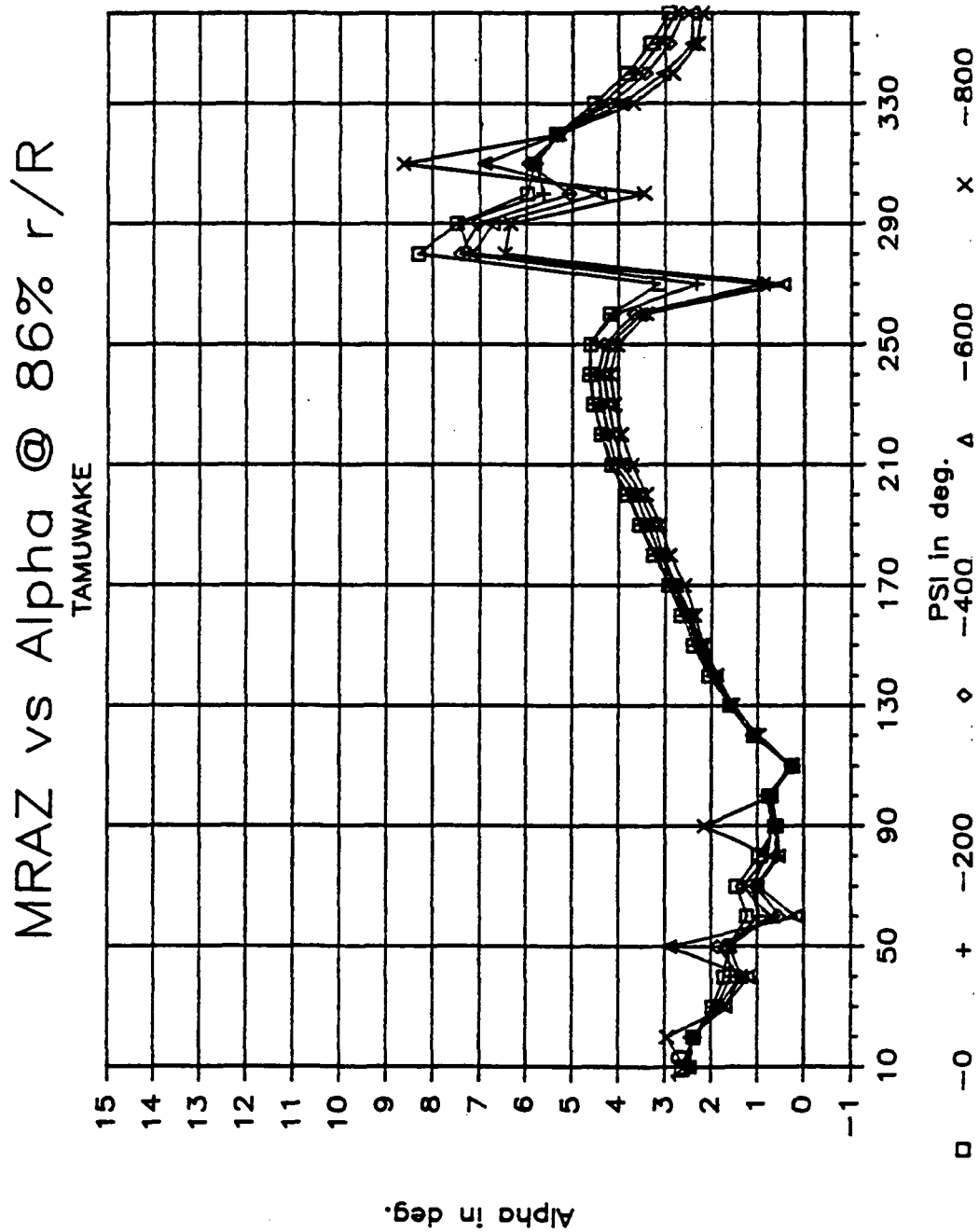


Figure 41. Free wake analysis predicted azimuthal angle of attack variation for different rates of descent. 86 percent blade radius station.

# MRAZ vs Alpha @ 86% r/R

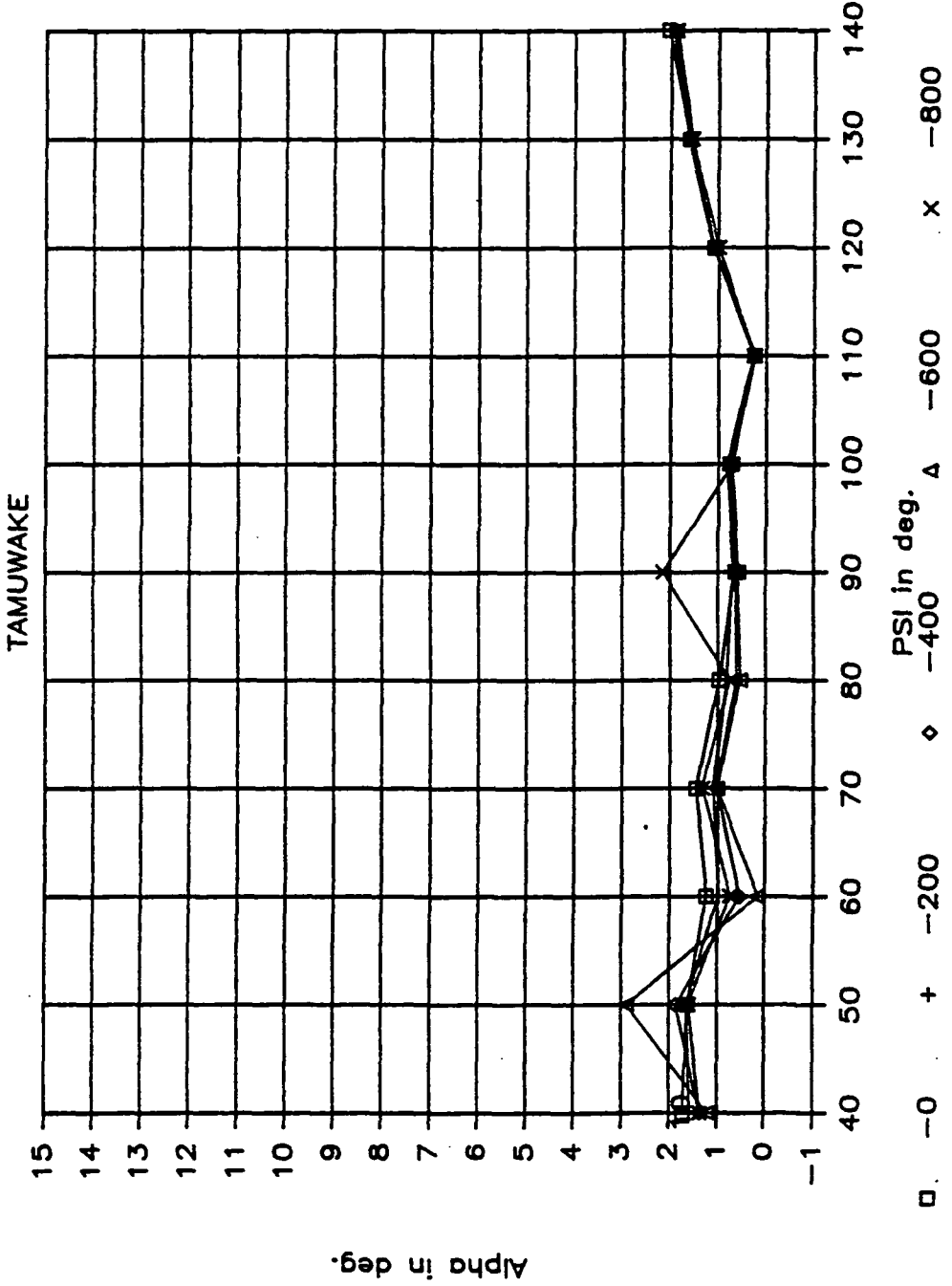


Figure 42. Free wake analysis predicted azimuthal angle of attack variation for different rates of descent. Expanded scale. 86 percent blade radius station.

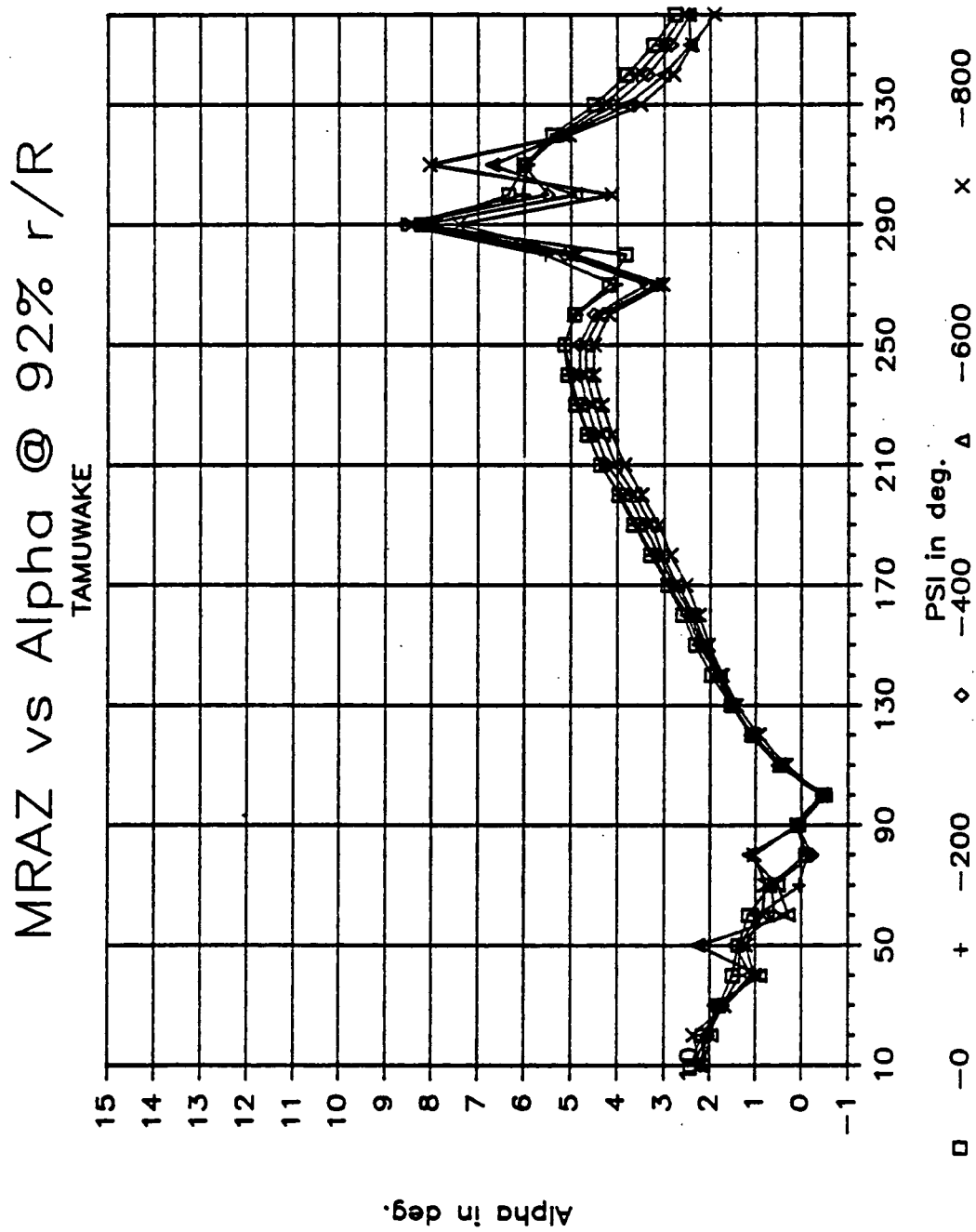


Figure 43. Free wake analysis predicted azimuthal angle of attack variation for different rates of descent. 92 percent blade radius station.

MRAZ VS Alpha @ 92% r/R  
TAMUWAKE

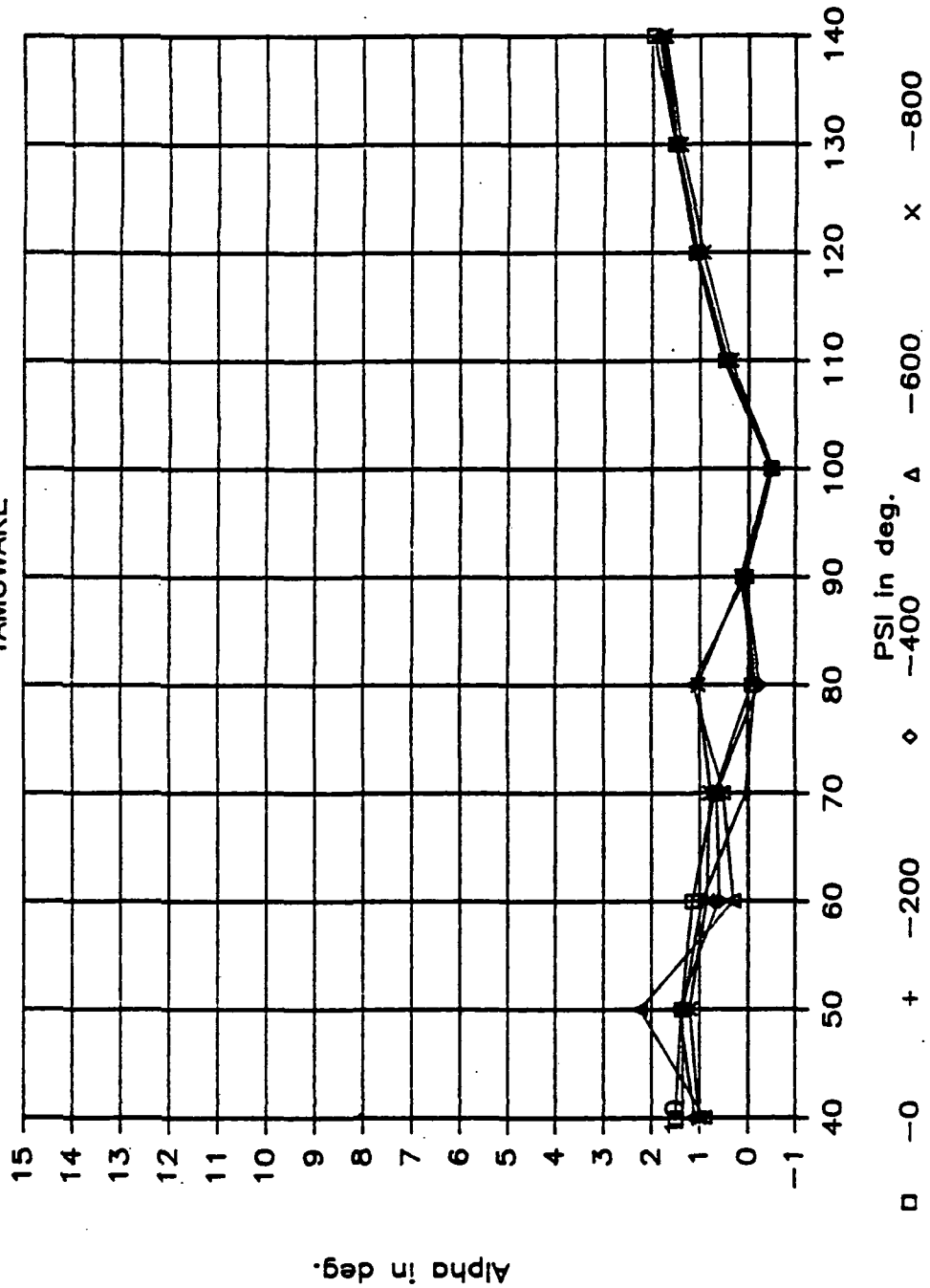
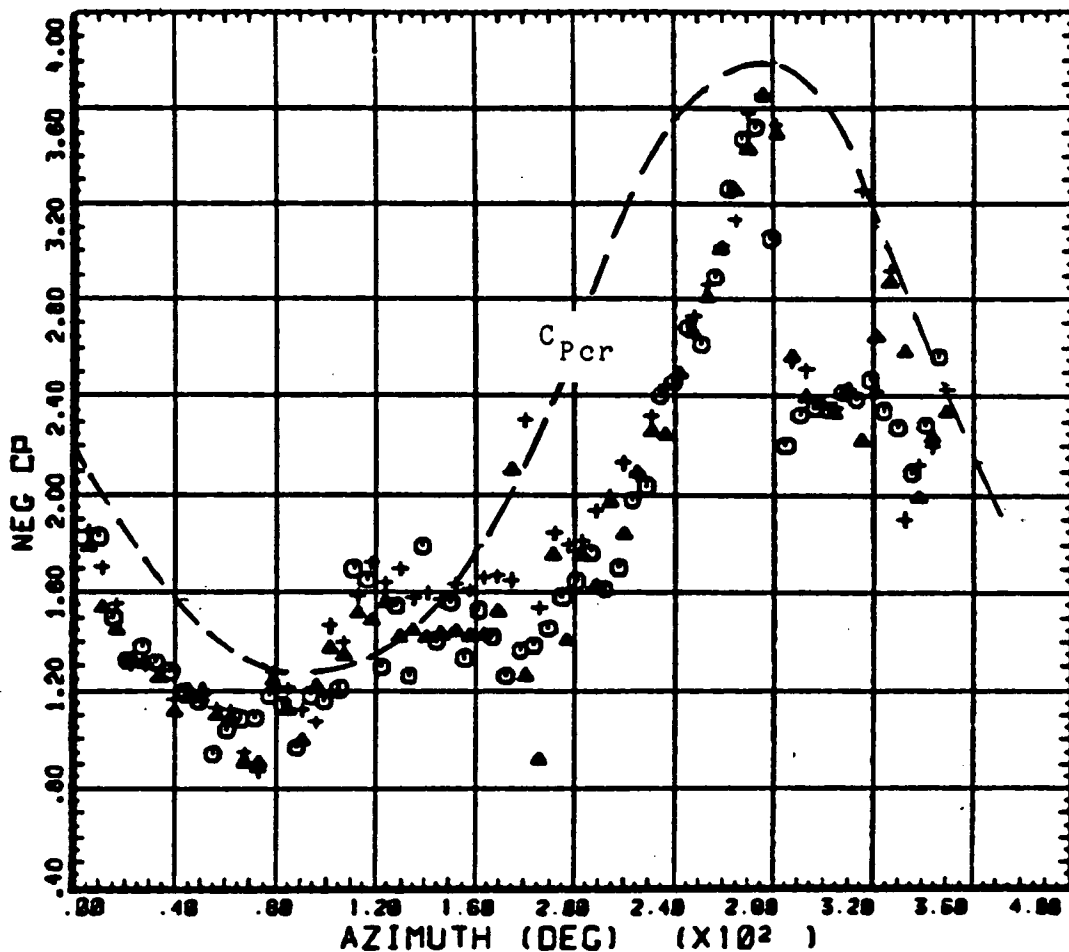


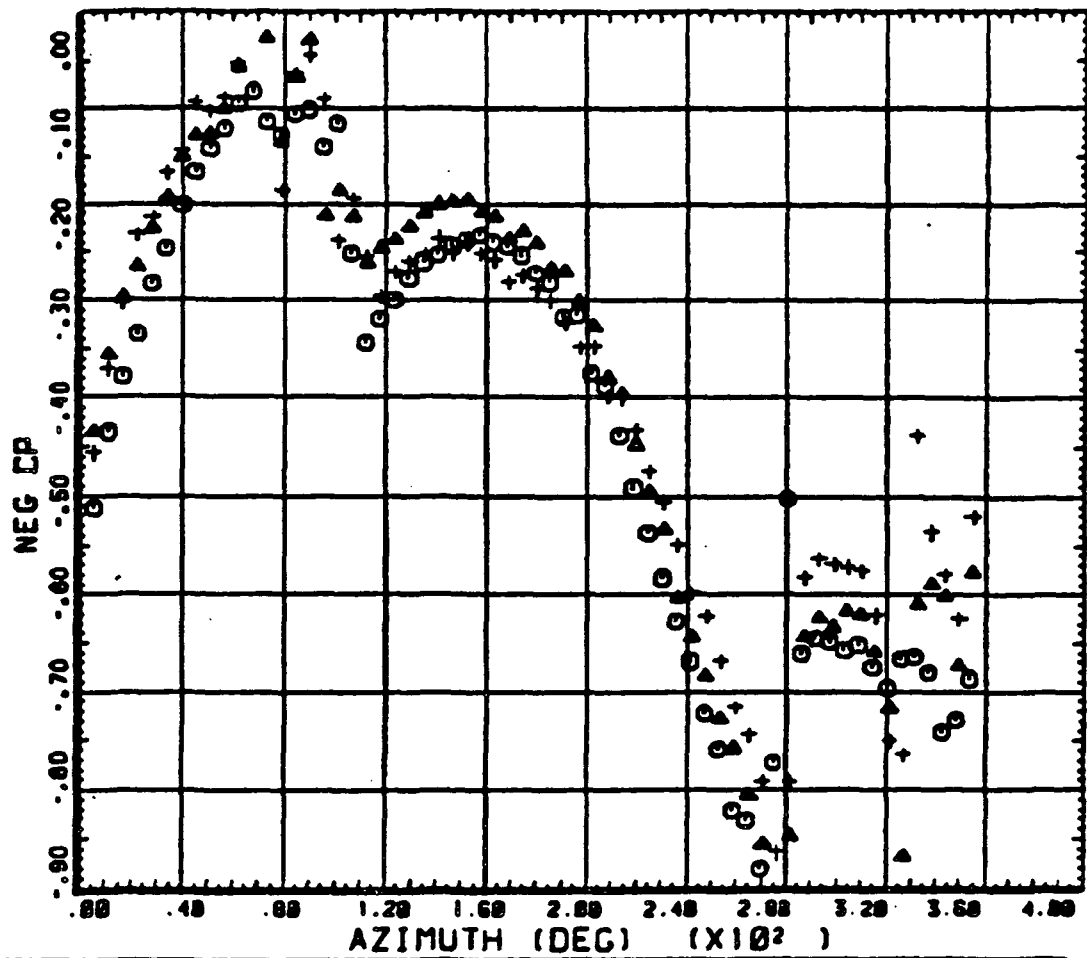
Figure 44. Free wake analysis predicted azimuthal angle of attack variation for different rates of descent. Expanded scale. 92 percent blade radius station.

ORIGINAL PAGE IS  
OF POOR QUALITY



○ ○ ○	COUNTER	3150	GROSS VT	SHIP MODEL	AM-1G
DERIVED PARAMETER.	.75	R/RADIUS	LONG CG	TOP SURFACE	
△ △ △	COUNTER	3151	GROSS VT	SHIP MODEL	AM-1G
DERIVED PARAMETER.	.75	R/RADIUS	LONG CG	TOP SURFACE	
+ + +	COUNTER	3152	GROSS VT	SHIP MODEL	AM-1G
DERIVED PARAMETER.	.75	R/RADIUS	LONG CG	TOP SURFACE	
		BLADE STATIC PRESSURE COEFF			

Figure 45. Azimuthal variation of pressure coefficient for 3 different rates of descent. Upper surface, 75 percent radius, 3 percent chord.



○ ○ ○	COUNTER .75	3150 R/RADIUS BLADE STATIC	GROSS WT LONG CG PRESSURE COEFF	SHIP MODEL AN-1G BOTTOM SURFACE
△ △ △	COUNTER .75	3151 R/RADIUS BLADE STATIC	GROSS WT LONG CG PRESSURE COEFF	SHIP MODEL AN-1G BOTTOM SURFACE
+++	COUNTER .75	3152 R/RADIUS BLADE STATIC	GROSS WT LONG CG PRESSURE COEFF	SHIP MODEL AN-1G BOTTOM SURFACE

Figure 46. Azimuthal variation of pressure coefficient for 3 different rates of descent. Lower surface, 75 percent radius, 3 percent chord.

ORIGINAL PAGE IS  
OF POOR QUALITY

ORIGINAL PAGE IS  
OF POOR QUALITY

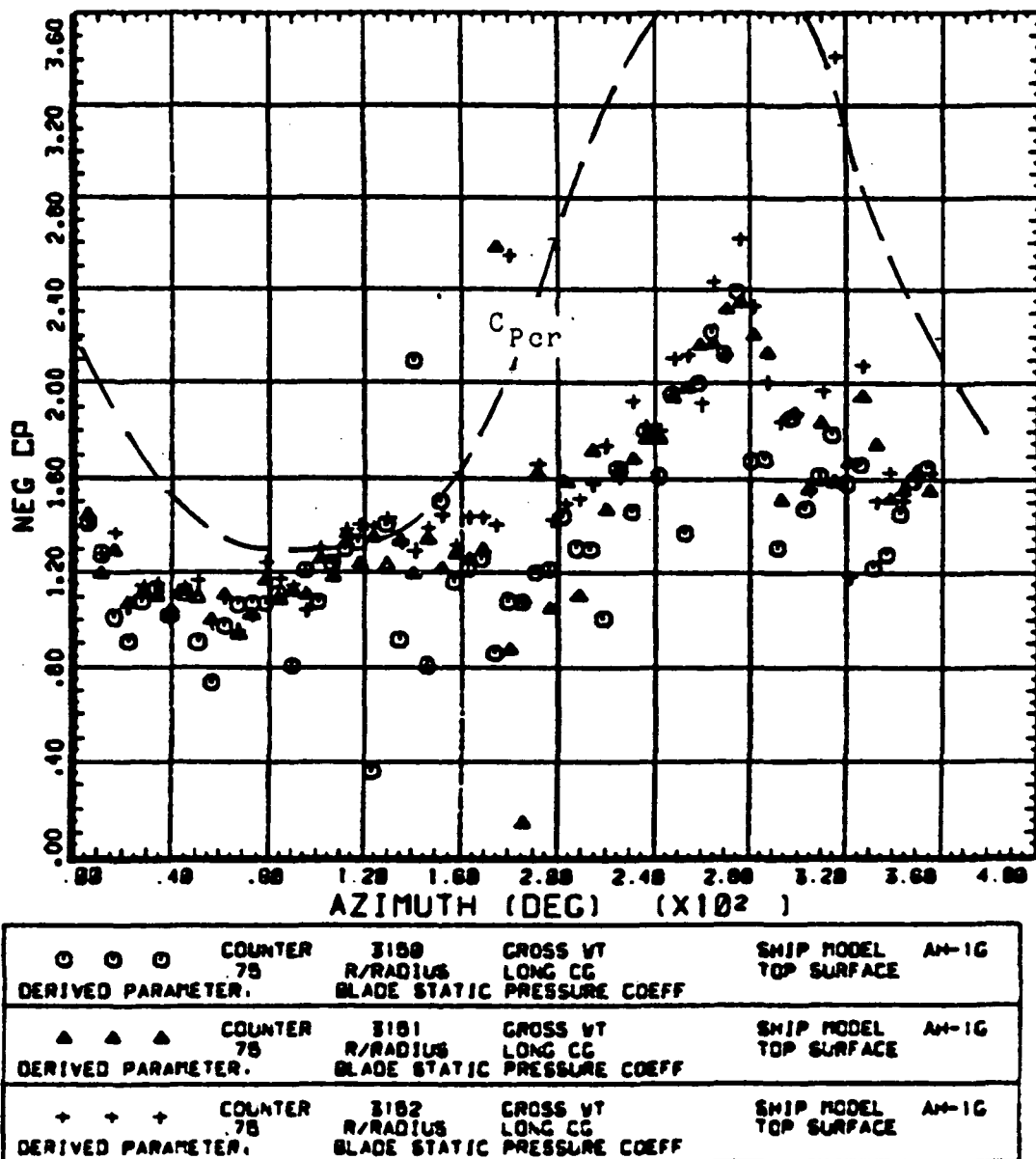
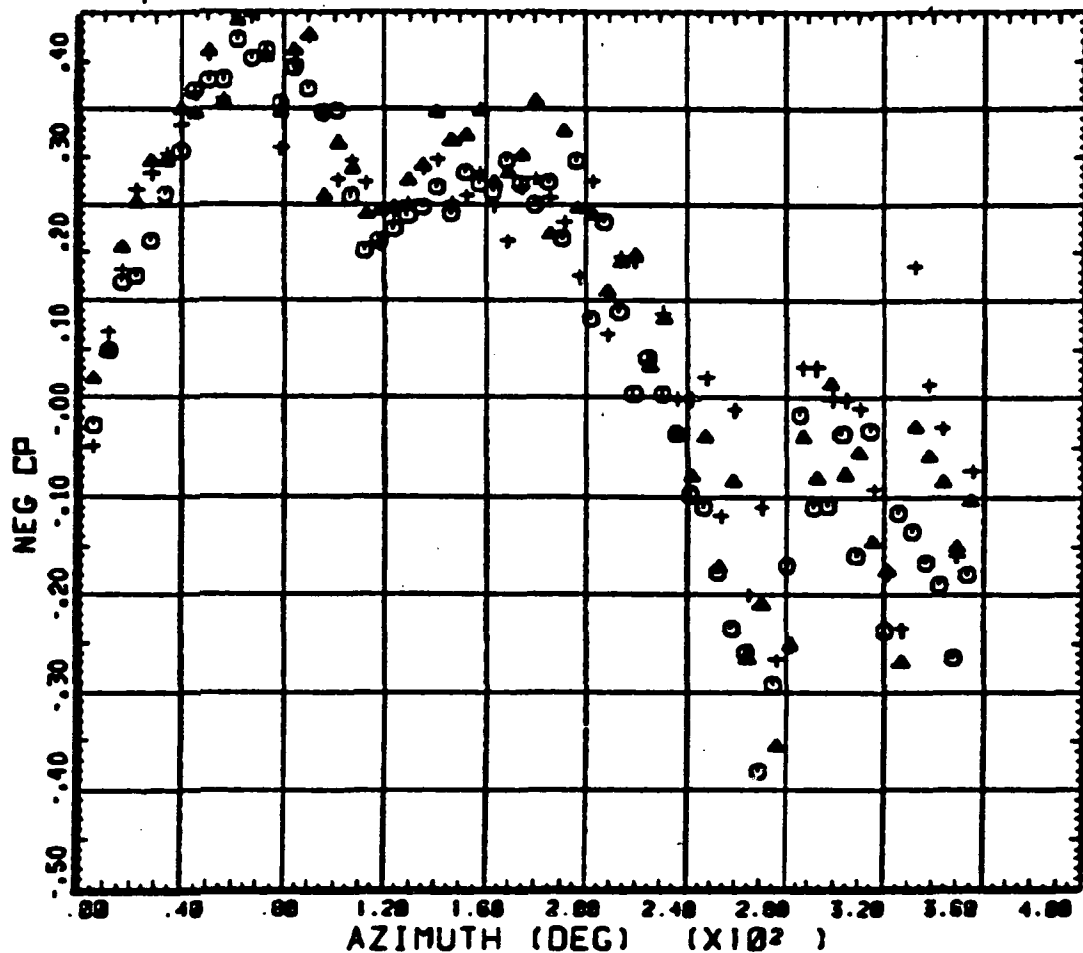


Figure 47. Azimuthal variation of pressure coefficient for 3 different rates of descent. Upper surface, 75 percent radius, 8 percent chord.

ORIGINAL PAGE IS  
OF POOR QUALITY



○ ○ ○	COUNTER	3150	GROSS WT	SHIP MODEL
DERIVED PARAMETER.	75	R/RADIUS	LONG CG	AM-1G
▲ ▲ ▲	COUNTER	3151	GROSS WT	SHIP MODEL
DERIVED PARAMETER.	75	R/RADIUS	LONG CG	AM-1G
† † †	COUNTER	3152	GROSS WT	SHIP MODEL
DERIVED PARAMETER.	75	R/RADIUS	LONG CG	BOTTOM SURFACE

Figure 48. Azimuthal variation of pressure coefficient for 3 different rates of descent. Lower surface, 75 percent radius, 8 percent chord.

ORIGINAL PAGE IS  
OF POOR QUALITY

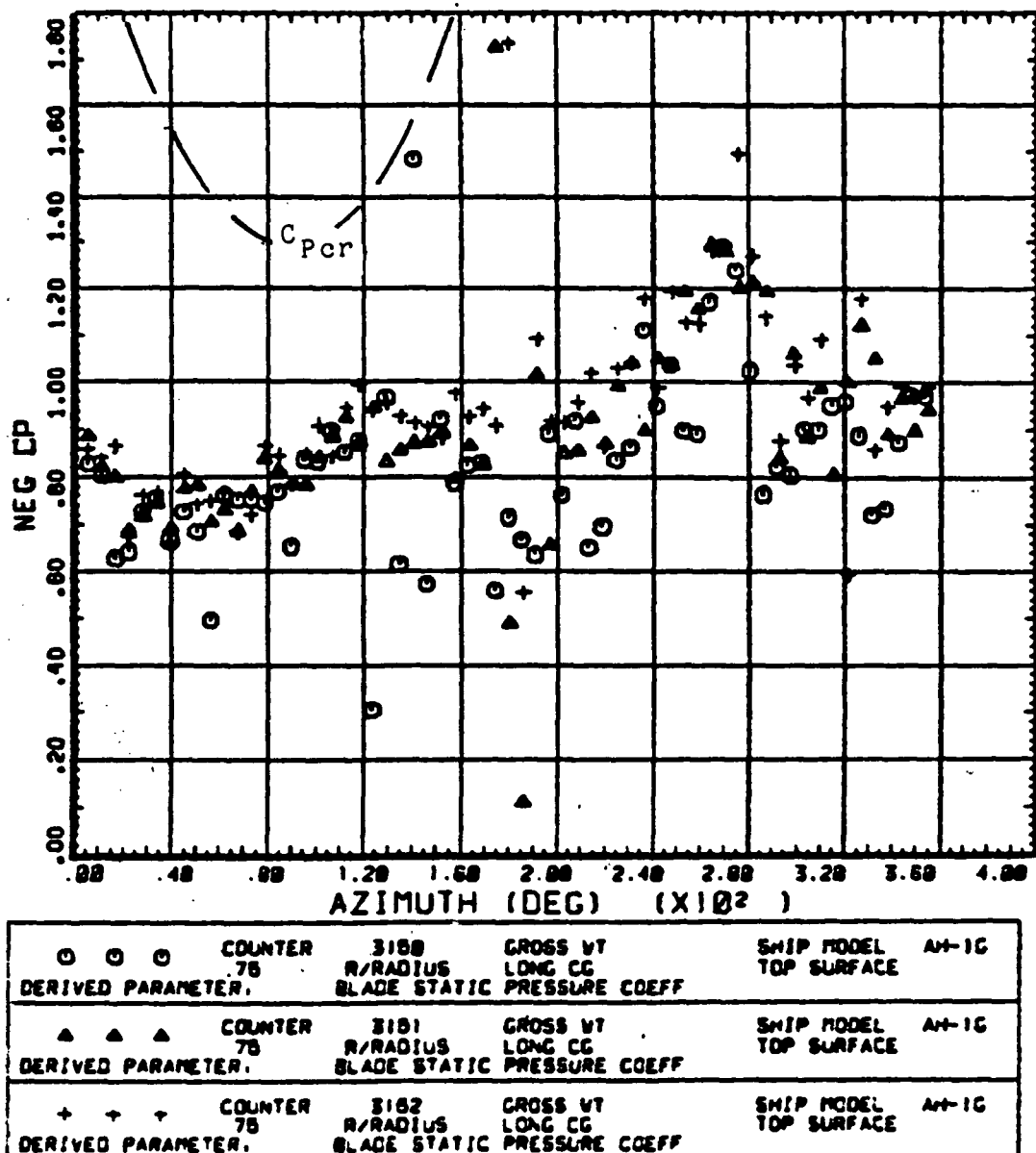
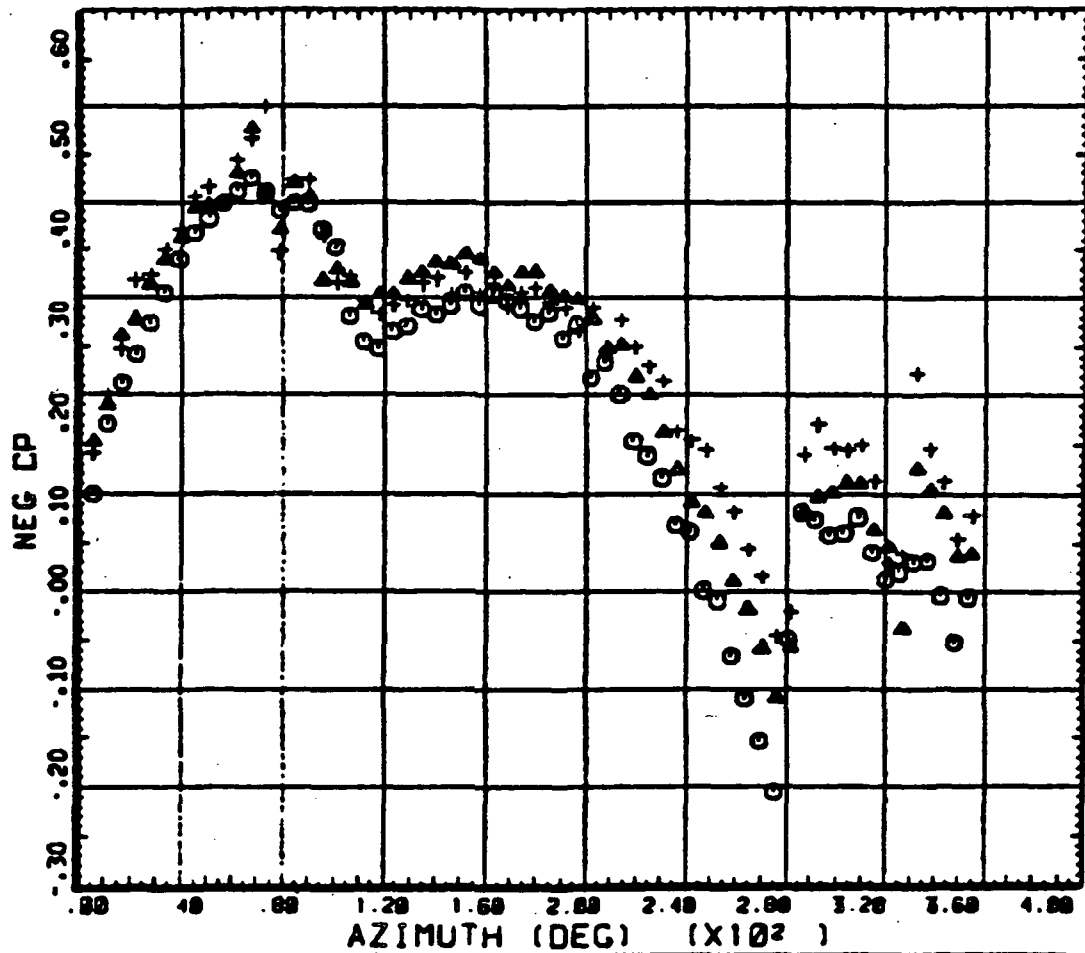


Figure 49. Azimuthal variation of pressure coefficient for 3 different rates of descent. Upper surface, 75 percent radius, 15 percent chord.

ORIGINAL PAGE IS  
OF POOR QUALITY



○ ○ ○	COUNTER 75	3158 R/RADIUS BLADE STATIC	GROSS WT LONG CG PRESSURE COEFF	SHIP MODEL AH-1G BOTTOM SURFACE
▲ ▲ ▲	COUNTER 75	3151 R/RADIUS BLADE STATIC	GROSS WT LONG CG PRESSURE COEFF	SHIP MODEL AH-1G BOTTOM SURFACE
+ + +	COUNTER 75	3152 R/RADIUS BLADE STATIC	GROSS WT LONG CG PRESSURE COEFF	SHIP MODEL AH-1G BOTTOM SURFACE

Figure 50. Azimuthal variation of pressure coefficient for 3 different rates of descent. Lower surface, 75 percent radius, 15 percent chord.

ORIGINAL PAGE IS  
OF POOR QUALITY

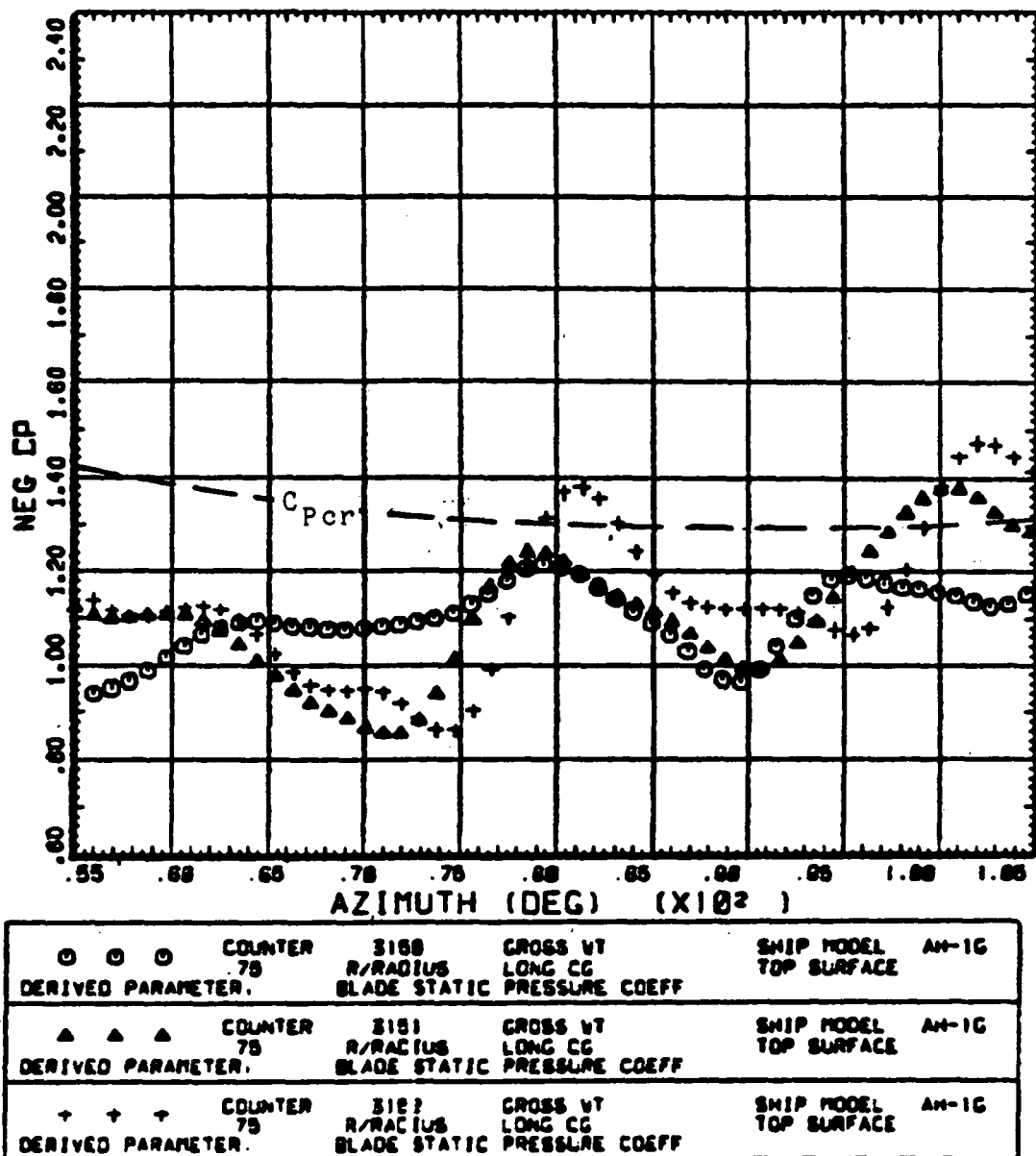
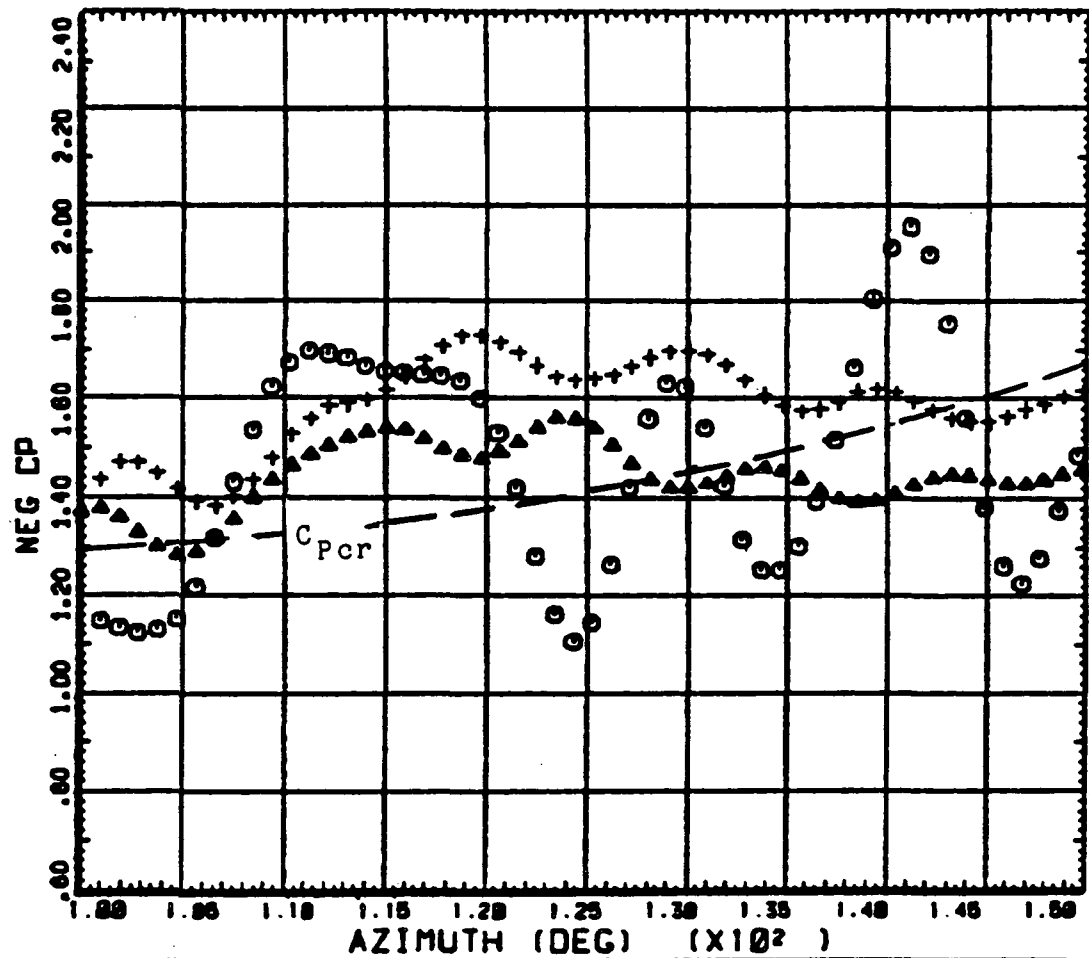


Figure 51. Azimuthal variation of pressure coefficient for 3 different rates of descent, expanded scale. Upper surface, 75 percent radius, 3 percent chord.



○ ○ ○ COUNTER 75 DERIVED PARAMETER.	3150 R/RADIUS BLADE STATIC	GROSS VT LONG CG PRESSURE COEFF	SHIP MODEL AM-1G TOP SURFACE
▲ ▲ ▲ COUNTER 78 DERIVED PARAMETER.	3151 R/RADIUS BLADE STATIC	GROSS VT LONG CG PRESSURE COEFF	SHIP MODEL AM-1G TOP SURFACE
+ + + COUNTER 79 DERIVED PARAMETER.	3152 R/RADIUS BLADE STATIC	GROSS VT LONG CG PRESSURE COEFF	SHIP MODEL AM-1G TOP SURFACE

Figure 52. Azimuthal variation of pressure coefficient for 3 different rates of descent, expanded scale. Upper surface, 75 percent radius, 3 percent chord.

ORIGINAL PAGE IS  
OF POOR QUALITY

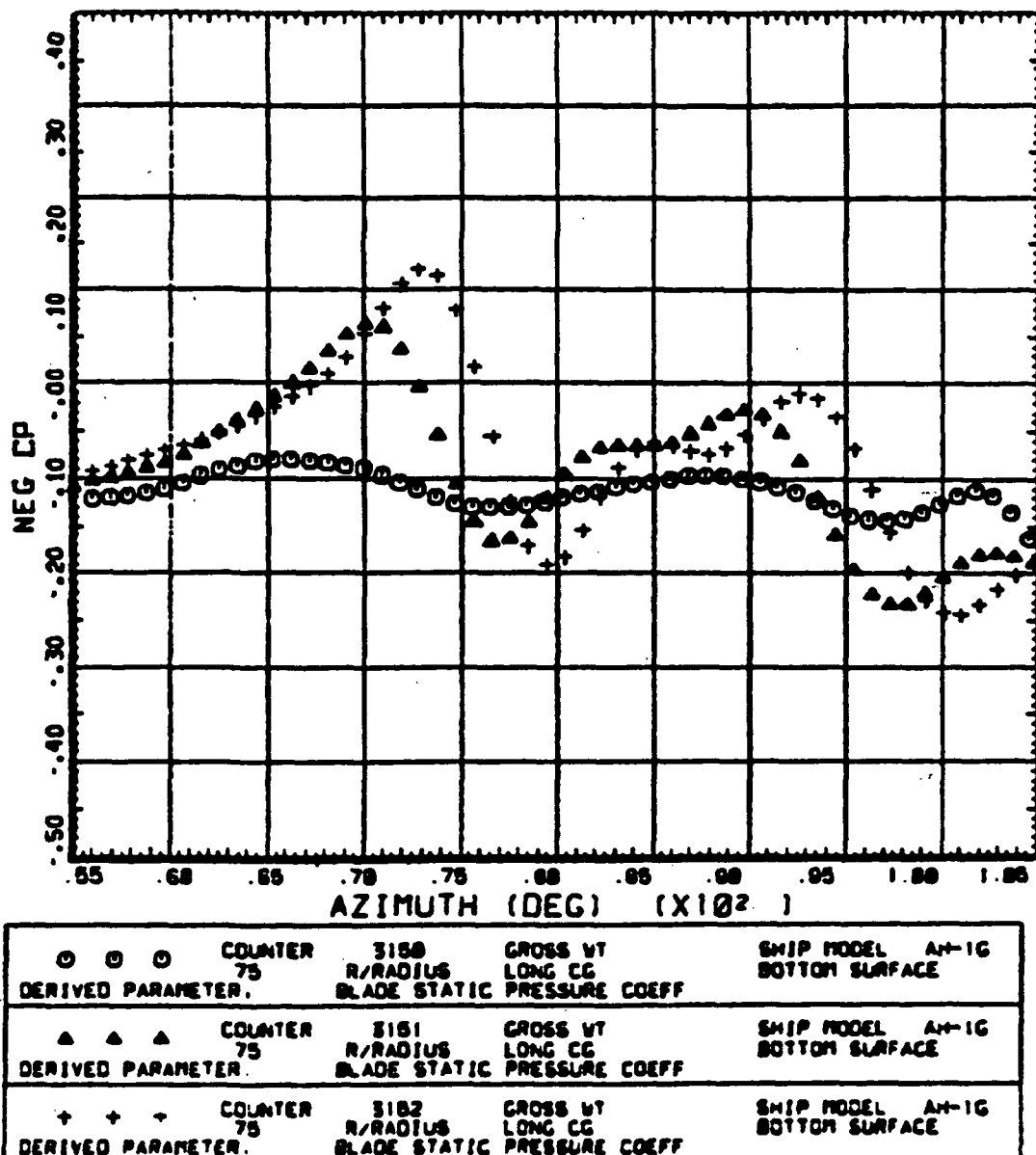
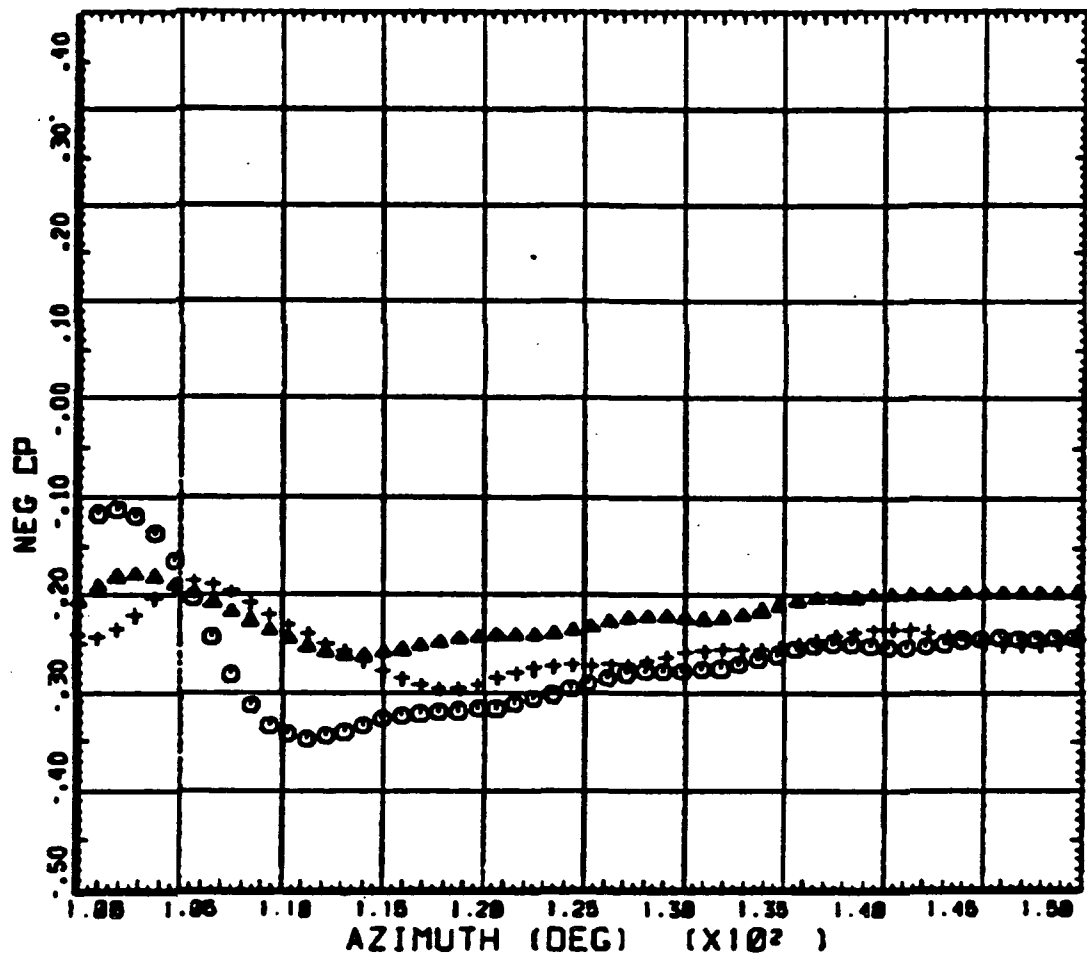


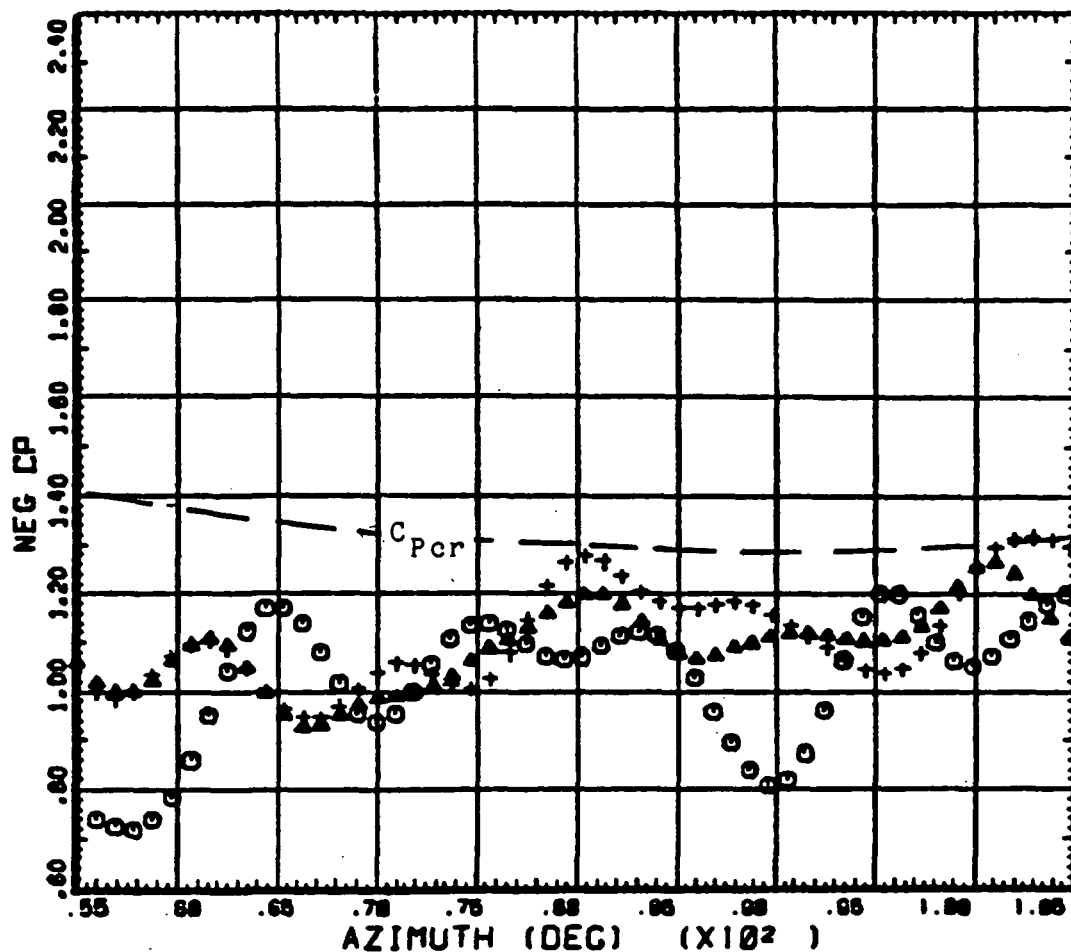
Figure 53. Azimuthal variation of pressure coefficient for 3 different rates of descent, expanded scale. Lower surface, 75 percent radius, 3 percent chord.



○ ○ ○	COUNTER 78	3150 R/RADIUS BLADE STATIC DERIVED PARAMETER.	GROSS WT LONG CG PRESSURE COEFF	SHIP MODEL AM-1G BOTTOM SURFACE
▲ ▲ ▲	COUNTER 78	3151 R/RADIUS BLADE STATIC DERIVED PARAMETER.	GROSS WT LONG CG PRESSURE COEFF	SHIP MODEL AM-1G BOTTOM SURFACE
++ +	COUNTER 78	3152 R/RADIUS BLADE STATIC DERIVED PARAMETER.	GROSS WT LONG CG PRESSURE COEFF	SHIP MODEL AM-1G BOTTOM SURFACE

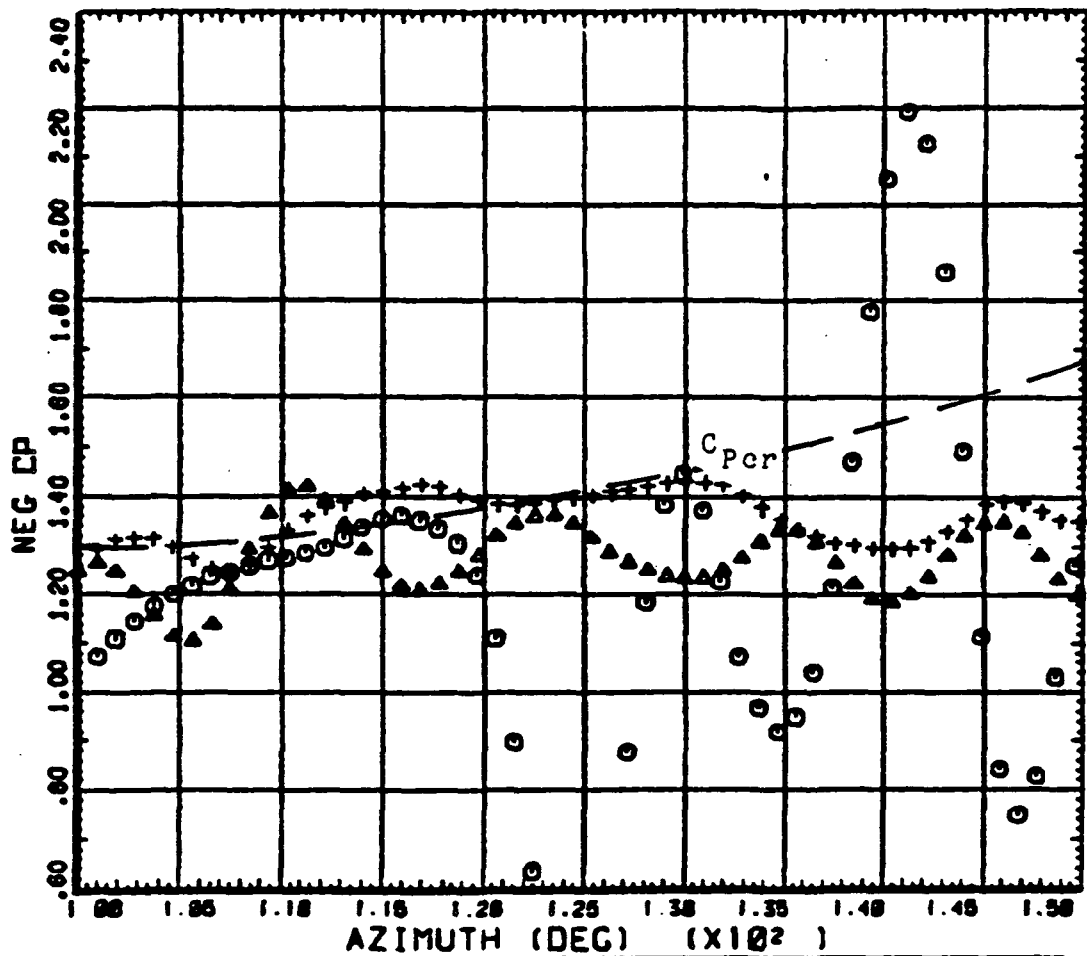
Figure 54. Azimuthal variation of pressure coefficient for 3 different rates of descent, expanded scale. Lower surface, 75 percent radius, 3 percent chord.

ORIGINAL PAGE IS  
OF POOR QUALITY



○ ○ ○	COUNTER .75 DERIVED PARAMETER.	3150 R/RADIUS BLADE STATIC	GROSS VT LONG CG PRESSURE COEFF	SHIP MODEL AM-1G TOP SURFACE
▲ ▲ ▲	COUNTER .78 DERIVED PARAMETER.	3151 R/RADIUS BLADE STATIC	GROSS VT LONG CG PRESSURE COEFF	SHIP MODEL AM-1G TOP SURFACE
† † †	COUNTER .78 DERIVED PARAMETER.	3152 R/RADIUS BLADE STATIC	GROSS VT LONG CG PRESSURE COEFF	SHIP MODEL AM-1G TOP SURFACE

Figure 55. Azimuthal variation of pressure coefficient for 3 different rates of descent, expanded scale. Upper surface, 75 percent radius, 8 percent chord.



○ ○ ○	COUNTER .75 DERIVED PARAMETER.	3150 R/RADIUS BLADE STATIC PRESSURE COEFF	GROSS WT LONG CG	SHIP MODEL AH-1G TOP SURFACE
△ △ △	COUNTER .75 DERIVED PARAMETER.	3151 R/RADIUS BLADE STATIC PRESSURE COEFF	GROSS WT LONG CG	SHIP MODEL AH-1G TOP SURFACE
+++	COUNTER .75 DERIVED PARAMETER.	3152 R/RADIUS BLADE STATIC PRESSURE COEFF	GROSS WT LONG CG	SHIP MODEL AH-1G TOP SURFACE

Figure 56. Azimuthal variation of pressure coefficient for 3 different rates of descent, expanded scale. Upper surface, 75 percent radius, 8 percent chord.

ORIGINAL PAGE IS  
OF POOR QUALITY

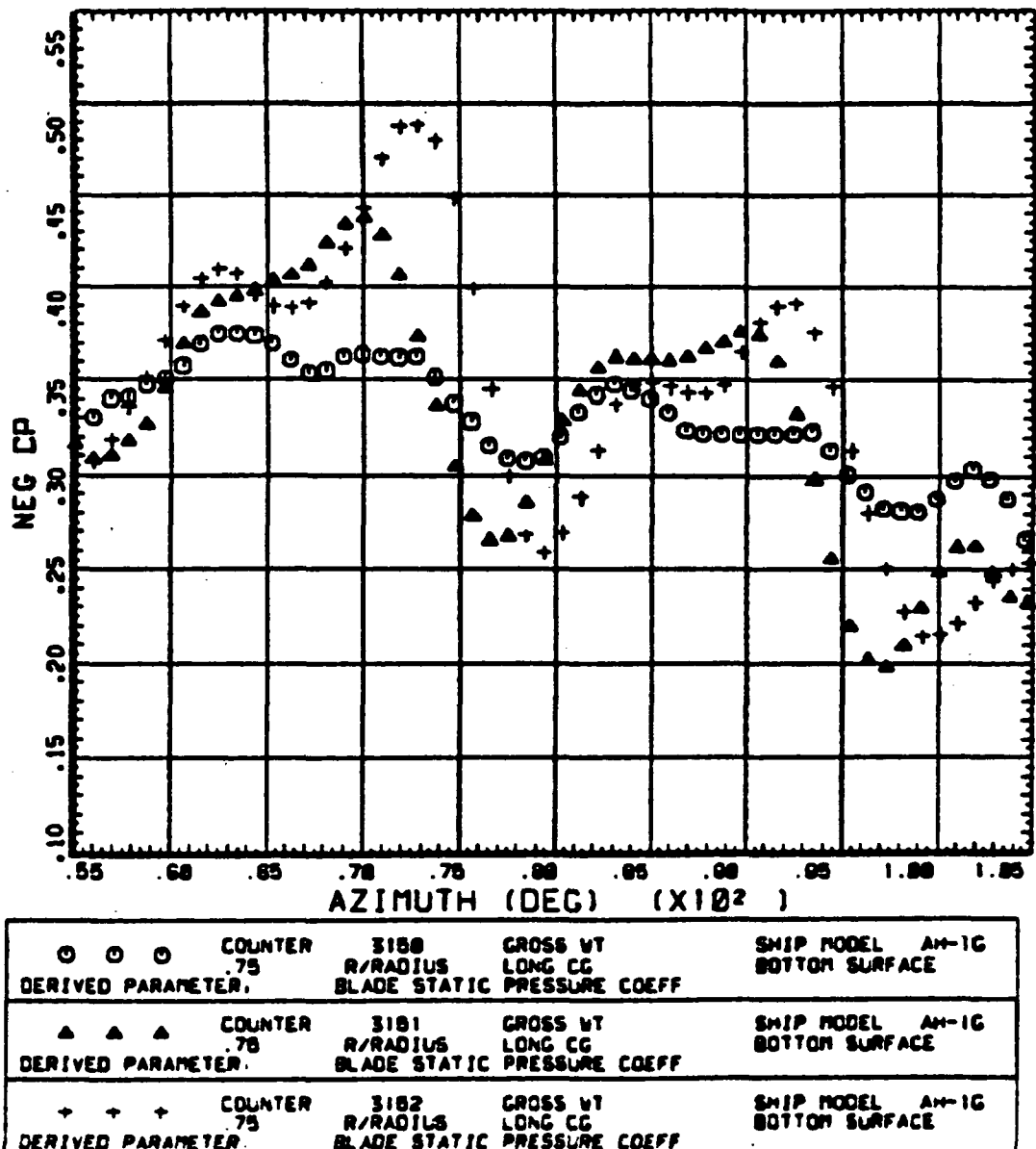
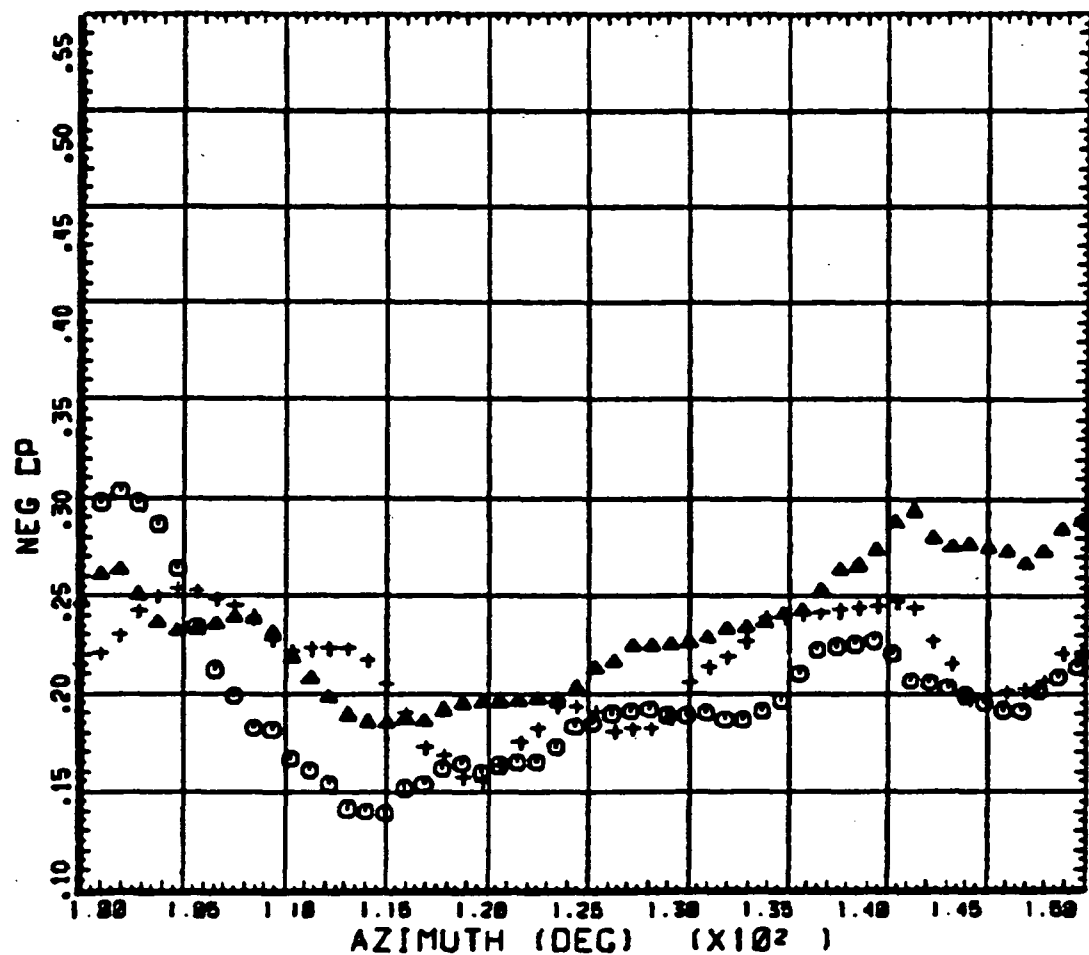


Figure 57. Azimuthal variation of pressure coefficient for 3 different rates of descent, expanded scale. Lower surface, 75 percent radius, 8 percent chord.



○ ○ ○	COUNTER 75	3158 R/RADIUS BLADE STATIC	GROSS WT LONG CG PRESSURE COEFF	SHIP MODEL AM-1G BOTTOM SURFACE
▲ ▲ ▲	COUNTER 75	3161 R/RADIUS BLADE STATIC	GROSS WT LONG CG PRESSURE COEFF	SHIP MODEL AM-1G BOTTOM SURFACE
+ + +	COUNTER 75	3152 R/RADIUS BLADE STATIC	GROSS WT LONG CG PRESSURE COEFF	SHIP MODEL AM-1G BOTTOM SURFACE

Figure 58. Azimuthal variation of pressure coefficient for 3 different rates of descent, expanded scale. Lower surface, 75 percent radius, 8 percent chord.

ORIGINAL PAGE IS  
OF POOR QUALITY

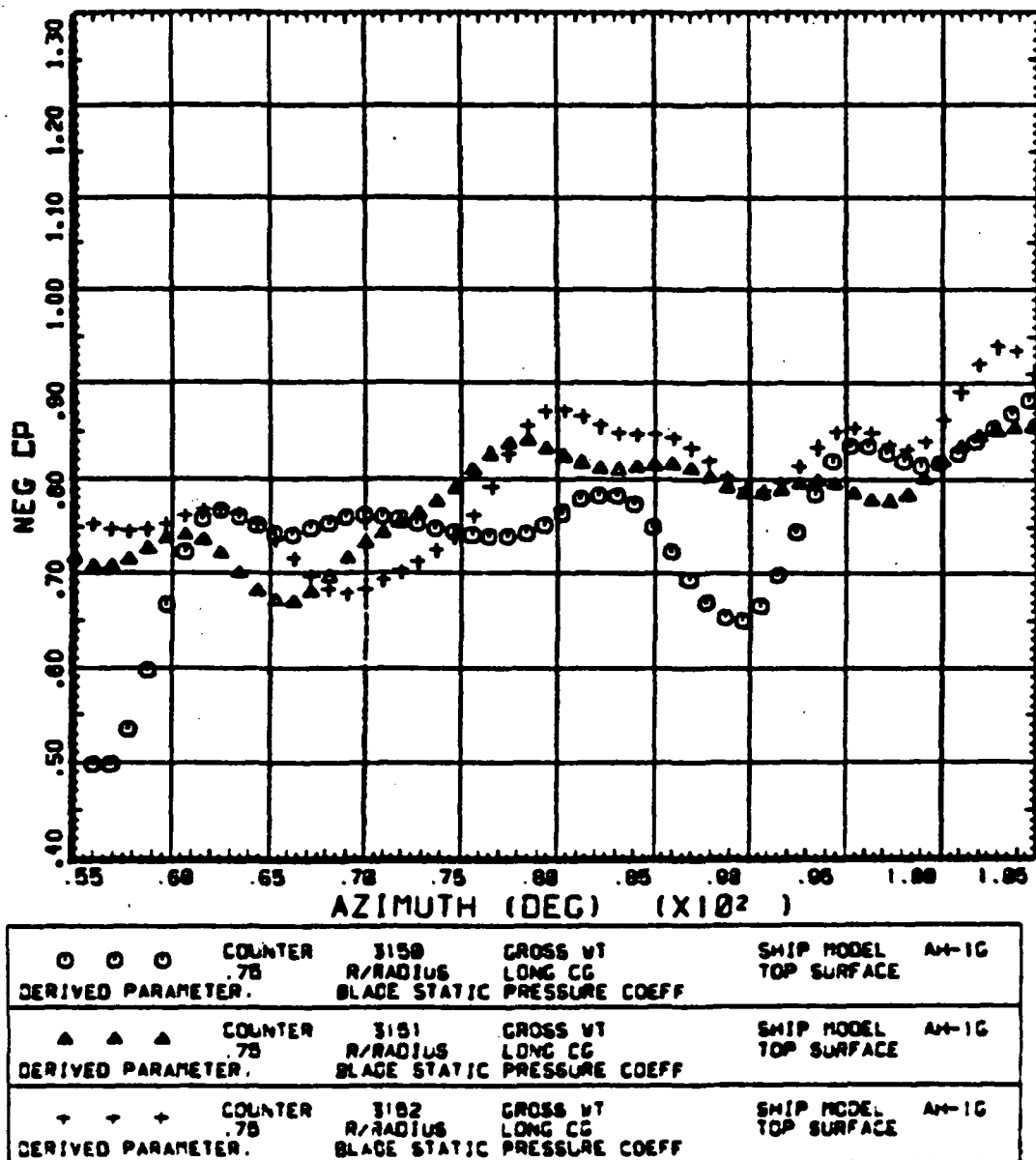
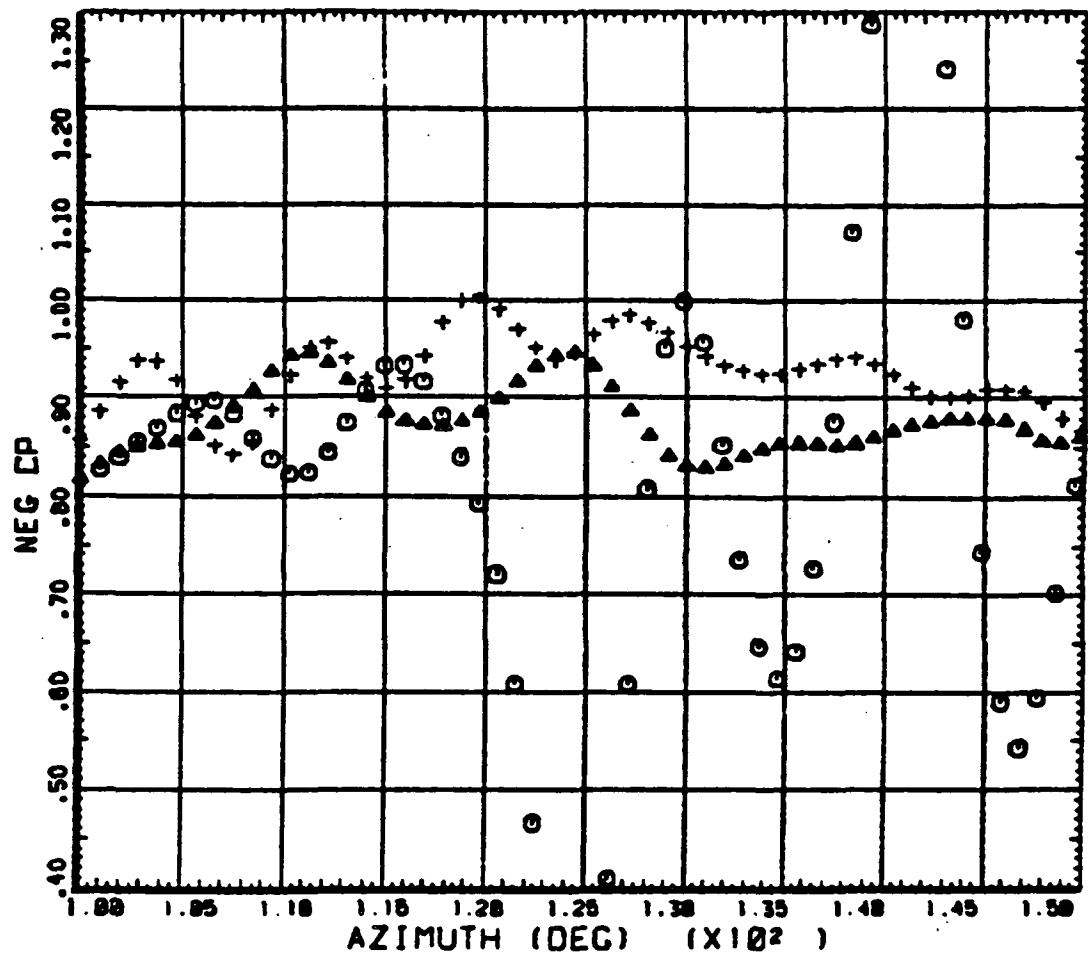


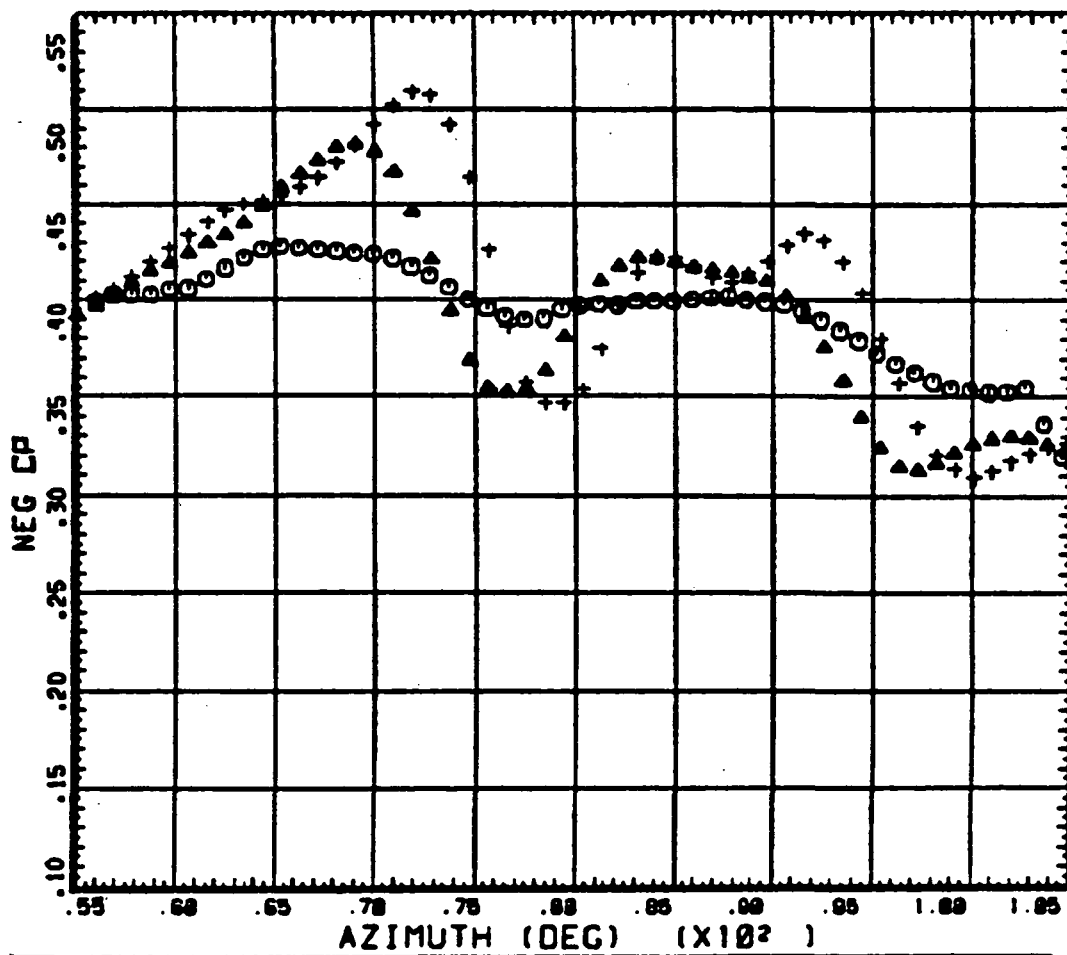
Figure 59. Azimuthal variation of pressure coefficient for 3 different rates of descent, expanded scale. Upper surface, 75 percent radius, 15 percent chord.



○ ○ ○ COUNTER DERIVED PARAMETER.	3158 R/RADIUS BLADE STATIC PRESSURE COEFF	GROSS WT LONG CG	SHIP MODEL TOP SURFACE AM-1G
▲ ▲ ▲ COUNTER DERIVED PARAMETER.	3151 R/RADIUS BLADE STATIC PRESSURE COEFF	GROSS WT LONG CG	SHIP MODEL TOP SURFACE AM-1G
+ + + COUNTER DERIVED PARAMETER.	3152 R/RADIUS BLADE STATIC PRESSURE COEFF	GROSS WT LONG CG	SHIP MODEL TOP SURFACE AM-1G

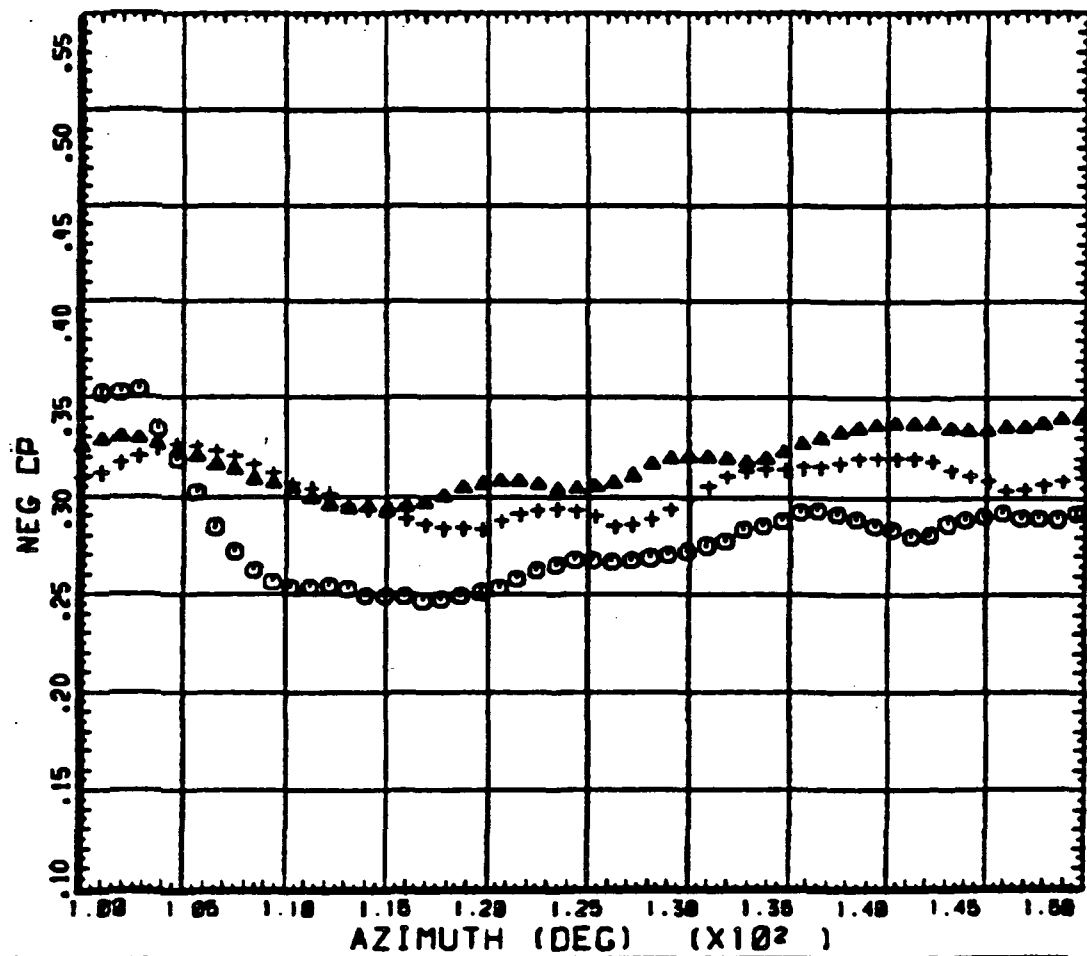
Figure 60. Azimuthal variation of pressure coefficient for 3 different rates of descent, expanded scale. Upper surface, 75 percent radius, 15 percent chord.

ORIGINAL PAGE IS  
OF POOR QUALITY



○ ○ ○	COUNTER 75 DERIVED PARAMETER.	3158 R/RADIUS BLADE STATIC PRESSURE COEFF	CROSS VT LONG CG	SHIP MODEL AM-1G BOTTOM SURFACE
▲ ▲ ▲	COUNTER 78 DERIVED PARAMETER.	3151 R/RADIUS BLADE STATIC PRESSURE COEFF	CROSS VT LONG CG	SHIP MODEL AM-1G BOTTOM SURFACE
+ + +	COUNTER 75 DERIVED PARAMETER.	3152 R/RADIUS BLADE STATIC PRESSURE COEFF	CROSS VT LONG CG	SHIP MODEL AM-1G BOTTOM SURFACE

Figure 61. Azimuthal variation of pressure coefficient for 3 different rates of descent, expanded scale. Lower surface, 75 percent radius, 15 percent chord.



○ ○ ○	COUNTER 78 DERIVED PARAMETER.	3150 R/RADIUS BLADE STATIC PRESSURE COEFF	GROSS WT LONG CG	SHIP MODEL AM-1G BOTTOM SURFACE
▲ ▲ ▲	COUNTER 78 DERIVED PARAMETER.	3151 R/RADIUS BLADE STATIC PRESSURE COEFF	GROSS WT LONG CG	SHIP MODEL AM-1G BOTTOM SURFACE
+++	COUNTER 75 DERIVED PARAMETER.	3152 R/RADIUS BLADE STATIC PRESSURE COEFF	GROSS WT LONG CG	SHIP MODEL AM-1G BOTTOM SURFACE

Figure 62. Azimuthal variation of pressure coefficient for 3 different rates of descent, expanded scale. Lower surface, 75 percent radius, 15 percent chord.

ORIGINAL PAGE IS  
OF POOR QUALITY

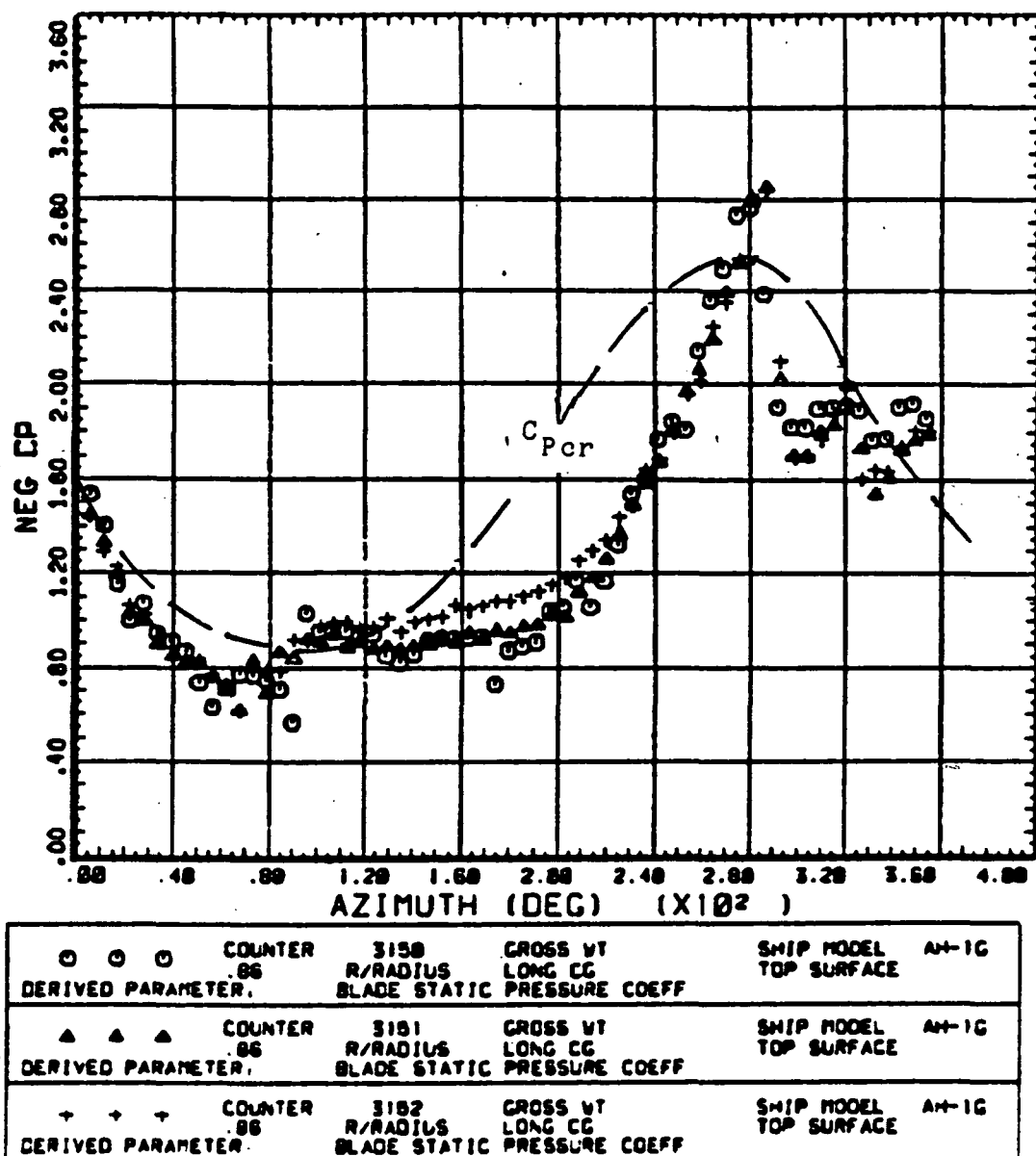
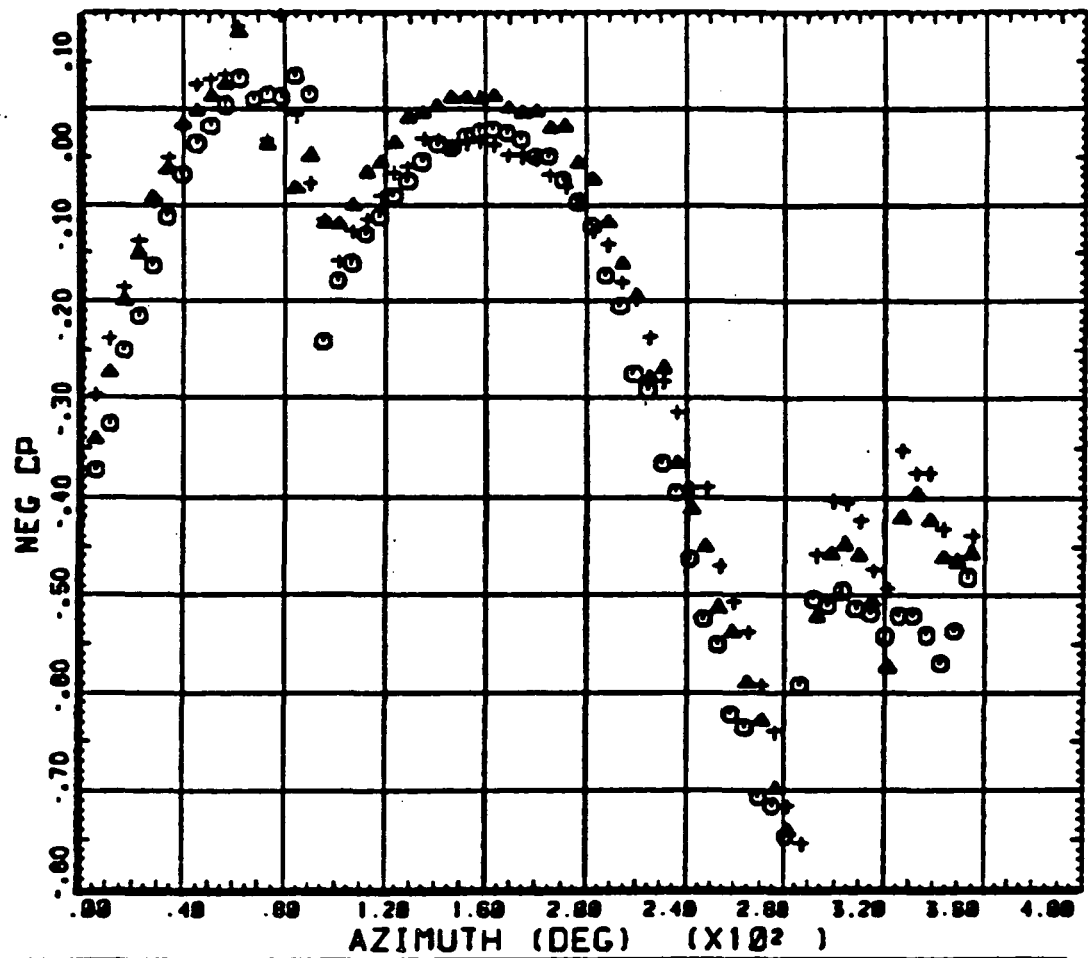


Figure 63. Azimuthal variation of pressure coefficient for 3 different rates of descent. Upper surface, 86 percent radius, 3 percent chord.



○ ○ ○	COUNTER 06	3188 R/RADIUS	GROSS VT LONG CG BLADE STATIC PRESSURE COEFF	SHIP MODEL AH-1G BOTTOM SURFACE
◆ ◆ ◆	COUNTER 08	3191 R/RADIUS	GROSS VT LONG CG BLADE STATIC PRESSURE COEFF	SHIP MODEL AH-1G BOTTOM SURFACE
† † †	COUNTER 08	3192 R/RADIUS	GROSS VT LONG CG BLADE STATIC PRESSURE COEFF	SHIP MODEL AH-1G BOTTOM SURFACE

Figure 64. Azimuthal variation of pressure coefficient for 3 different rates of descent. Lower surface, 86 percent radius, 3 percent chord.

ORIGINAL PAGE IS  
OF POOR QUALITY

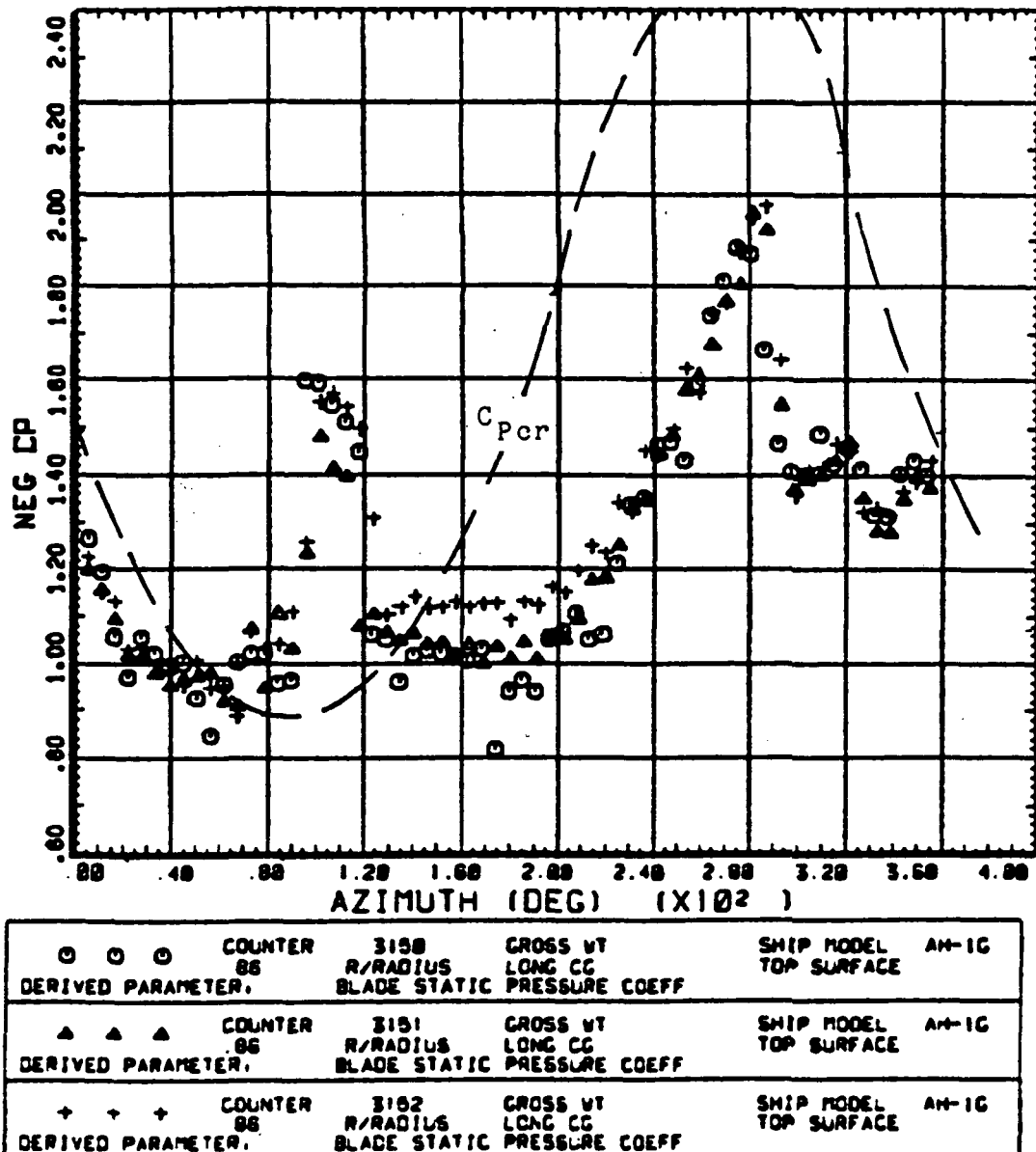
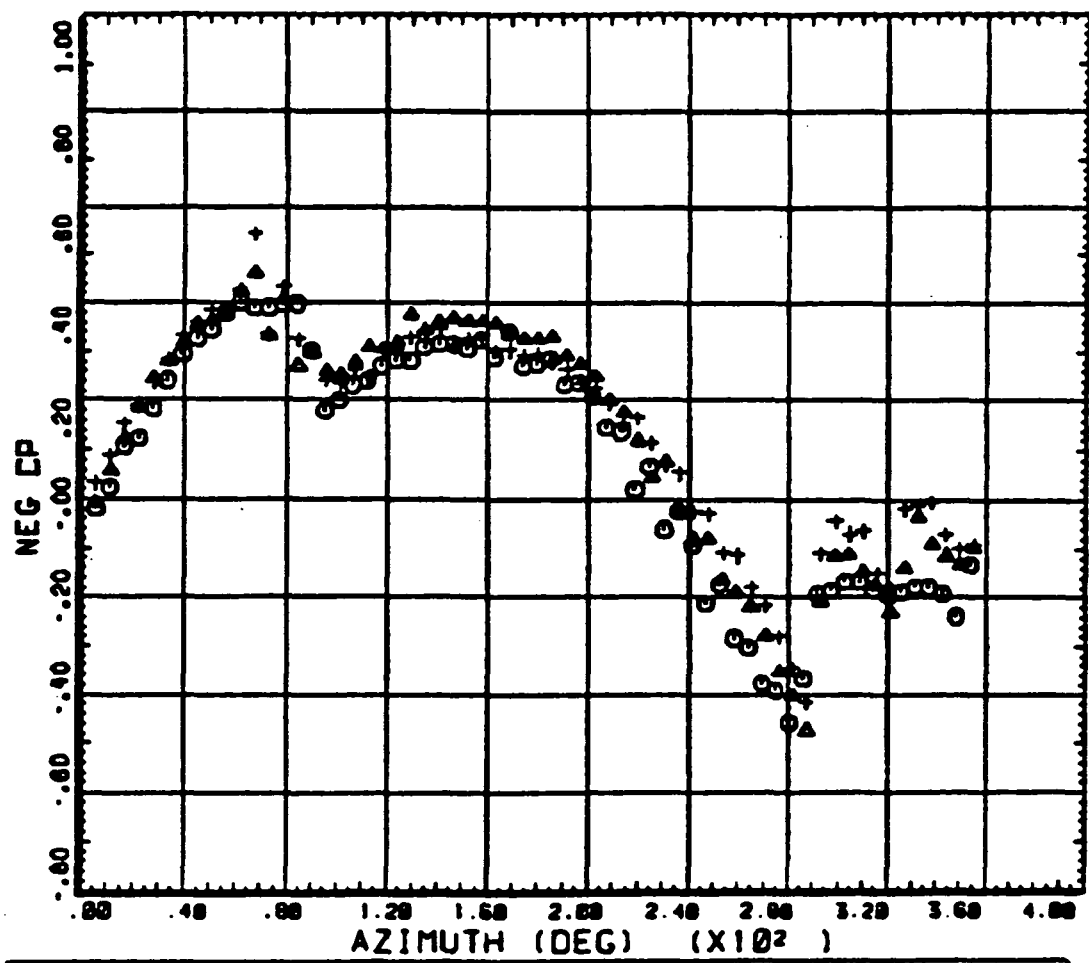


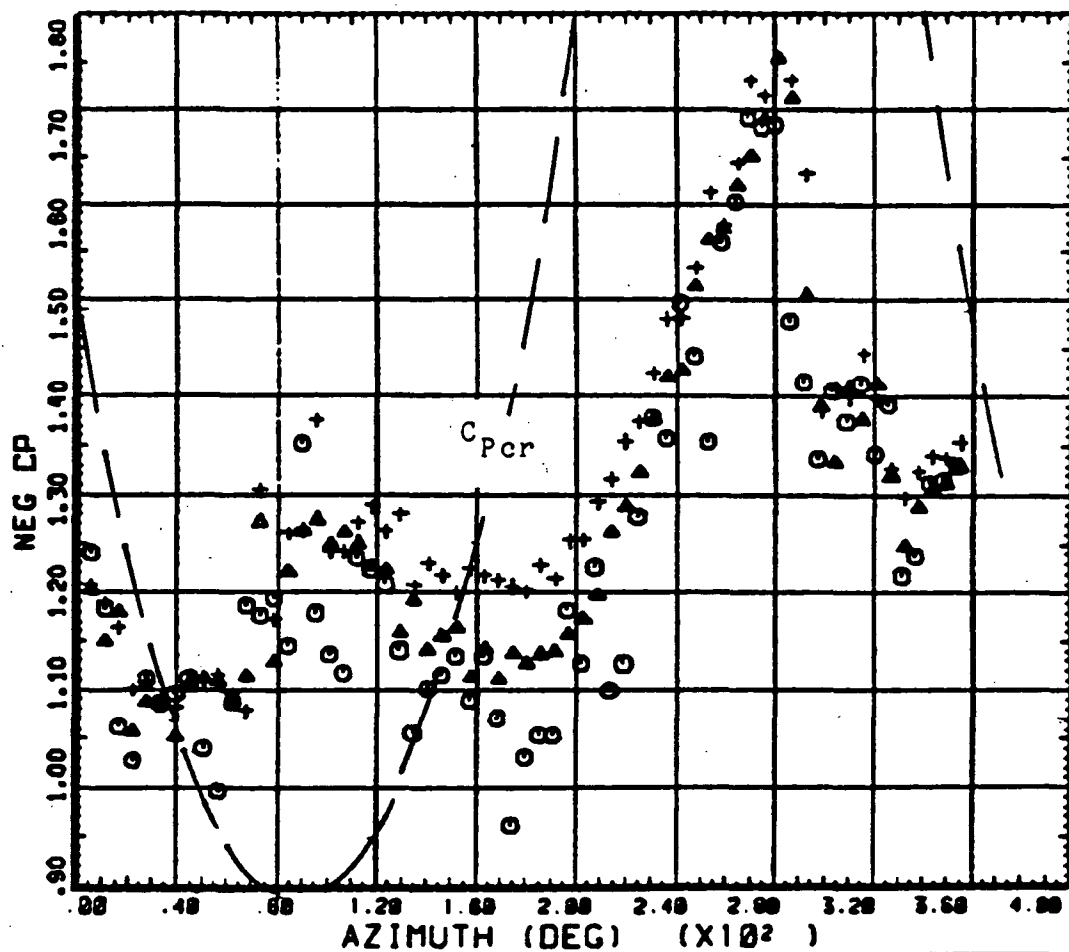
Figure 65. Azimuthal variation of pressure coefficient for 3 different rates of descent. Upper surface, 86 percent radius, 8 percent chord.



○ ○ ○	COUNTER 86	3150 R/RADIUS BLADE STATIC PRESSURE COEFF	GROSS VT LONG CG	SHIP MODEL AN-1G BOTTOM SURFACE
△ △ △	COUNTER 86	3151 R/RADIUS BLADE STATIC PRESSURE COEFF	GROSS VT LONG CG	SHIP MODEL AN-1G BOTTOM SURFACE
† † †	COUNTER 86	3152 R/RADIUS BLADE STATIC PRESSURE COEFF	GROSS VT LONG CG	SHIP MODEL AN-1G BOTTOM SURFACE

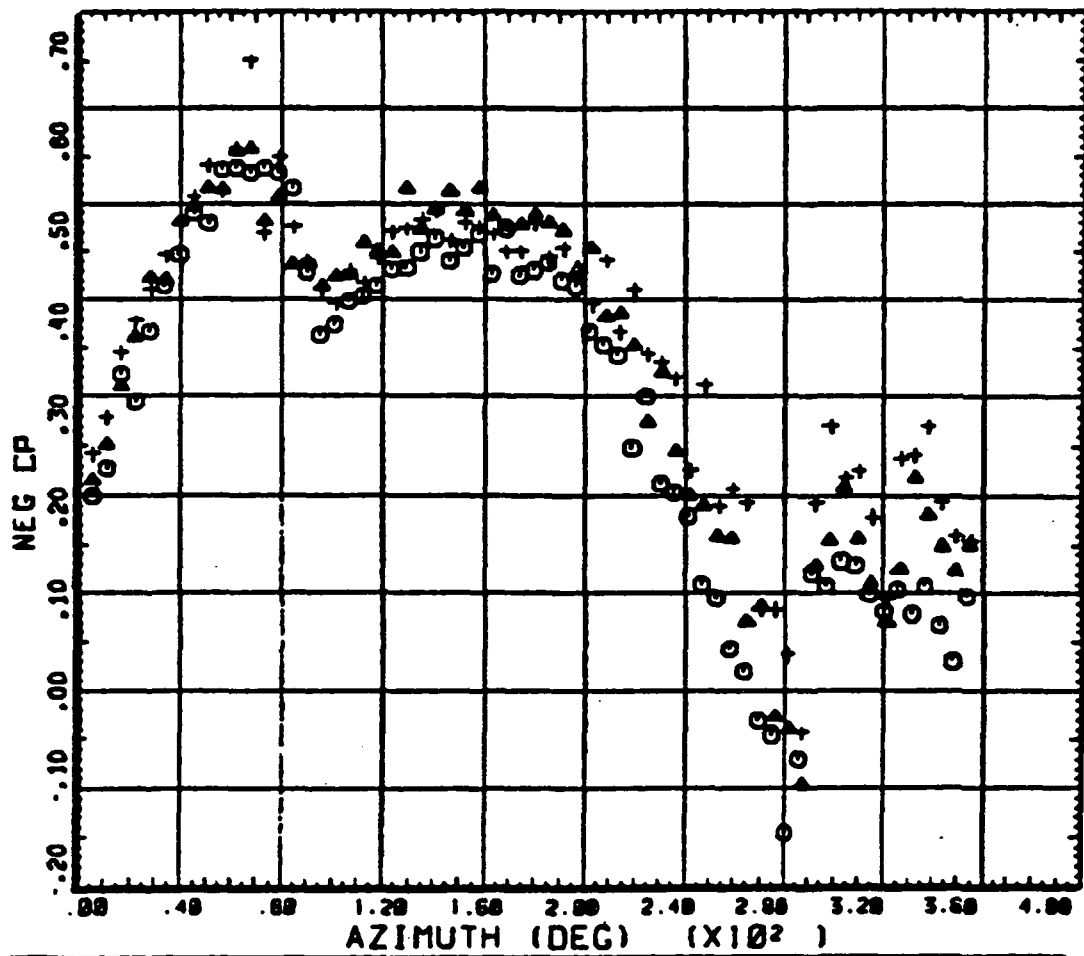
Figure 66. Azimuthal variation of pressure coefficient for 3 different rates of descent. Lower surface, 86 percent radius, 8 percent chord.

ORIGINAL PAGE IS  
OF POOR QUALITY



○ ○ ○	COUNTER 86	3150 R/RADIUS BLADE STATIC PRESSURE COEFF	GROSS WT LONG CG	SHIP MODEL AM-1G TOP SURFACE
▲ ▲ ▲	COUNTER 86	3151 R/RADIUS BLADE STATIC PRESSURE COEFF	GROSS WT LONG CG	SHIP MODEL AM-1G TOP SURFACE
+ + +	COUNTER 86	3152 R/RADIUS BLADE STATIC PRESSURE COEFF	GROSS WT LONG CG	SHIP MODEL AM-1G TOP SURFACE

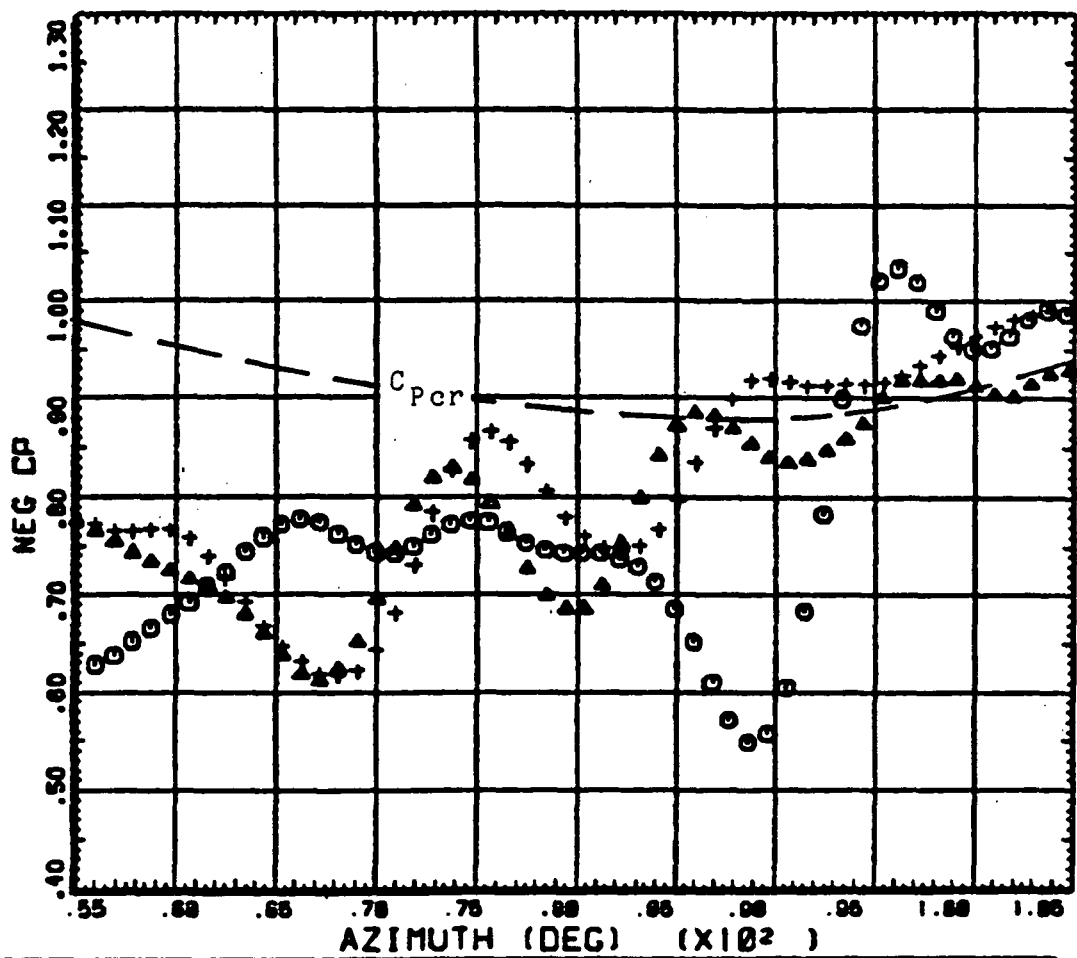
Figure 67. Azimuthal variation of pressure coefficient for 3 different rates of descent. Upper surface, 86 percent radius, 15 percent chord.



○ ○ ○	COUNTER	3150	GROSS WT	SHIP MODEL
.86	R/RADIUS	LONG CG	AM-1G	
DERIVED PARAMETER.	BLADE STATIC PRESSURE COEFF		BOTTOM SURFACE	
▲ ▲ ▲	COUNTER	3151	GROSS WT	SHIP MODEL
.88	R/RADIUS	LONG CG	AM-1G	
DERIVED PARAMETER.	BLADE STATIC PRESSURE COEFF		BOTTOM SURFACE	
+ + +	COUNTER	3152	GROSS WT	SHIP MODEL
.90	R/RADIUS	LONG CG	AM-1G	
DERIVED PARAMETER.	BLADE STATIC PRESSURE COEFF		BOTTOM SURFACE	

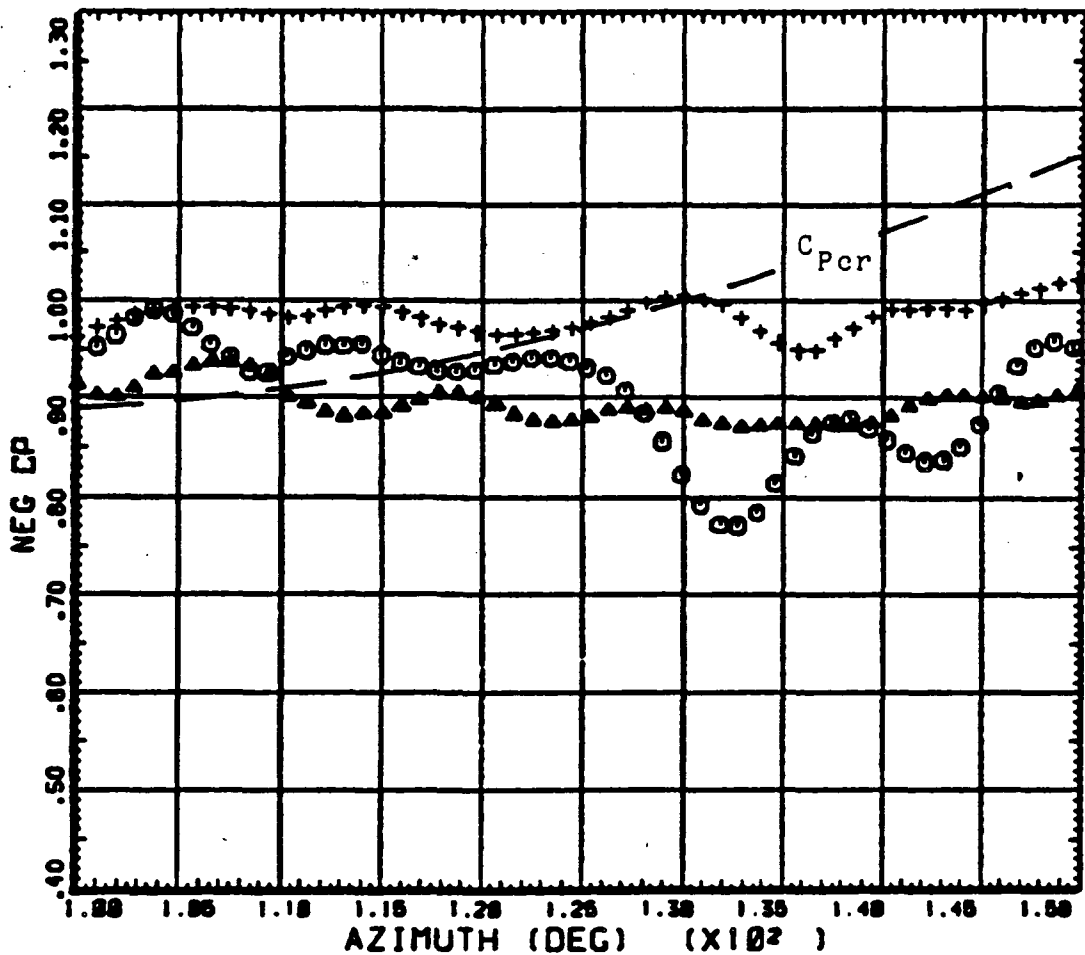
Figure 68. Azimuthal variation of pressure coefficient for 3 different rates of descent. Lower surface, 86 percent radius, 15 percent chord.

ORIGINAL PAGE IS  
OF POOR QUALITY.



○ ○ ○	COUNTER 86 DERIVED PARAMETER.	3180 R/RADIUS BLADE STATIC	GROSS WT LONG CG PRESSURE COEFF	ENIP MODEL TOP SURFACE AN-1G
▲ ▲ ▲	COUNTER 86 DERIVED PARAMETER.	3181 R/RADIUS BLADE STATIC	GROSS WT LONG CG PRESSURE COEFF	ENIP MODEL TOP SURFACE AN-1G
+ + +	COUNTER 86 DERIVED PARAMETER.	3182 R/RADIUS BLADE STATIC	GROSS WT LONG CG PRESSURE COEFF	ENIP MODEL TOP SURFACE AN-1G

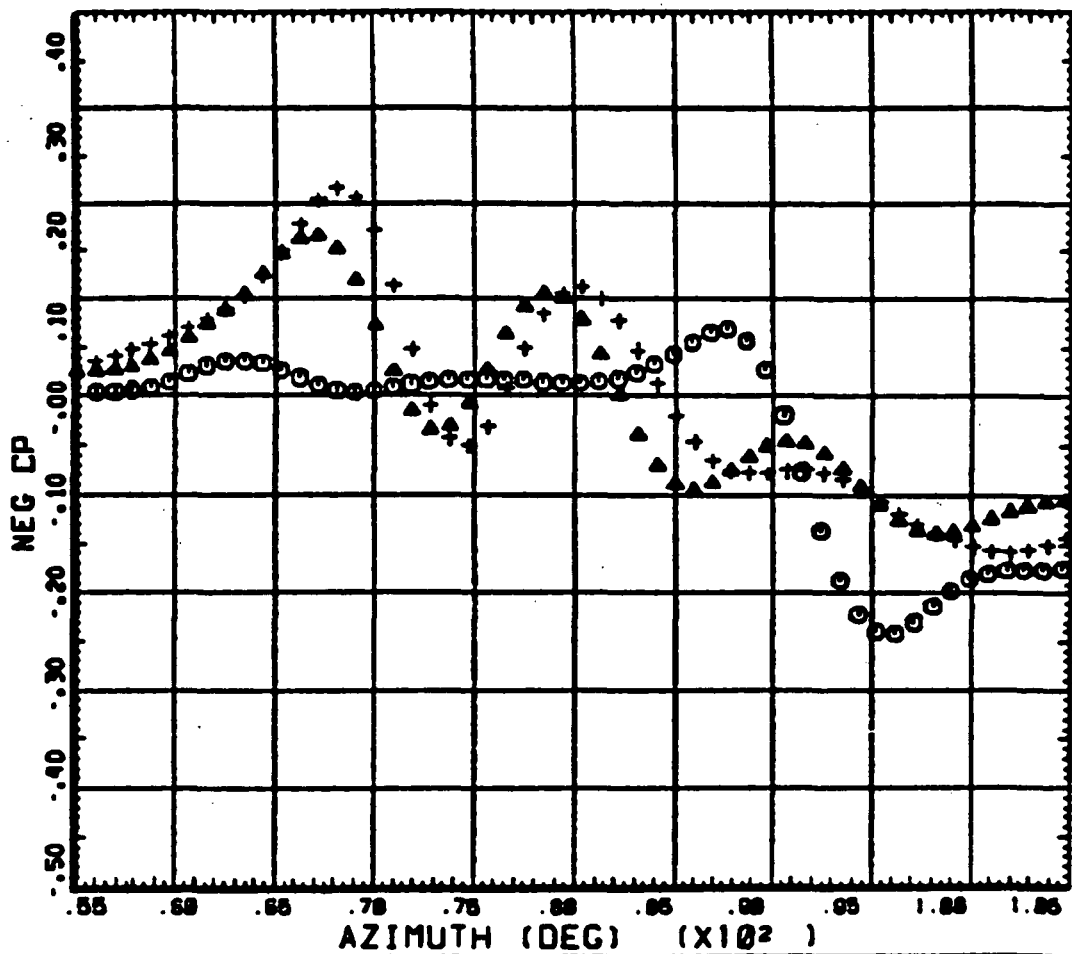
Figure 69. Azimuthal variation of pressure coefficient for 3 different rates of descent, expanded scale. Upper surface, 86 percent radius, 3 percent chord.



○ ○ ○	COUNTER 86	3150 R/RADIUS BLADE STATIC	GROSS WT LONG CG PRESSURE COEFF	SHIP MODEL TOP SURFACE	AM-1G
DERIVED PARAMETER.					
▲ ▲ ▲	COUNTER 86	3151 R/RADIUS BLADE STATIC	GROSS WT LONG CG PRESSURE COEFF	SHIP MODEL TOP SURFACE	AM-1G
DERIVED PARAMETER.					
+ + +	COUNTER 86	3152 R/RADIUS BLADE STATIC	GROSS WT LONG CG PRESSURE COEFF	SHIP MODEL TOP SURFACE	AM-1G
DERIVED PARAMETER.					

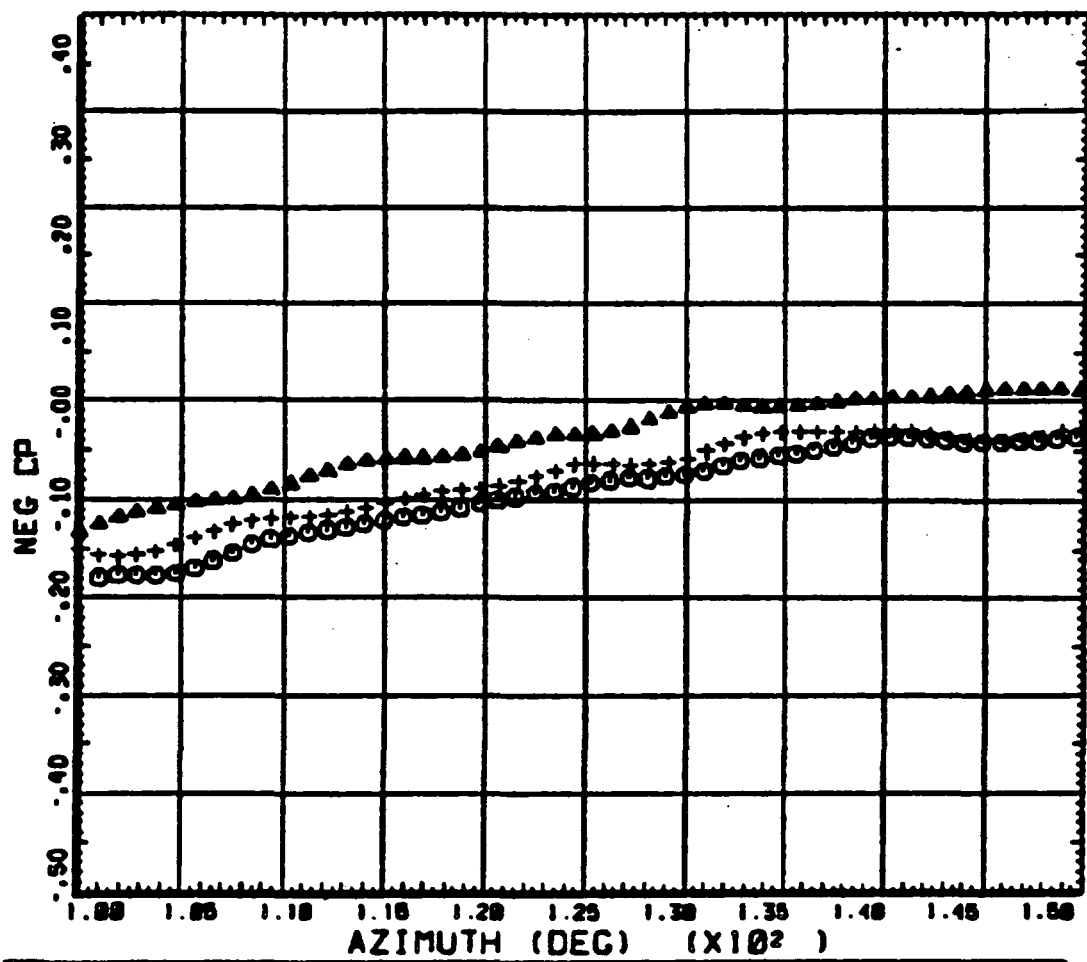
Figure 70. Azimuthal variation of pressure coefficient for 3 different rates of descent, expanded scale. Upper surface, 86 percent radius, 3 percent chord.

ORIGINAL PAGE IS  
OF POOR QUALITY



○ ○ ○	COUNTER 86	3150 R/RADIUS BLADE STATIC DERIVED PARAMETER.	GROSS WT LONG CG PRESSURE COEFF	SHIP MODEL AH-1G BOTTOM SURFACE
▲ ▲ ▲	COUNTER 86	3151 R/RADIUS BLADE STATIC DERIVED PARAMETER.	GROSS WT LONG CG PRESSURE COEFF	SHIP MODEL AH-1G BOTTOM SURFACE
+ + +	COUNTER 86	3152 R/RADIUS BLADE STATIC DERIVED PARAMETER.	GROSS WT LONG CG PRESSURE COEFF	SHIP MODEL AH-1G BOTTOM SURFACE

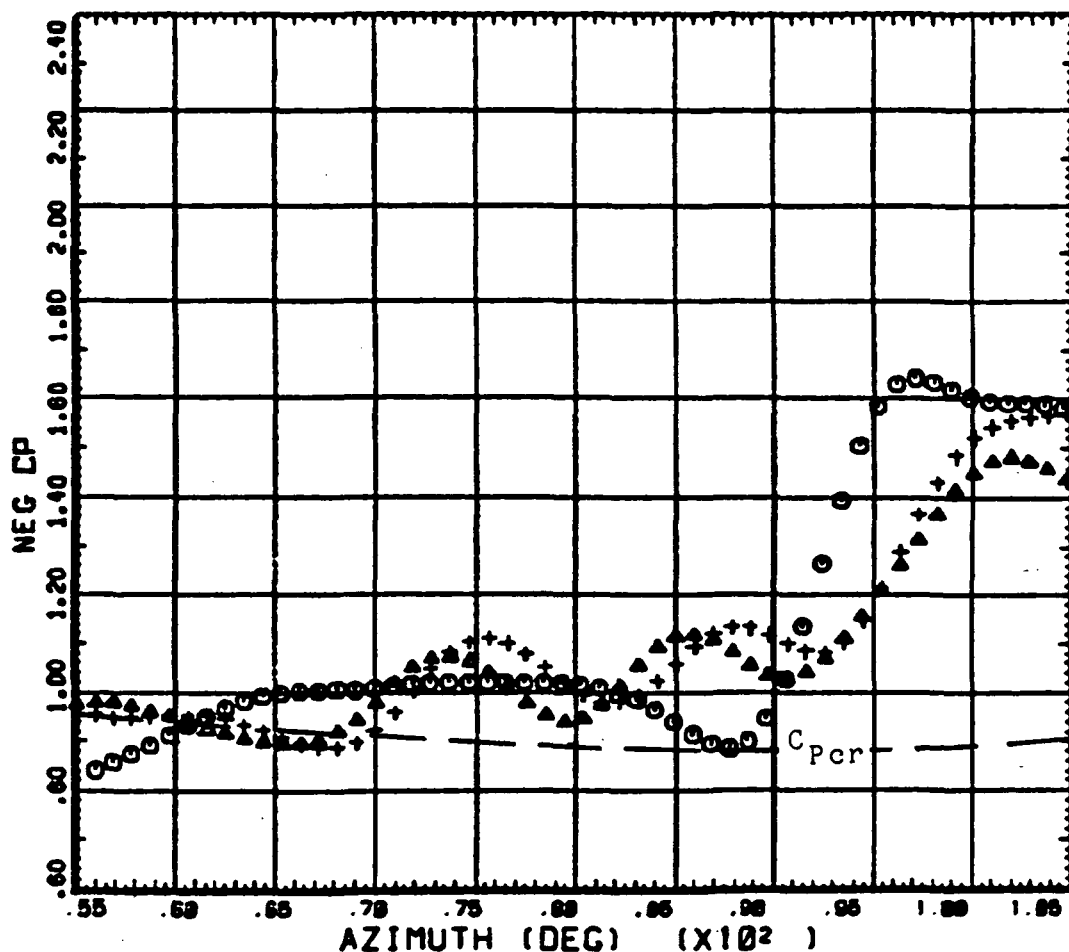
Figure 71. Azimuthal variation of pressure coefficient for 3 different rates of descent, expanded scale. Lower surface, 86 percent radius, 3 percent chord.



○ ○ ○	COUNTER .86	3150 R/RADIUS	GROSS WT LONG CG	SHIP MODEL AM-1G
DERIVED PARAMETER:		BLADE STATIC	PRESSURE COEFF	BOTTOM SURFACE
▲ ▲ ▲	COUNTER .86	3151 R/RADIUS	GROSS WT LONG CG	SHIP MODEL AM-1G
DERIVED PARAMETER:		BLADE STATIC	PRESSURE COEFF	BOTTOM SURFACE
+	+	COUNTER .86	3152 R/RADIUS	GROSS WT LONG CG
DERIVED PARAMETER:		BLADE STATIC	PRESSURE COEFF	BOTTOM SURFACE

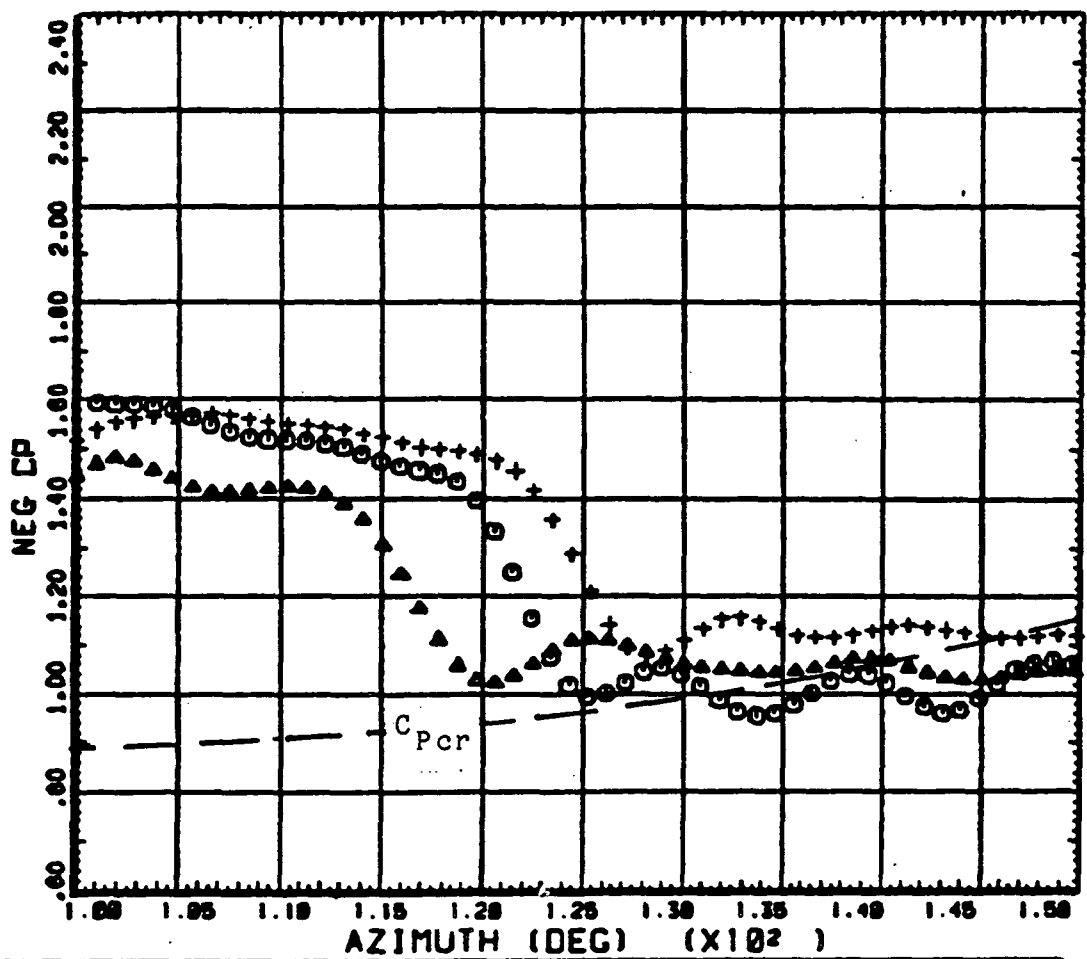
Figure 72. Azimuthal variation of pressure coefficient for 3 different rates of descent, expanded scale. Lower surface, 86 percent radius, 3 percent chord.

ORIGINAL PAGE IS  
OF POOR QUALITY



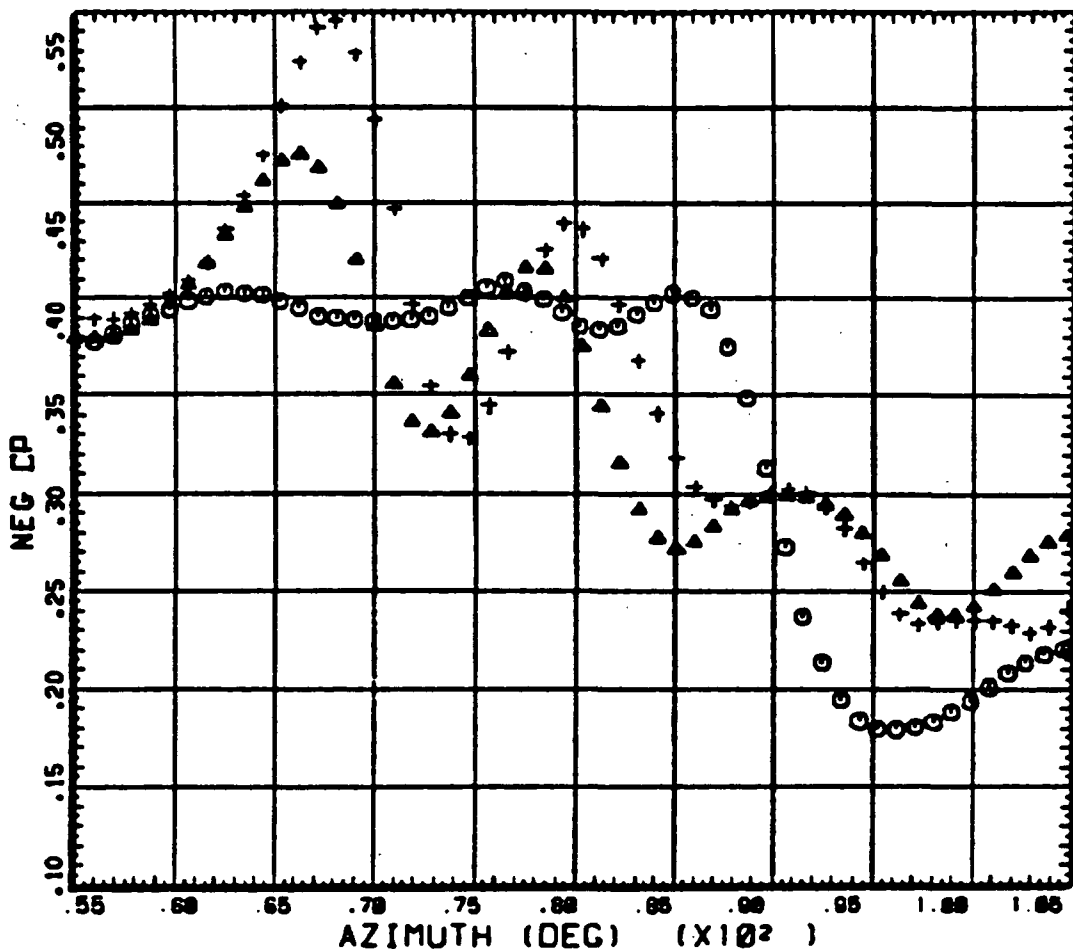
○ ○ ○ DERIVED PARAMETER.	COUNTER 86	3158 R/RADIUS BLADE STATIC PRESSURE COEFF	GROSS WT LONG CG	SHIP MODEL AM-1G TOP SURFACE
▲ ▲ ▲ DERIVED PARAMETER.	COUNTER 86	3151 R/RADIUS BLADE STATIC PRESSURE COEFF	GROSS WT LONG CG	SHIP MODEL AM-1G TOP SURFACE
† † † DERIVED PARAMETER.	COUNTER 86	3152 R/RADIUS BLADE STATIC PRESSURE COEFF	GROSS WT LONG CG	SHIP MODEL AM-1G TOP SURFACE

Figure 73. Azimuthal variation of pressure coefficient for 3 different rates of descent, expanded scale. Upper surface, 86 percent radius, 8 percent chord.



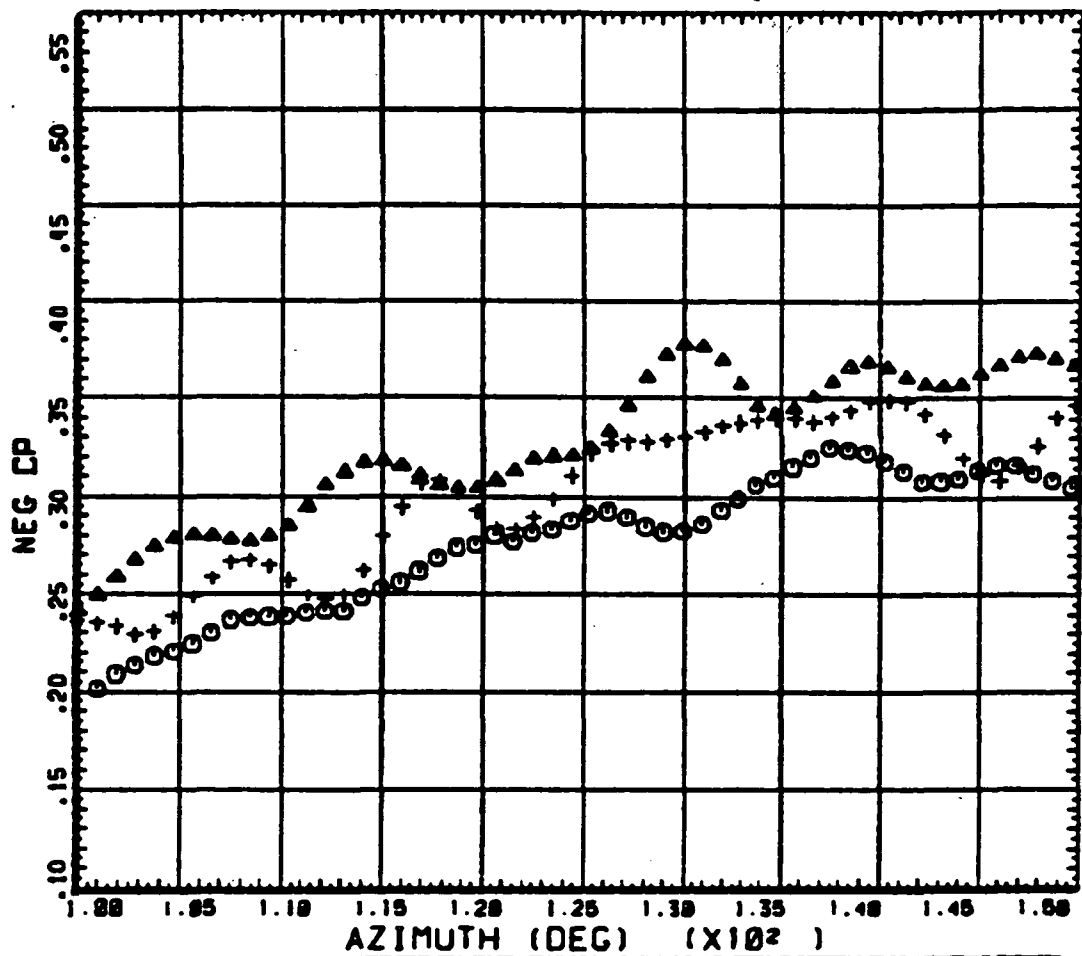
○ ○ ○	COUNTER 86	3150 R/RADIUS BLADE STATIC PRESSURE COEFF	GROSS VT LONG CG	SHIP MODEL AM-1G TOP SURFACE
△ △ △	COUNTER 86	3151 R/RADIUS BLADE STATIC PRESSURE COEFF	GROSS VT LONG CG	SHIP MODEL AM-1G TOP SURFACE
+ + +	COUNTER 86	3152 R/RADIUS BLADE STATIC PRESSURE COEFF	GROSS VT LONG CG	SHIP MODEL AM-1G TOP SURFACE

Figure 74. Azimuthal variation of pressure coefficient for 3 different rates of descent, expanded scale. Upper surface, 86 percent radius, 8 percent chord.



○ ○ ○ COUNTER 86 DERIVED PARAMETER.	3150 R/RADIUS BLADE STATIC PRESSURE COEFF	GROSS WT LONG CG	SHIP MODEL AM-1G BOTTOM SURFACE
▲ ▲ ▲ COUNTER 86 DERIVED PARAMETER	3151 R/RADIUS BLADE STATIC PRESSURE COEFF	GROSS WT LONG CG	SHIP MODEL AM-1G BOTTOM SURFACE
+ + + COUNTER 86 DERIVED PARAMETER	3152 R/RADIUS BLADE STATIC PRESSURE COEFF	GROSS WT LONG CG	SHIP MODEL AM-1G BOTTOM SURFACE

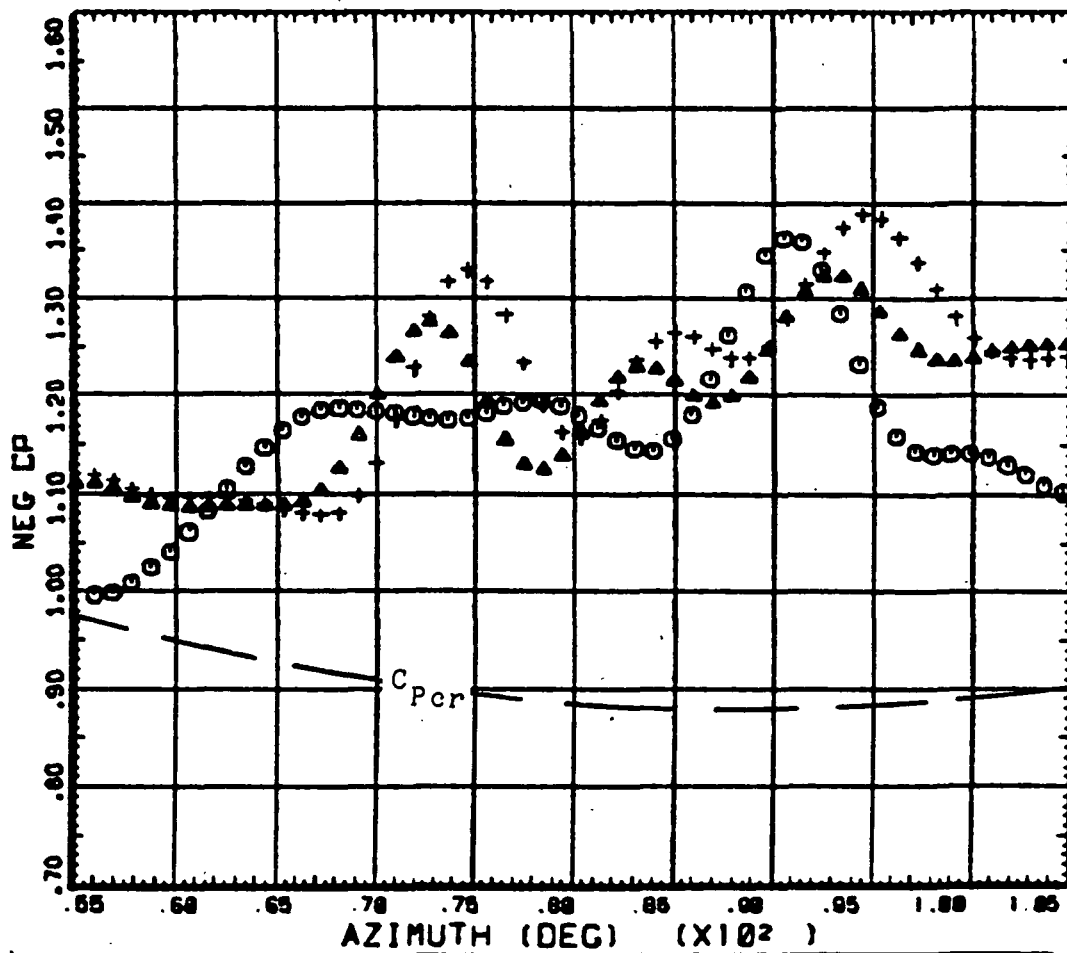
Figure 75. Azimuthal variation of pressure coefficient for 3 different rates of descent, expanded scale. Lower surface, 86 percent radius, 8 percent chord.



○ ○ ○ COUNTER DERIVED PARAMETER.	3150 R/RADIUS BLADE STATIC	GROSS WT LONG CG PRESSURE COEFF	SHIP MODEL AN-1G BOTTOM SURFACE
▲ ▲ ▲ COUNTER DERIVED PARAMETER.	3151 R/RADIUS BLADE STATIC	GROSS WT LONG CG PRESSURE COEFF	SHIP MODEL AN-1G BOTTOM SURFACE
+ + + COUNTER DERIVED PARAMETER.	3152 R/RADIUS BLADE STATIC	GROSS WT LONG CG PRESSURE COEFF	SHIP MODEL AN-1G BOTTOM SURFACE

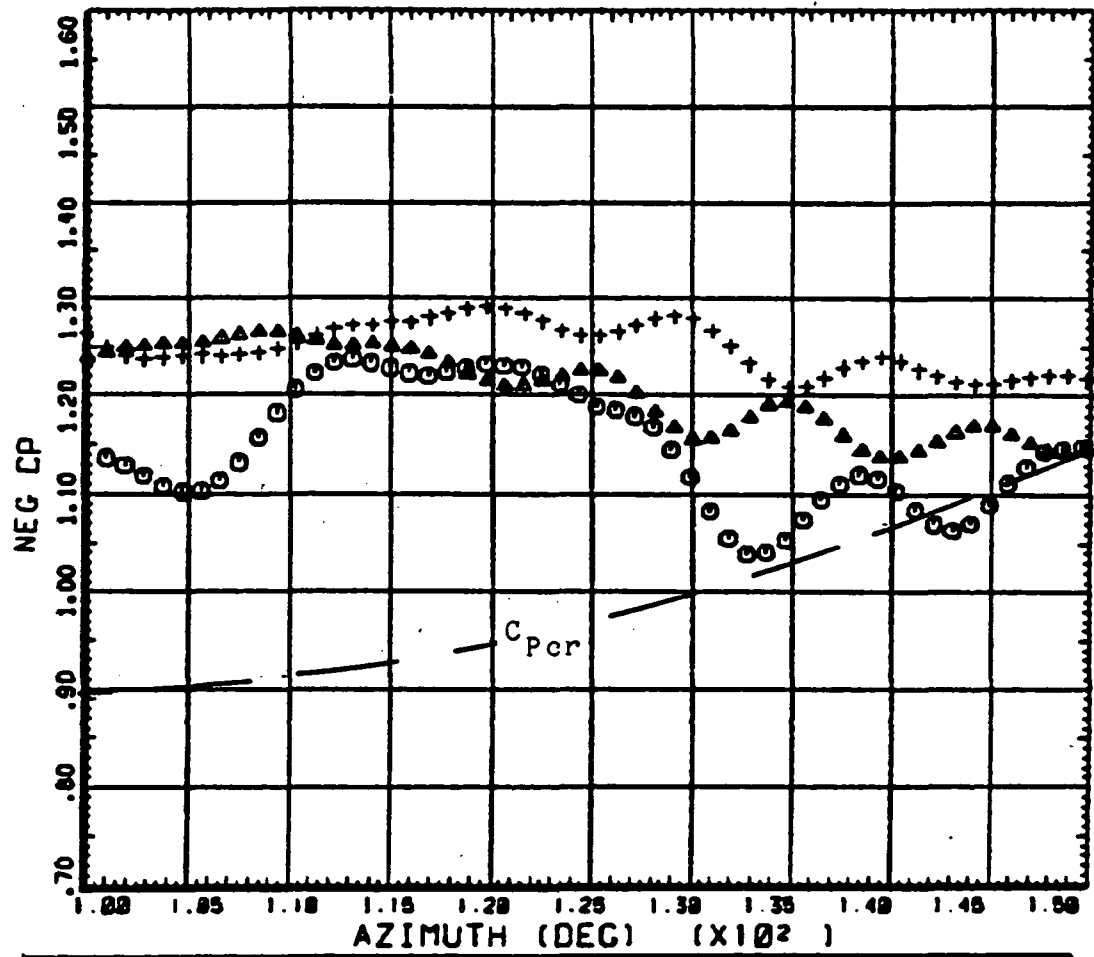
Figure 76. Azimuthal variation of pressure coefficient for 3 different rates of descent, expanded scale. Lower surface, 86 percent radius, 8 percent chord.

ORIGINAL PAGE IS  
OF POOR QUALITY



○ ○ ○	COUNTER 86	3158 R/RADIUS BLADE STATIC PRESSURE COEFF	GROSS VT LONG CG	SHIP MODEL AM-1G TOP SURFACE
△ △ △	COUNTER 86	3191 R/RADIUS BLADE STATIC PRESSURE COEFF	GROSS VT LONG CG	SHIP MODEL AM-1G TOP SURFACE
+ + +	COUNTER 86	3192 R/RADIUS BLADE STATIC PRESSURE COEFF	GROSS VT LONG CG	SHIP MODEL AM-1G TOP SURFACE

Figure 77. Azimuthal variation of pressure coefficient for 3 different rates of descent, expanded scale. Upper surface, 86 percent radius, 15 percent chord.



○ ○ ○ COUNTER DERIVED PARAMETER.	3150 R/RADIUS BLADE STATIC PRESSURE COEFF.	GROSS WT LONG CG	SHIP MODEL TOP SURFACE	AM-1G
▲ ▲ ▲ COUNTER DERIVED PARAMETER.	3151 R/RADIUS BLADE STATIC PRESSURE COEFF.	GROSS WT LONG CG	SHIP MODEL TOP SURFACE	AM-1G
+ + + COUNTER DERIVED PARAMETER.	3152 R/RADIUS BLADE STATIC PRESSURE COEFF.	GROSS WT LONG CG	SHIP MODEL TOP SURFACE	AM-1G

Figure 78. Azimuthal variation of pressure coefficient for 3 different rates of descent, expanded scale. Upper surface, 86 percent radius, 15 percent chord.

ORIGINAL PAGE IS  
OF POOR QUALITY

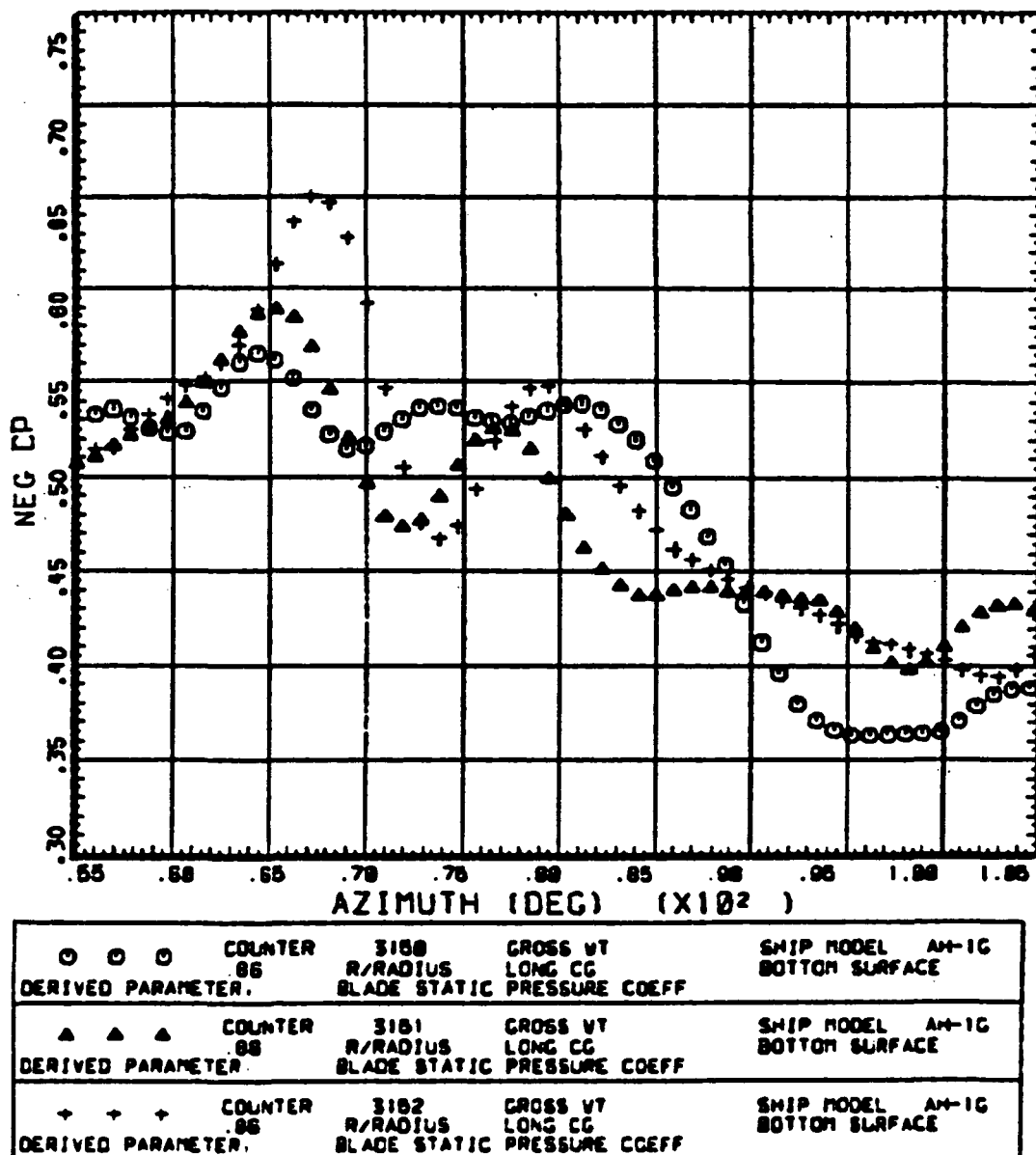
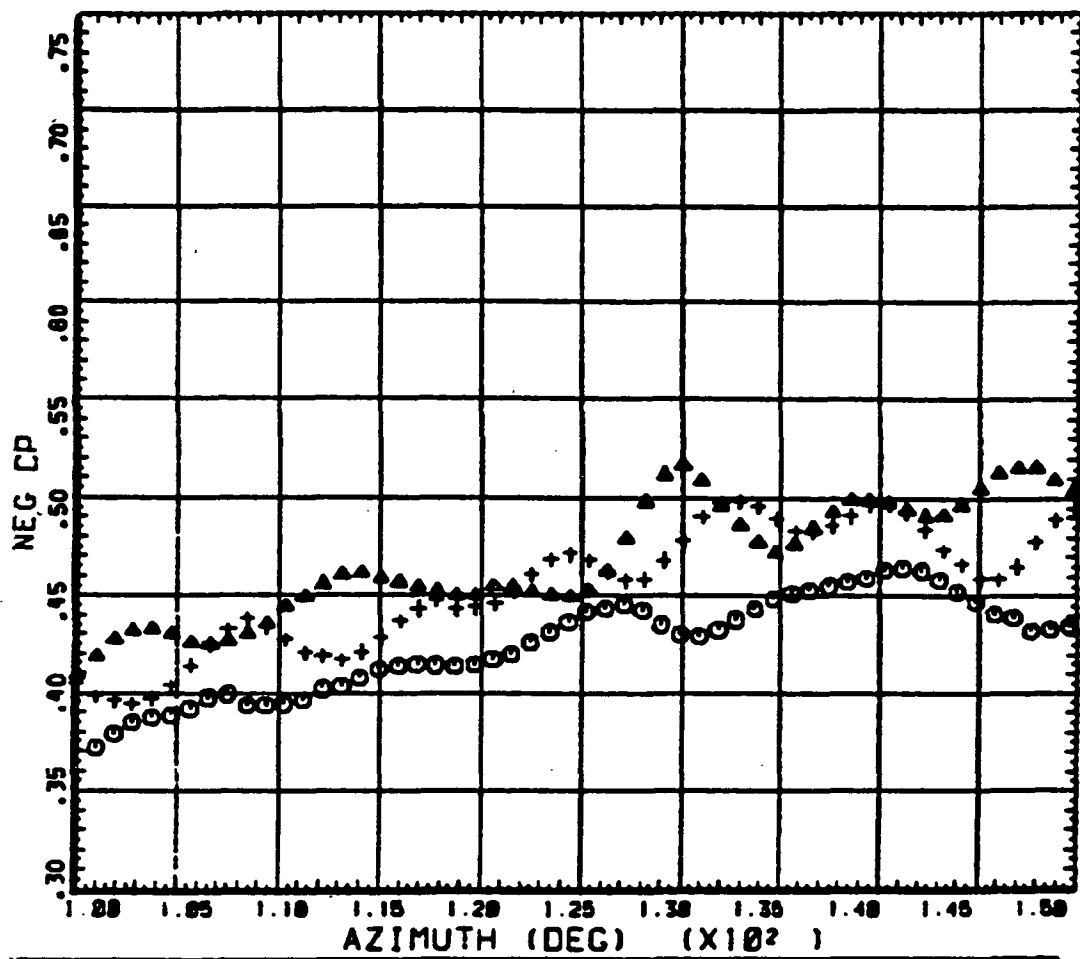


Figure 79. Azimuthal variation of pressure coefficient for 3 different rates of descent, expanded scale. Lower surface, 86 percent radius, 15 percent chord.



○ ○ ○	COUNTER .86	3150	GROSS WT	SHIP MODEL AM-1G
DERIVED PARAMETER,		R/RADIUS	LONG CG	BOTTOM SURFACE
△ △ △	COUNTER .88	3151	GROSS WT	SHIP MODEL AM-1G
DERIVED PARAMETER,		R/RADIUS	LONG CG	BOTTOM SURFACE
++ +	COUNTER .90	3152	GROSS WT	SHIP MODEL AM-1G
DERIVED PARAMETER,		R/RADIUS	LONG CG	BOTTOM SURFACE
		BLADE STATIC PRESSURE COEFF		

Figure 80. Azimuthal variation of pressure coefficient for 3 different rates of descent, expanded scale. Lower surface, 86 percent radius, 15 percent chord.

ORIGINAL PAGE IS  
OF POOR QUALITY

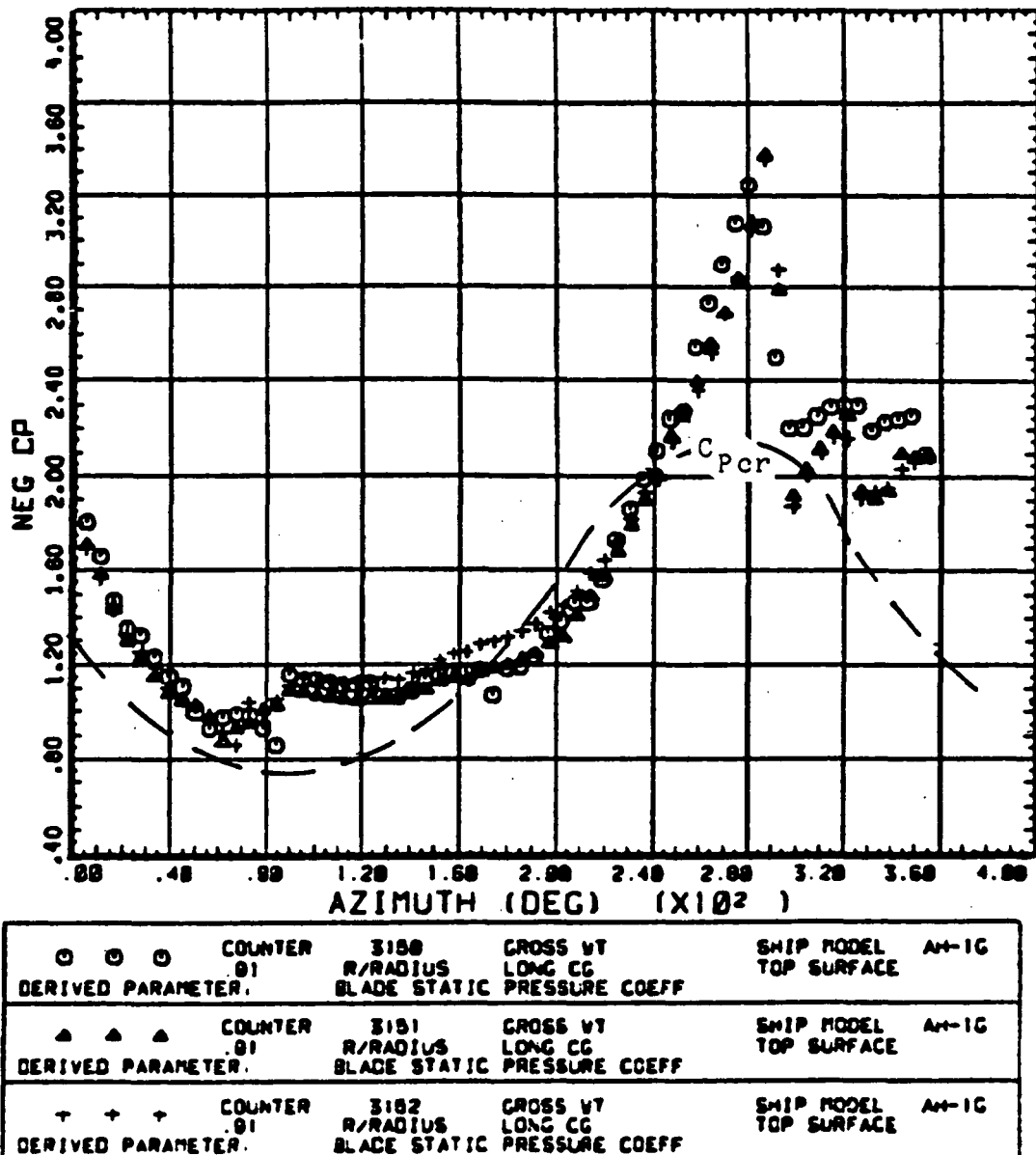


Figure 81. Azimuthal variation of pressure coefficient for 3 different rates of descent. Upper surface, 91 percent radius, 3 percent chord.

ORIGINAL PAGE IS  
OF POOR QUALITY

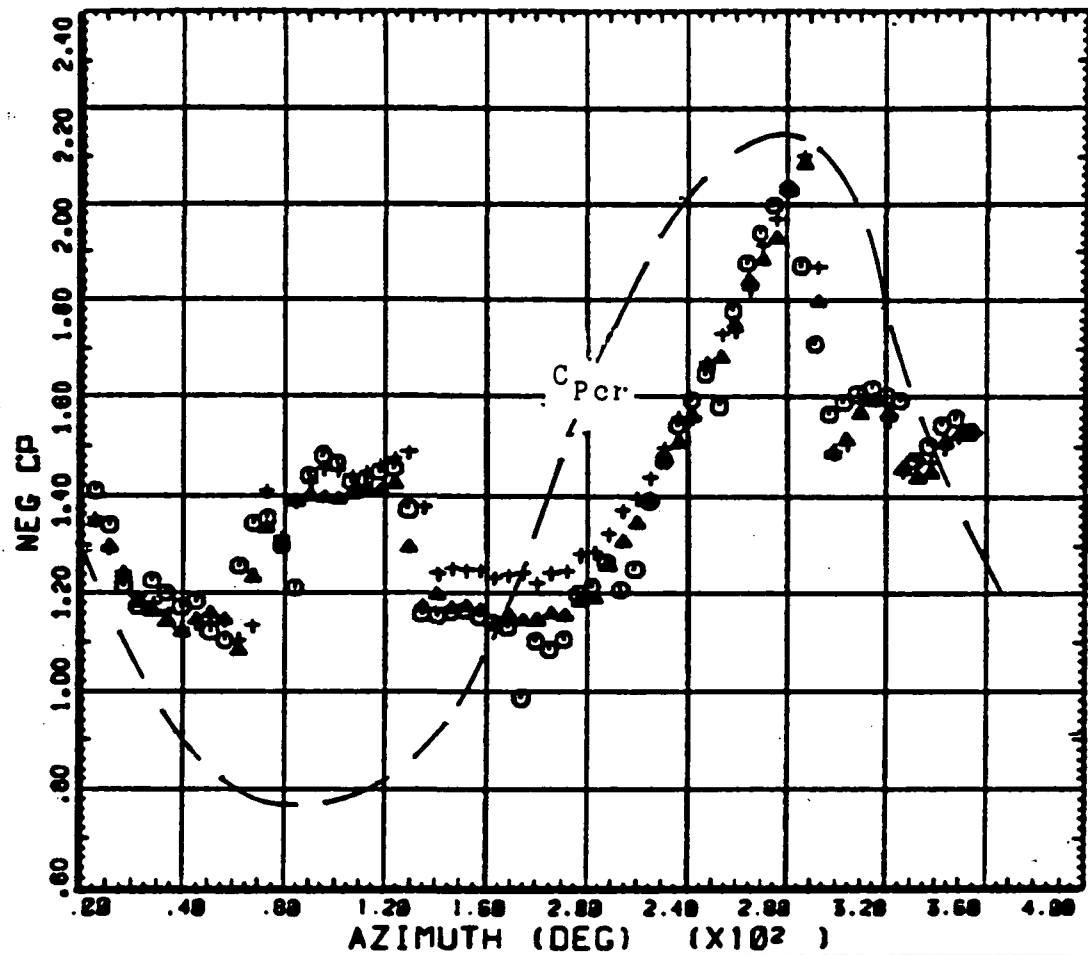


Figure 82. Azimuthal variation of pressure coefficient for 3 different rates of descent. Upper surface, 91 percent radius, 8 percent chord.

ORIGINAL PAGE IS  
OF POOR QUALITY

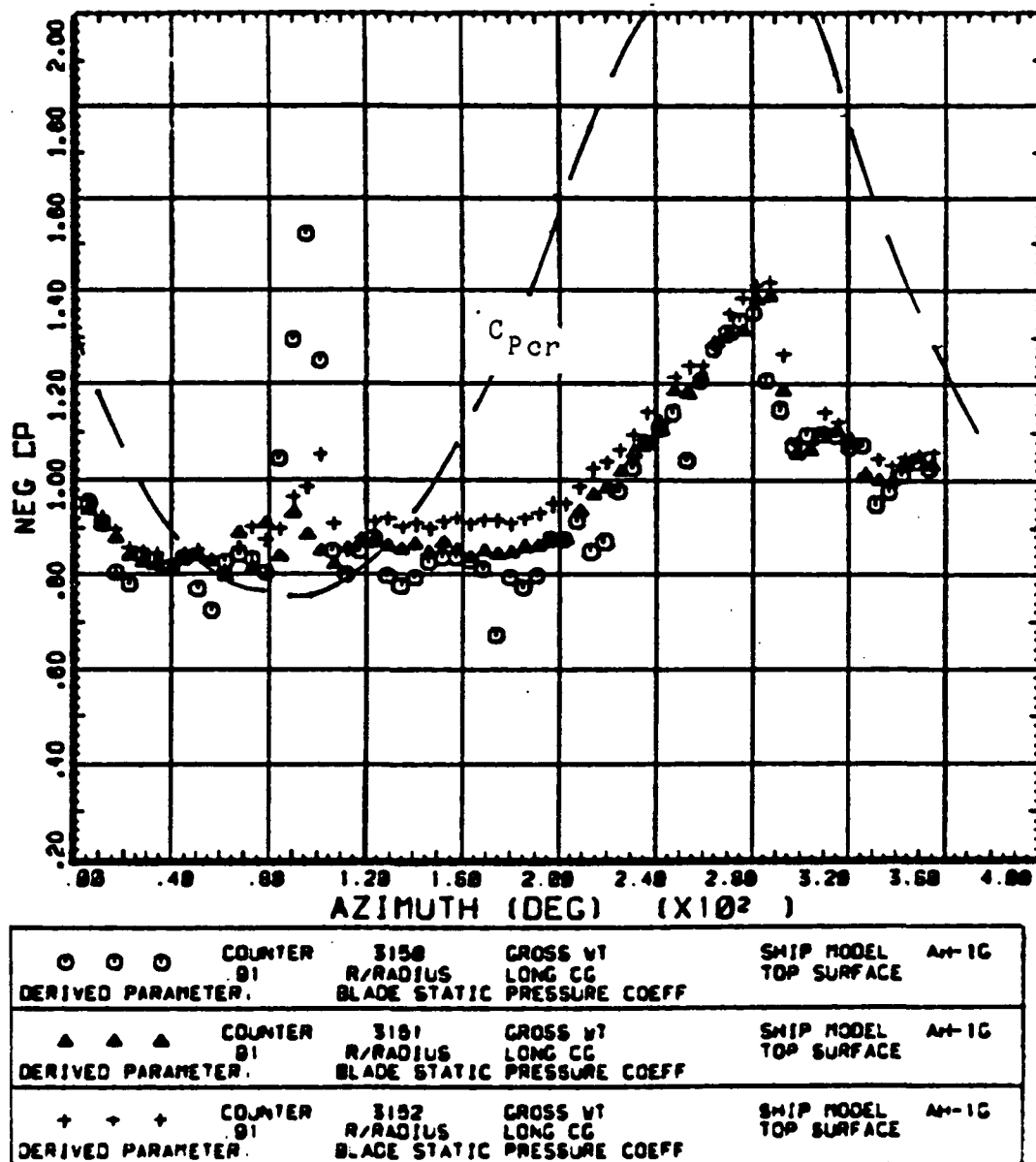
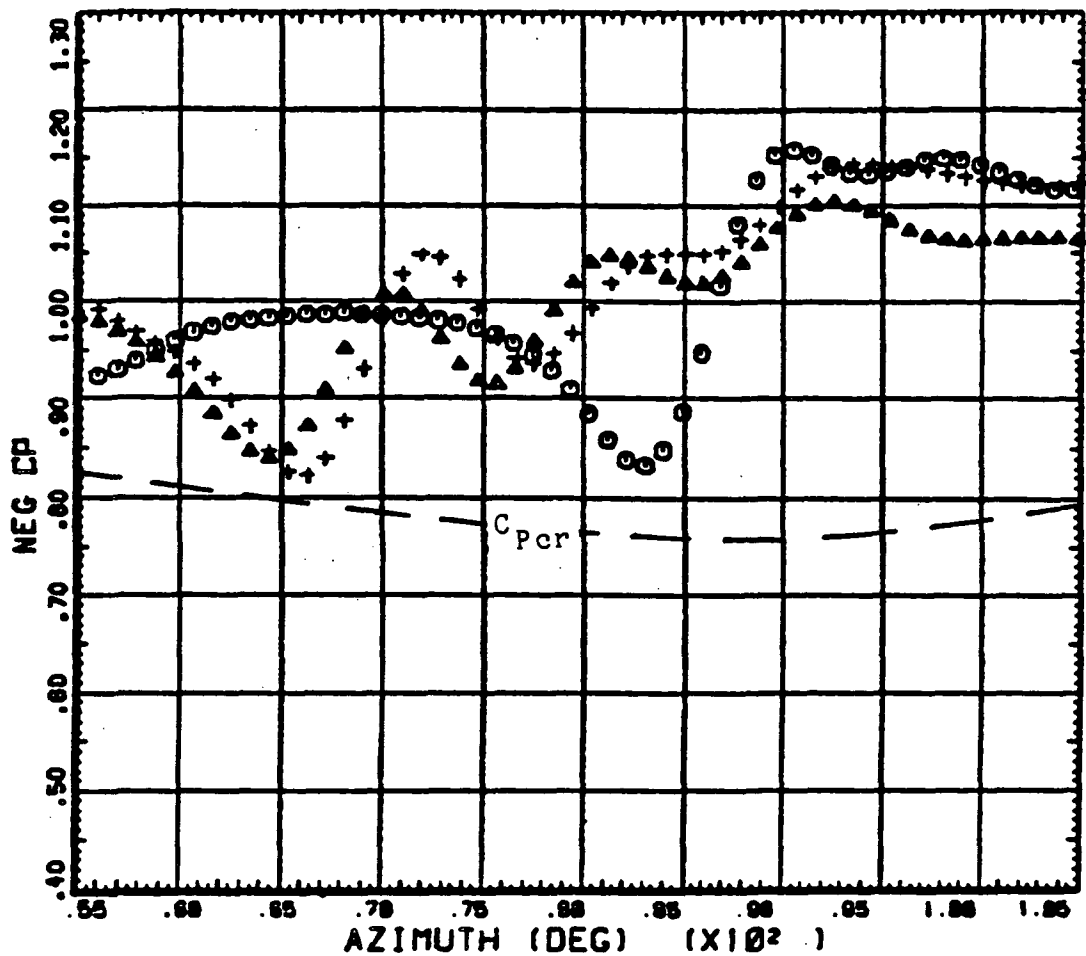


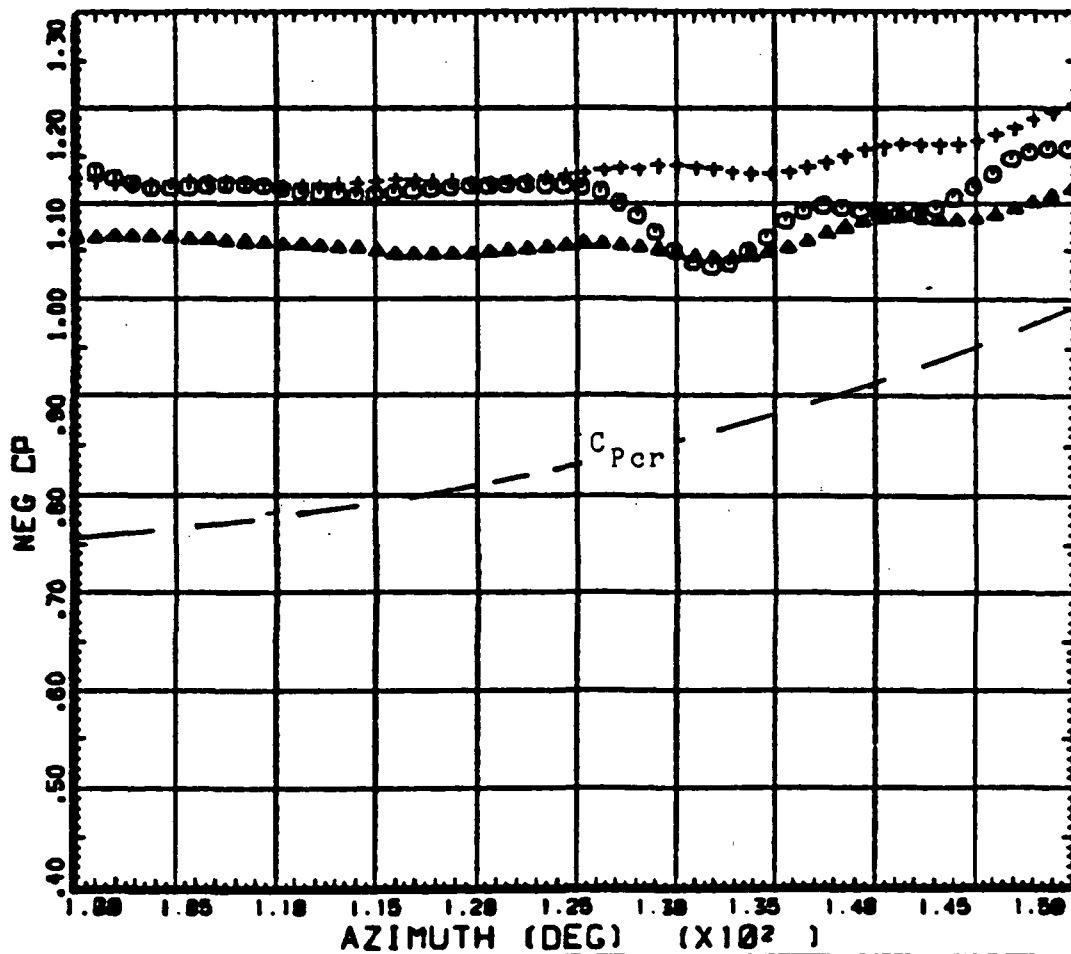
Figure 83. Azimuthal variation of pressure coefficient for 3 different rates of descent. Upper surface, 91 percent radius, 15 percent chord.



○ ○ ○	COUNTER	3188	GROSS VT	SHIP MODEL	AM-1G
DERIVED PARAMETER.	.91	R/RADIUS	LONG CG	TOP SURFACE	
△ △ △	COUNTER	3181	GROSS VT	SHIP MODEL	AM-1G
DERIVED PARAMETER.	.81	R/RADIUS	LONG CG	TOP SURFACE	
+++	COUNTER	3162	GROSS VT	SHIP MODEL	AM-1G
DERIVED PARAMETER.	.81	R/RADIUS	LONG CG	TOP SURFACE	
			BLADE STATIC PRESSURE COEFF		

Figure 84. Azimuthal variation of pressure coefficient for 3 different rates of descent, expanded scale. Upper surface, 91 percent radius, 3 percent chord.

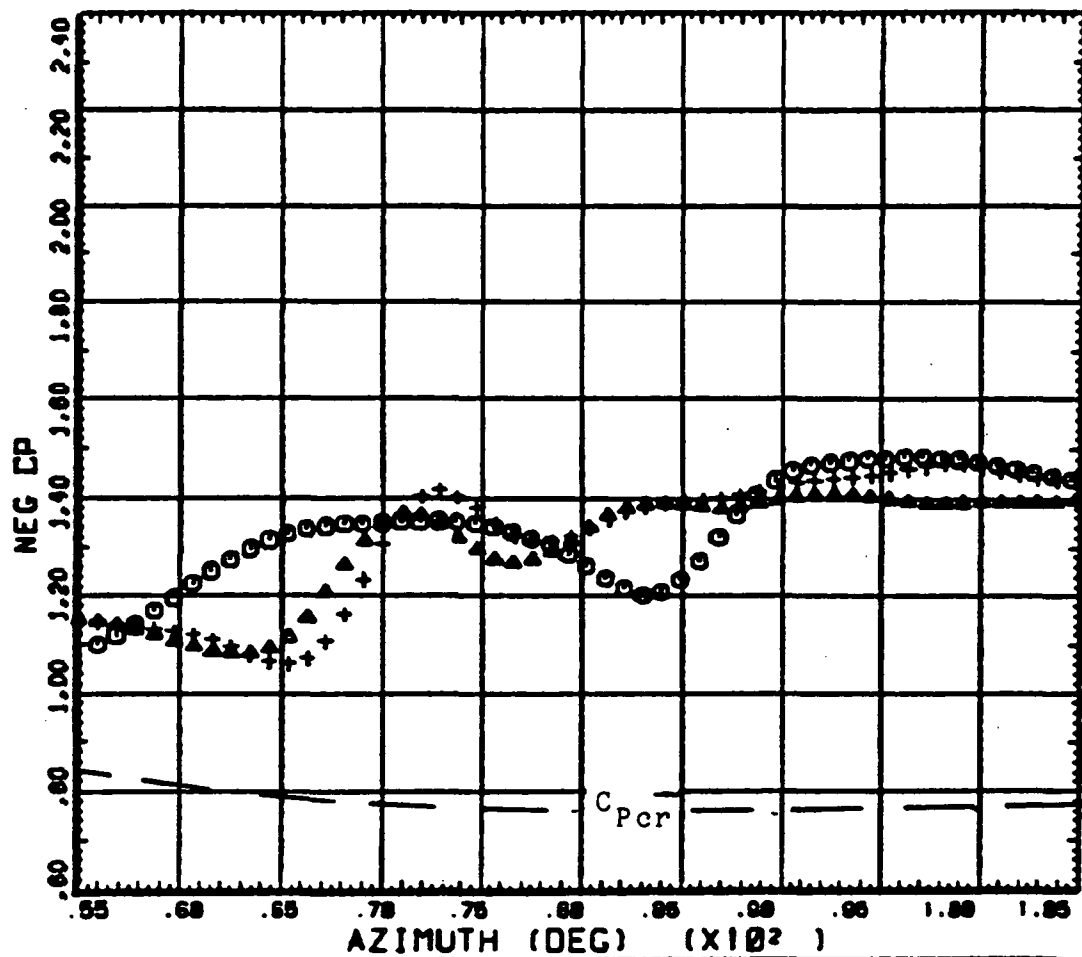
ORIGINAL PAGE IS  
OF POOR QUALITY.



COUNTER		3150	GROSS WT	SHIP MODEL	AM-1G
DERIVED PARAMETER.		R/RADIUS	LONG CG	TOP SURFACE	
COUNTER		3161	GROSS WT	SHIP MODEL	AM-1G
DERIVED PARAMETER.		R/RADIUS	LONG CG	TOP SURFACE	
COUNTER		3162	GROSS WT	SHIP MODEL	AM-1G
DERIVED PARAMETER.		R/RADIUS	LONG CG	TOP SURFACE	

Figure 85. Azimuthal variation of pressure coefficient for 3 different rates of descent, expanded scale. Upper surface, 91 percent radius, 3 percent chord.

ORIGINAL PAGE IS  
OF POOR QUALITY



○ ○ ○	COUNTER 91 DERIVED PARAMETER.	3150 R/RADIUS BLADE STATIC PRESSURE COEFF	GROSS WT LONG CG PRESSURE COEFF	SHIP MODEL AM-1G TOP SURFACE
▲ ▲ ▲	COUNTER 91 DERIVED PARAMETER.	3151 R/RADIUS BLADE STATIC PRESSURE COEFF	GROSS WT LONG CG PRESSURE COEFF	SHIP MODEL AM-1G TOP SURFACE
+ + +	COUNTER 91 DERIVED PARAMETER.	3152 R/RADIUS BLADE STATIC PRESSURE COEFF	GROSS WT LONG CG PRESSURE COEFF	SHIP MODEL AM-1G TOP SURFACE

Figure 86. Azimuthal variation of pressure coefficient for 3 different rates of descent, expanded scale. Upper surface, 91 percent radius, 8 percent chord.

ORIGINAL PAGE IS  
OF POOR QUALITY

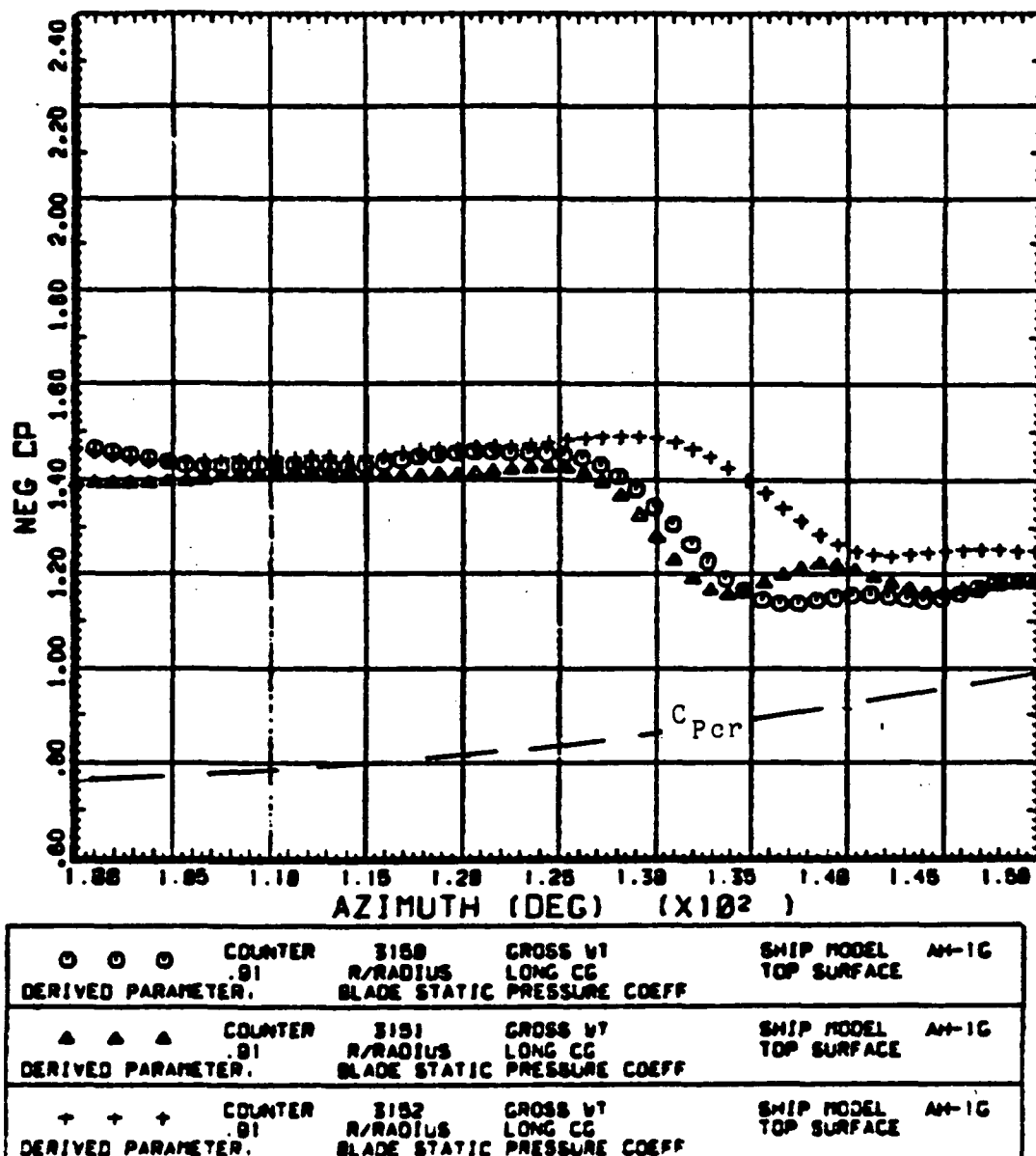
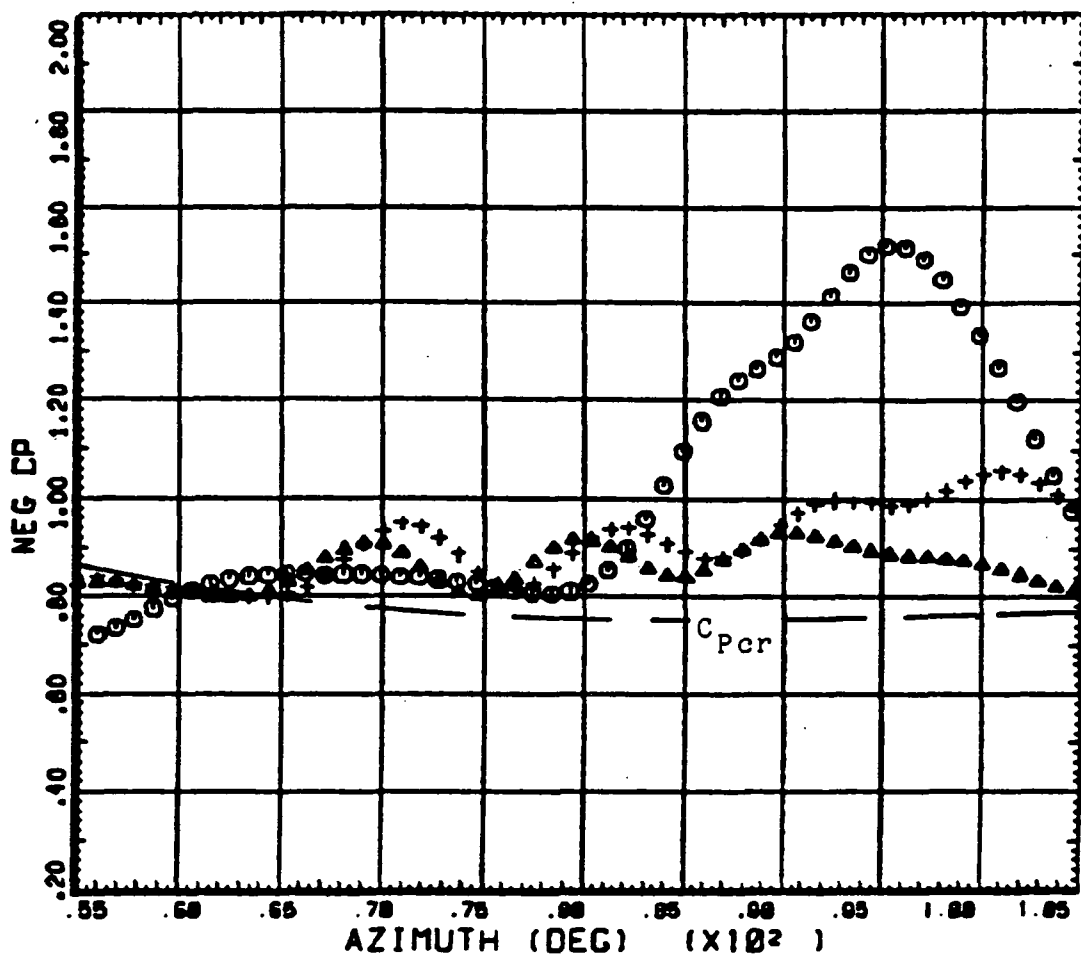


Figure 87. Azimuthal variation of pressure coefficient for 3 different rates of descent, expanded scale. Upper surface, 91 percent radius, 8 percent chord.



○ ○ ○	COUNTER .91 DERIVED PARAMETER.	3150 R/RADIUS BLADE STATIC PRESSURE COEFF	GROSS WT LONG CG	SHIP MODEL AH-1G TOP SURFACE
▲ ▲ ▲	COUNTER .91 DERIVED PARAMETER.	3151 R/RADIUS BLADE STATIC PRESSURE COEFF	GROSS WT LONG CG	SHIP MODEL AH-1G TOP SURFACE
+ + +	COUNTER .91 DERIVED PARAMETER.	3152 R/RADIUS BLADE STATIC PRESSURE COEFF	GROSS WT LONG CG	SHIP MODEL AH-1G TOP SURFACE

Figure 88. Azimuthal variation of pressure coefficient for 3 different rates of descent, expanded scale. Upper surface, 91 percent radius, 15 percent chord.

ORIGINAL PAGE IS  
OF POOR QUALITY

ORIGINAL PAGE IS  
OF POOR QUALITY

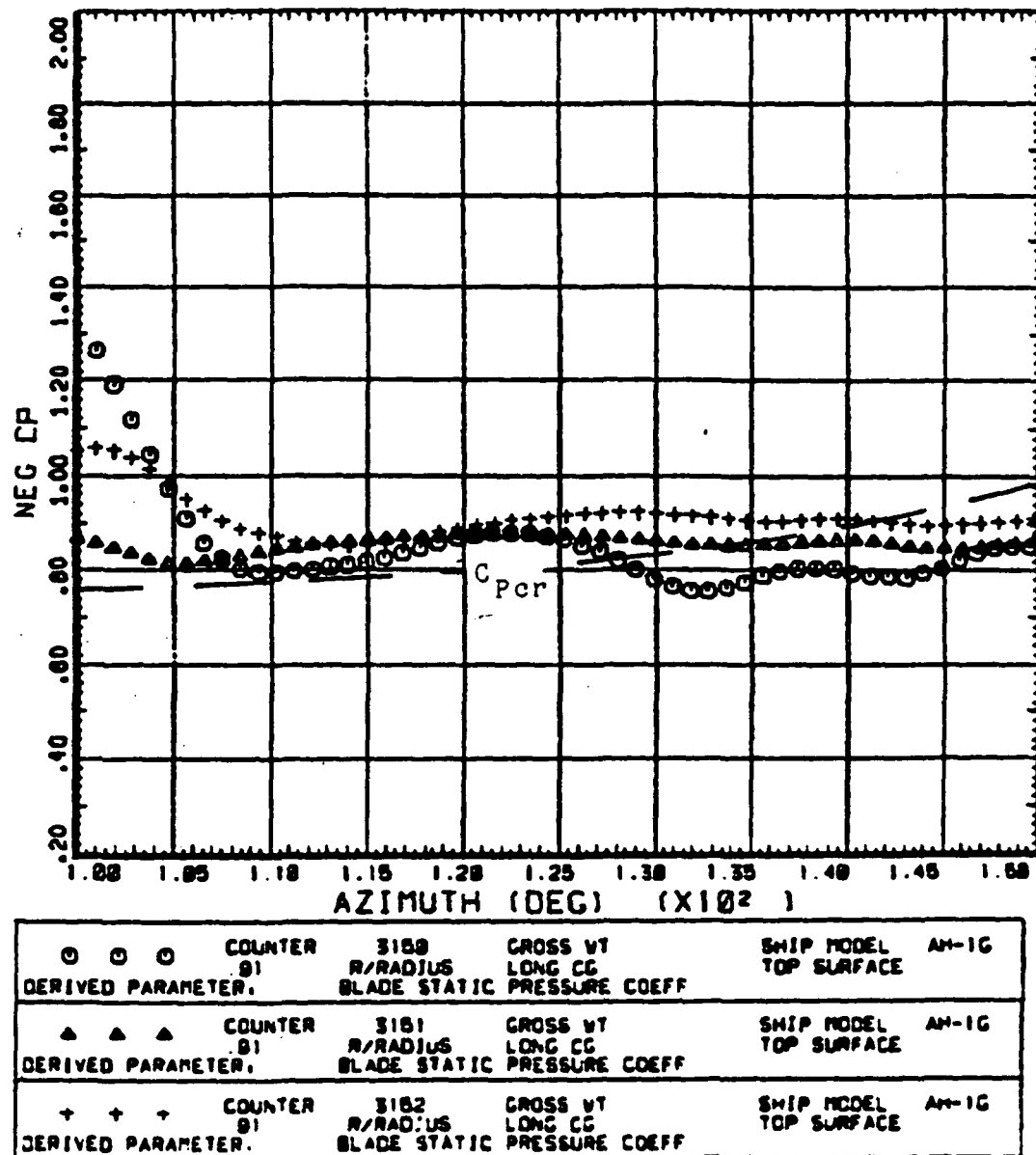
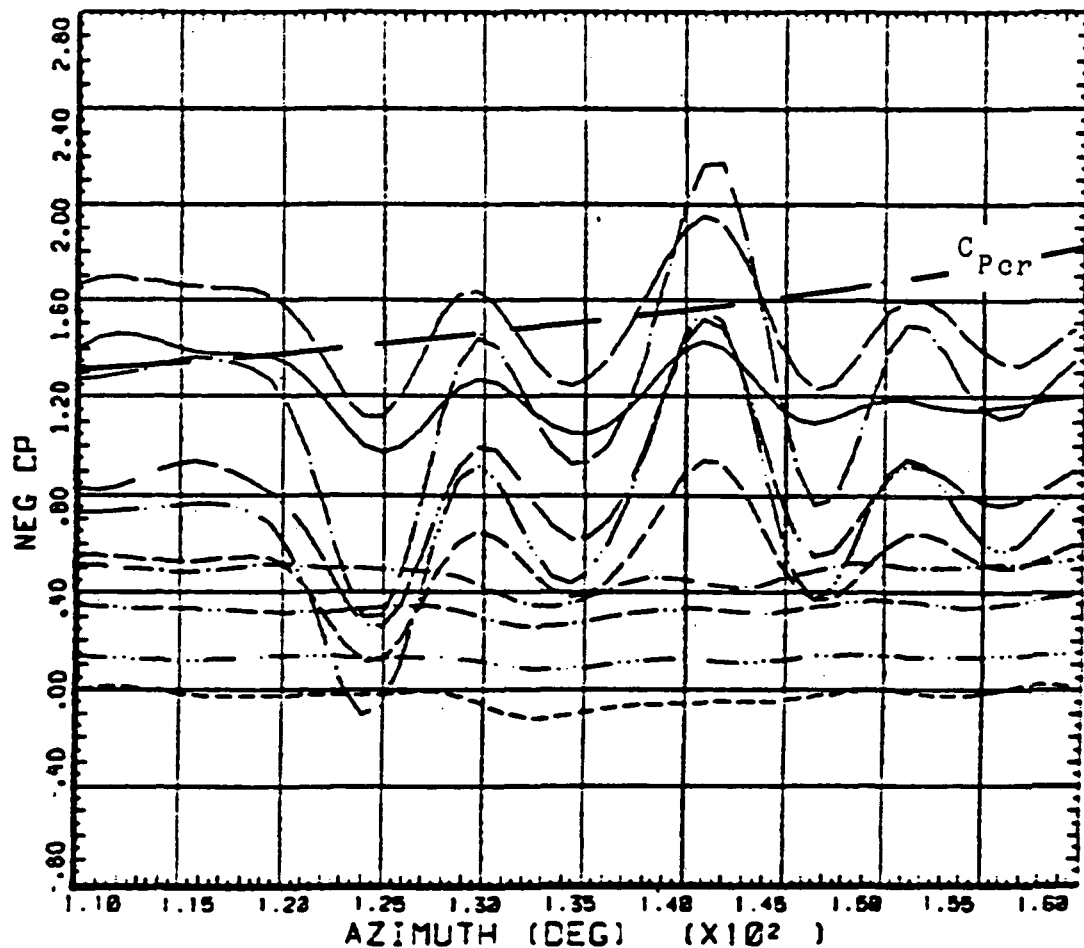


Figure 89. Azimuthal variation of pressure coefficient for 3 different rates of descent, expanded scale. Upper surface, 91 percent radius, 15 percent chord.



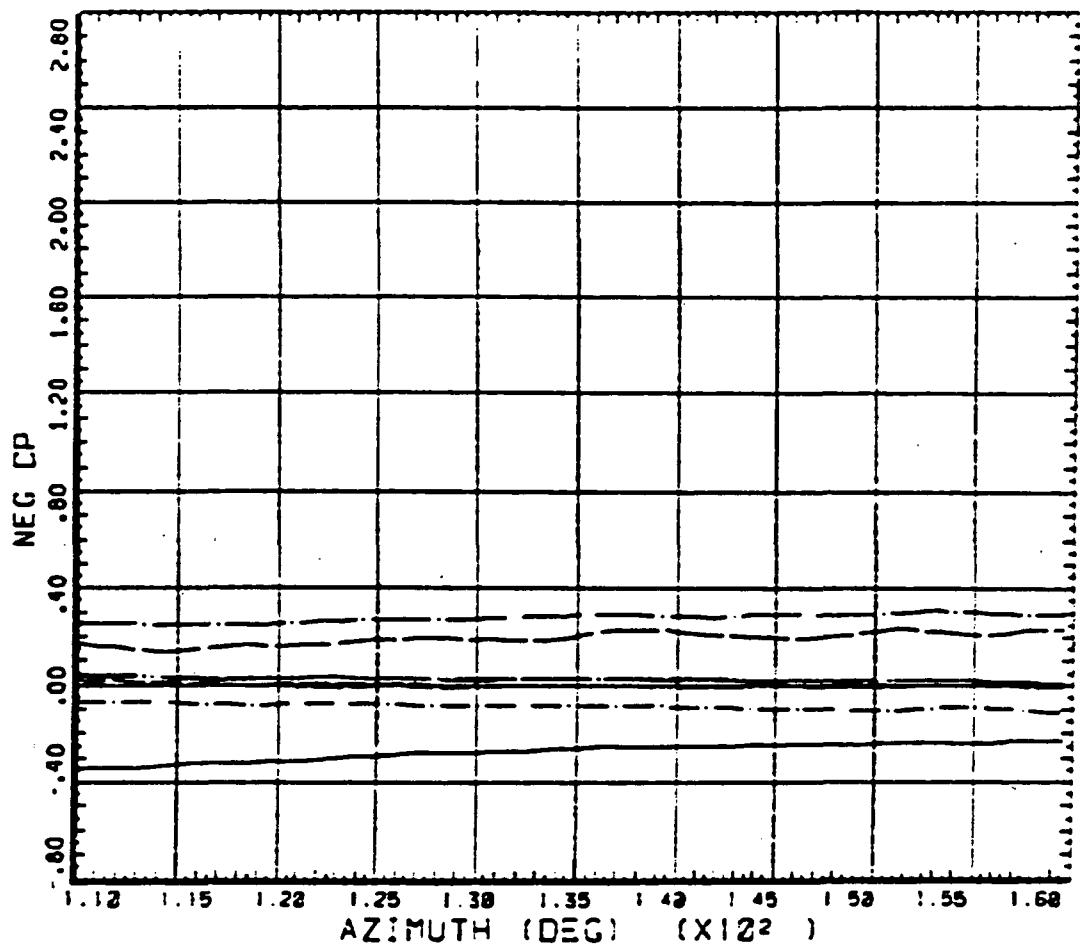
DERIVED PARAMETER: BLADE STATIC PRESSURE CCEFF

COUNTER 75	R/RADIUS 3158	CROSS WT LONG CS	SHIP MODEL OP SURFACE	AM-10
81	X/CHORD	---	---	55 X/C-CHD
23	X/CHORD	---	---	73 X/C-CHD
28	X/CHORD	---	---	92 X/C-CHD
19	X/CHORD	---	---	
29	X/CHORD	---	---	
35	X/CHORD	---	---	
42	X/CHORD	---	---	

Figure 90. Azimuthal variation of pressure coefficient for all chordwise stations. Upper surface, 75 percent radius, level flight.

ORIGINAL PAGE IS  
OF POOR QUALITY

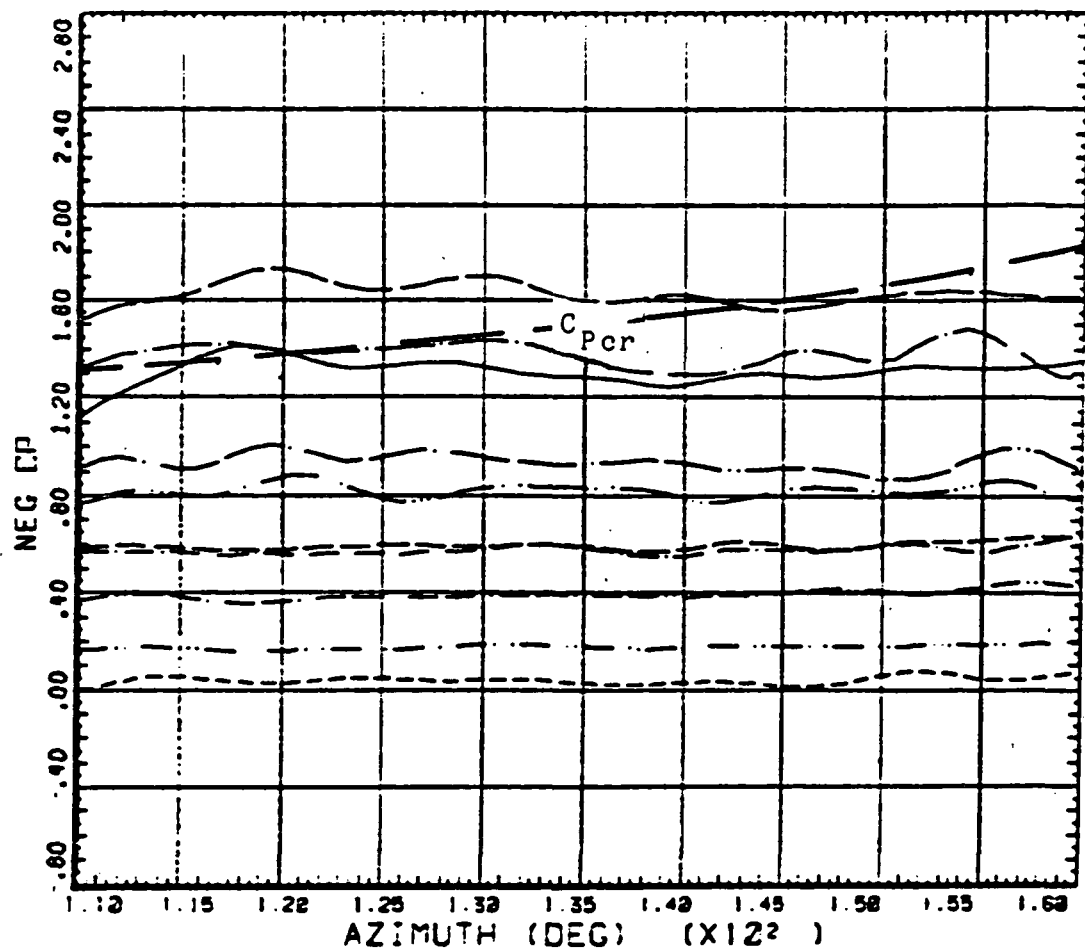
ORIGINAL PAGE IS  
OF POOR QUALITY



DERIVED PARAMETER: BLADE STATIC PRESSURE COEFF

COUNTER 75	3150 R/RADIUS	CROSS WT LEVEL CC	S-1 P T-DEL A-1 G BOT SURFACE	92 X/C-HCPC
23	X/C-HCPC			
28	X/C-HCPC			
15	X/C-HCPC			
42	X/C-HCPC			
45	X/C-HCPC			
55	X/C-HCPC			
72	X/C-HCPC			

Figure 91. Azimuthal variation of pressure coefficient for all chordwise stations. Lower surface, 75 percent radius, level flight.



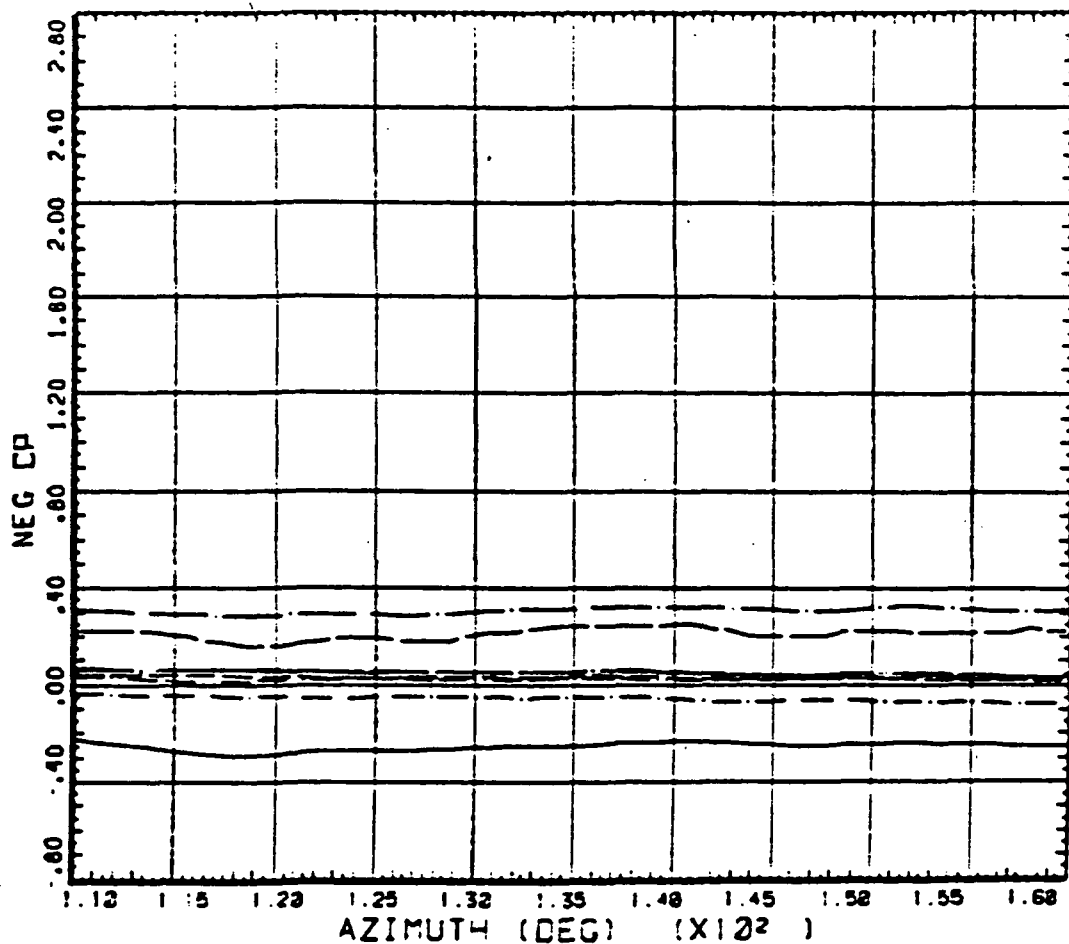
DERIVED PARAMETER: BLADE STATIC PRESSURE CCEFF

CHORD STATION	R/RADIUS	CROSS WT LONG CS	SHIP MODEL	AM-1G
75	3152			
.81	X/CHORD		69	X/CHORD
.83	X/CHORD		70	X/CHORD
.88	X/CHORD		82	X/CHORD
.95	X/CHORD			
25	X/CHORD			
35	X/CHORD			
43	X/CHORD			

Figure 92. Azimuthal variation of pressure coefficient for all chordwise stations. Upper surface, 75 percent radius, 400 fpm rate of descent.

ORIGINAL PAGE IS  
OF POOR QUALITY

ORIGINAL PAGE IS  
OF POOR QUALITY.

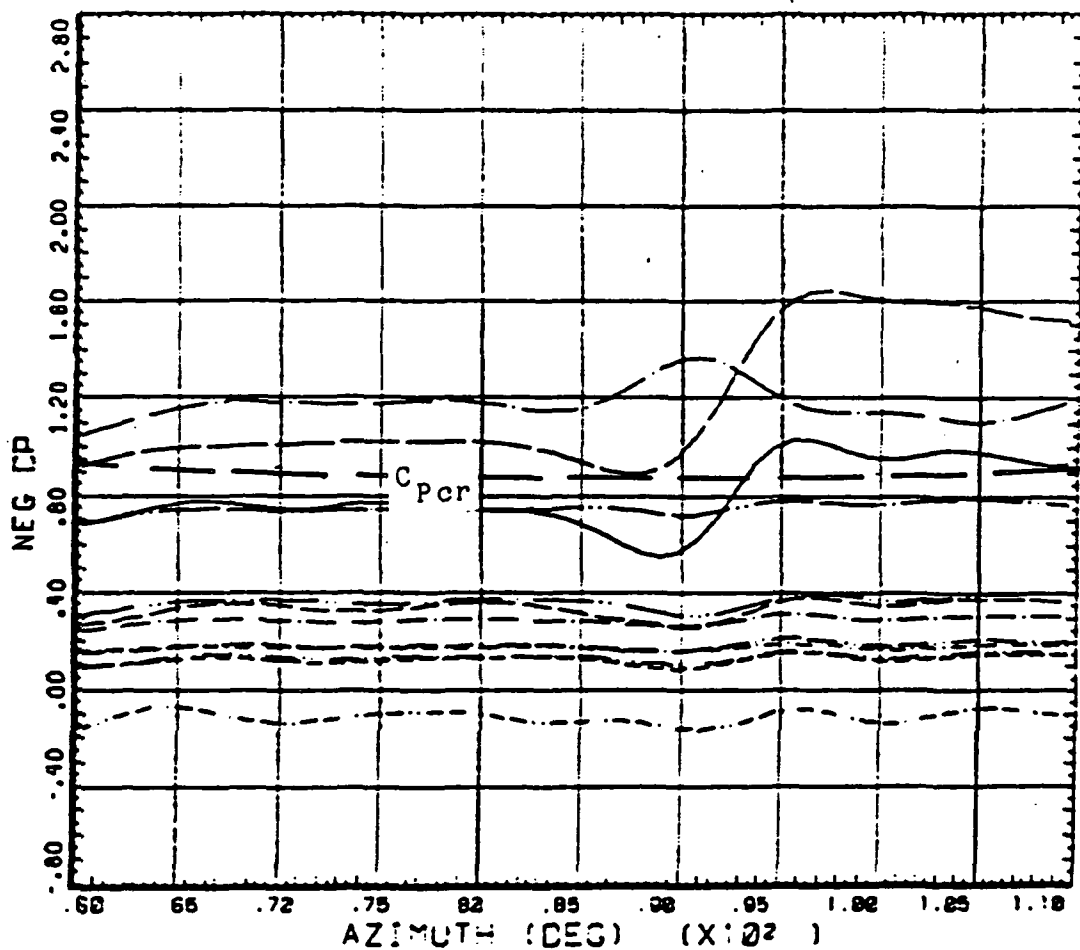


DERIVED PARAMETER: BLADE STATIC PRESSURE CCEFF

CHORD 75	R/RADIUS 3.52	CROSS WT LNG CC	SHIP ACCEL BCY'30° SURFACE AH-16 82 X/CHORD
		.23	X/CHORD
		.28	X/CHORD
		.5	X/CHORD
		.48	X/CHORD
		.45	X/CHORD
		.55	X/CHORD
		.70	X/CHORD

Figure 93. Azimuthal variation of pressure coefficient for all chordwise stations. Lower surface, 75 percent radius, 400 fpm rate of descent.

ORIGINAL PAGE IS  
OF POOR QUALITY

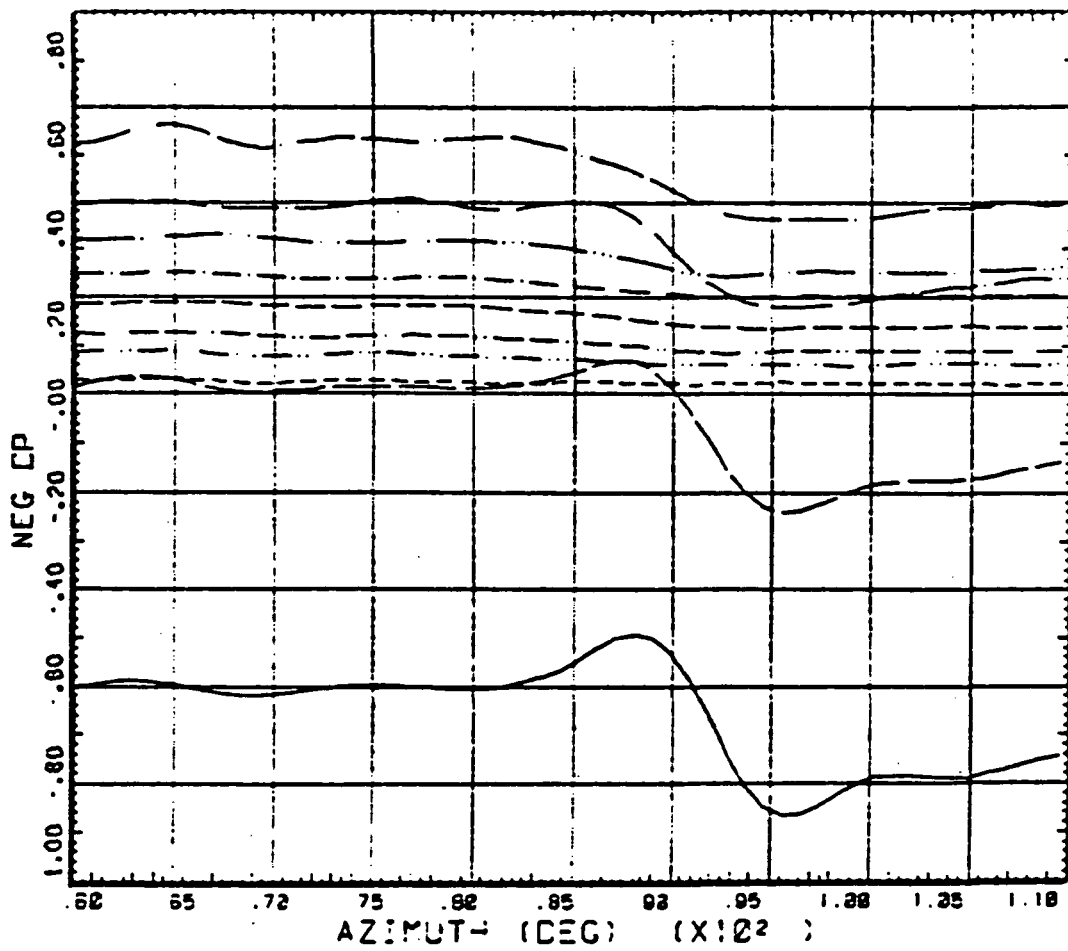


DERIVED PARAMETER: BLADE STATIC PRESSURE COEFF

CHORD 86	3150 R/RADIUS	CROSS WT LONG CC	SP/C <sub>P</sub> COEF C <sub>P</sub> SURFACE	AM-1G
—	23	X/CHCRD	—	58 X/CHCRD
—	28	X/C-OPC	—	59 X/CHCRD
—	15	X/C-OPC	—	63 X/CHCRD
—	25	X/C-OPC	—	78 X/CHCRD
—	39	X/C-OPC	—	92 X/CHCRD
—	40	X/C-OPC	—	
—	45	X/CHCRD	—	

Figure 94. Azimuthal variation of pressure coefficient for all chordwise stations. Upper surface, 86 percent radius, level flight.

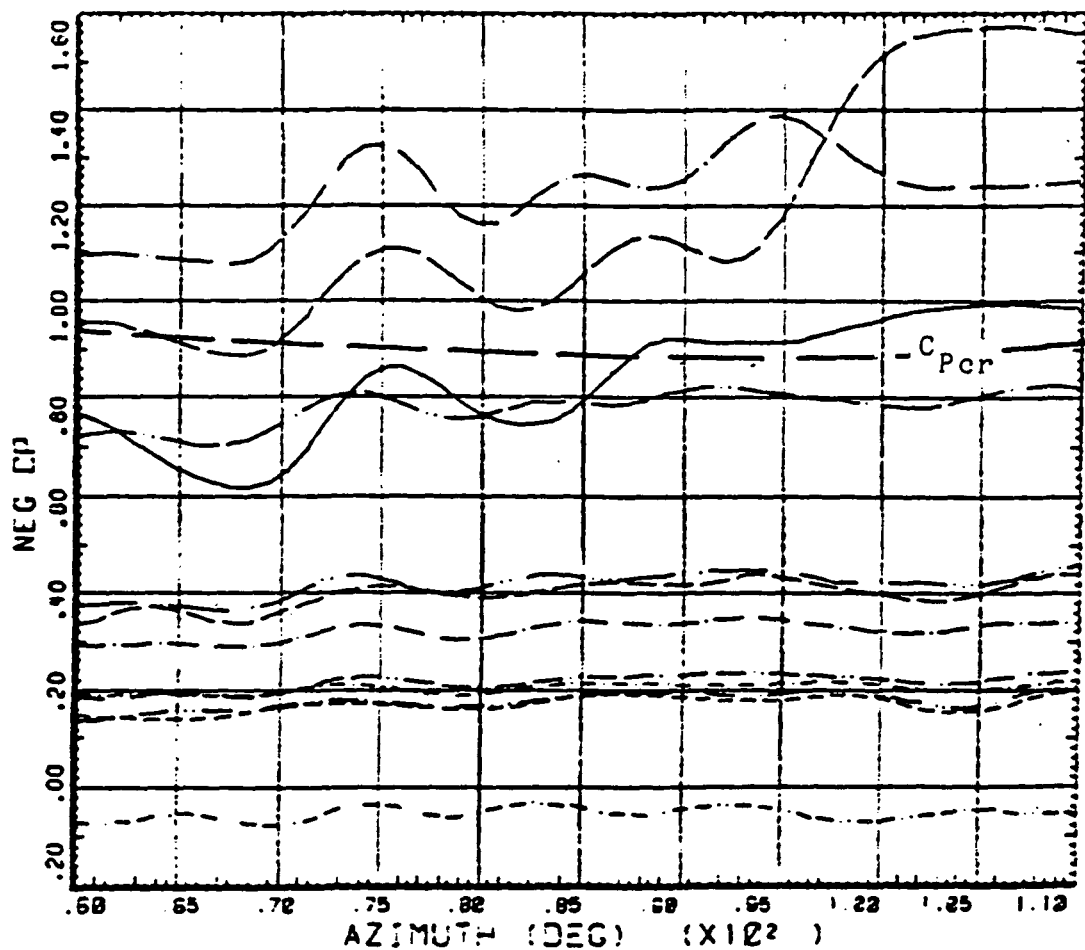
ORIGINAL PAGE IS  
OF POOR QUALITY



DERIVED PARAMETER: BLADE STATIC PRESSURE COEFF

CHORD 86	R/RADIUS 3.58	CROSS WT -CNC CC	S-1P MODEL BOT CH SURFACE	AN-1G
		21 X/CHORD	55 X/CHORD	
		23 X/CHORD	73 X/CHORD	
		29 X/CHORD	92 X/CHORD	
		15 X/C-CHORD		
		35 X/C-CHORD		
		45 X/C-CHORD		
		53 X/C-CHORD		

Figure 95. Azimuthal variation of pressure coefficient for all chordwise stations. Lower surface, 86 percent radius, level flight.



### DERIVED PARAMETER

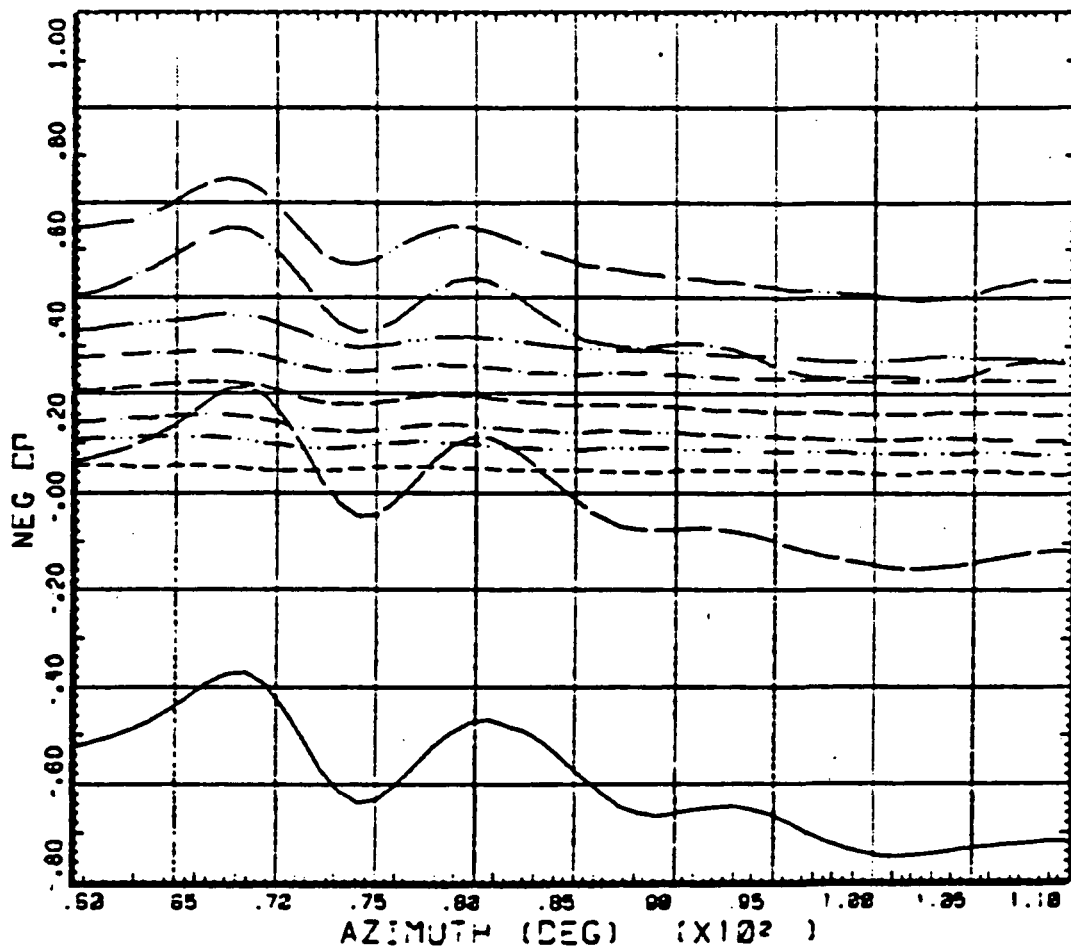
### BLADE STATIC PRESSURE COEFF

CO- UNTER 86	3152 R/RADIUS	GROSS W <sup>2</sup> 3000 CS	SHIP MODE OP SURFACE	AH-10
	33	X/CHORD	—	.53 X/CHORD
	29	X/CHORD	—	.55 X/CHORD
	15	X/CHORD	-----	.68 X/CHORD
	25	X/CHORD	—	.78 X/CHORD
	35	X/C-CHORD	—	.92 X/C-CHORD
	43	X/C-CHORD		
	45	X/C-CHORD		

Figure 96. Azimuthal variation of pressure coefficient for all chordwise stations. Upper surface, 86 percent radius, 400 fpm rate of descent.

ORIGINAL PAGE IS  
OF POOR QUALITY

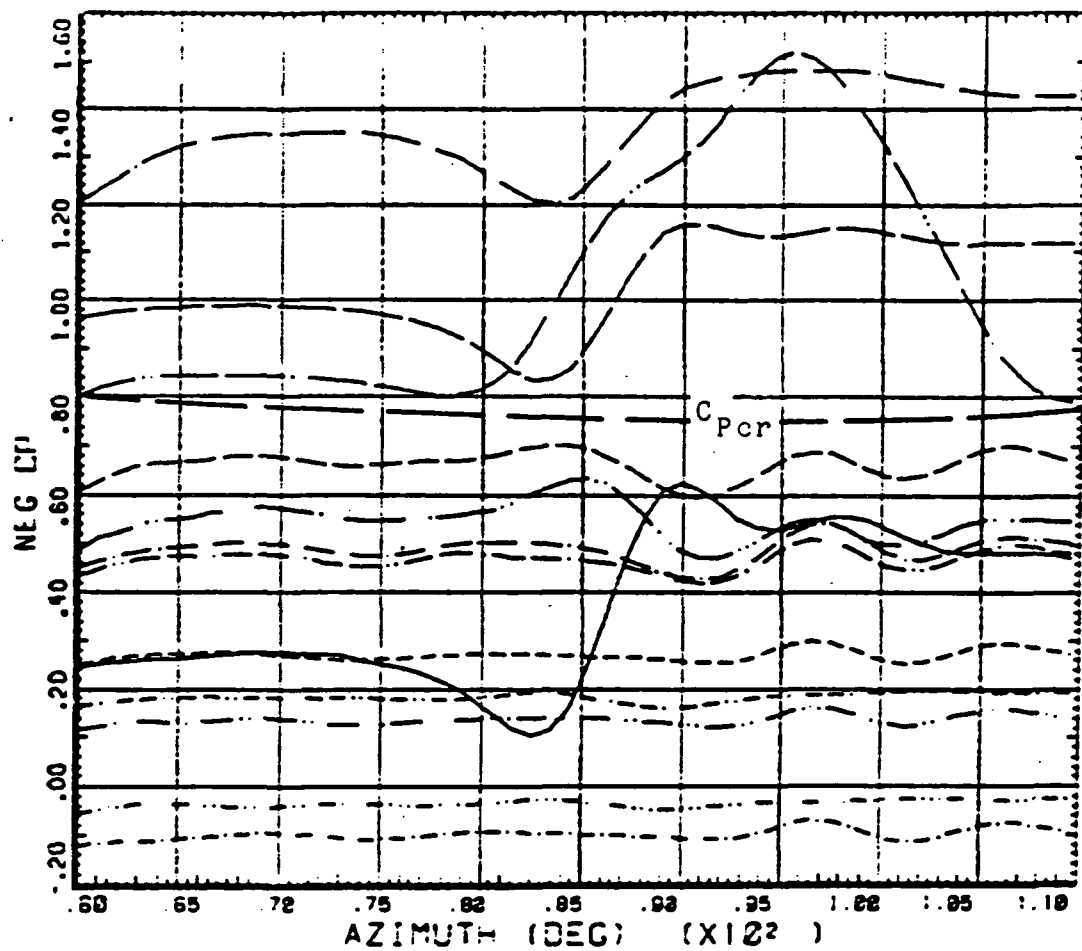
ORIGINAL PAGE IS  
OF POOR QUALITY



DERIVED PARAMETER: SLADE STATIC PRESSURE COEFF

COUNTER 86	3.52 R/RADIUS	CROSS WT LONG CC	SHIP MODEL BOTTOM SURFACE	AN-15
81	X/C-0RC	—	55	X/C-0RC
83	X/C-0RC	—	78	X/C-0RC
28	X/C-0RC	—	92	X/C-0RC
19	X/C-0RC	—		
35	X/C-0RC	—		
45	X/C-0RC	—		
53	X/C-0RC	—		

Figure 97. Azimuthal variation of pressure coefficient for all chordwise stations. Lower surface, 86 percent radius, 400 fpm rate of descent.



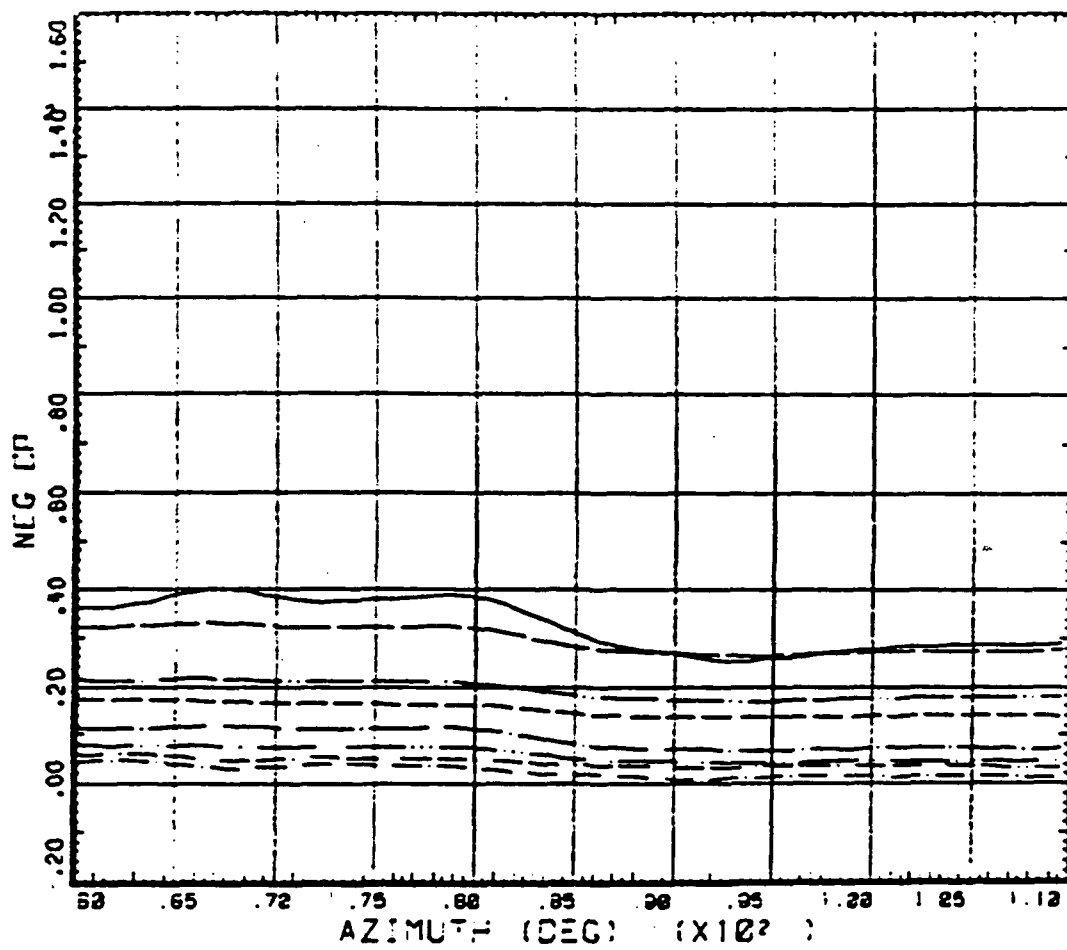
### DERIVED PARAMETER: BLADE STATIC PRESSURE COEFF

COUNTER #	3'92 R/RADIUS	GROSS WT LONG CC	S-IP MCCEL "CP SURFACE	AM-15
—	.81	X/C-0920	—	.48
—	.33	X/C-0920	—	.45
—	.28	X/C-0920	—	.98
—	.15	X/C-0920	—	.55
—	.22	X/C-0920	—	.62
—	.25	X/C-0920	—	.72
—	.35	X/C-0920	—	

Figure 98. Azimuthal variation of pressure coefficient for all chordwise stations. Upper surface, 91 percent radius, level flight.

ORIGINAL PAGE IS  
OF POOR QUALITY

ORIGINAL PAGE IS  
OF POOR QUALITY

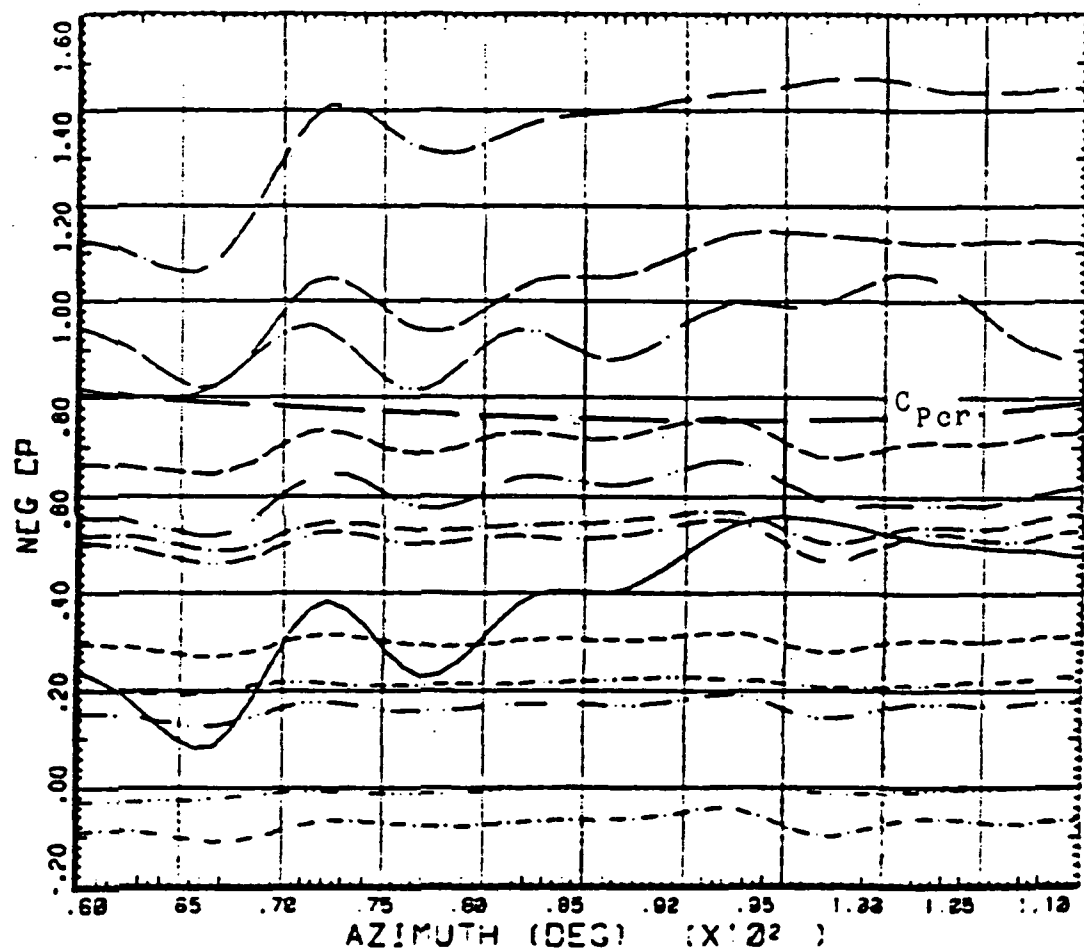


## DERIVED PARAMETER

## BLADE STATIC PRESSURE COEFF

COUNTER #	3153 #/RADIUS	CROSS WT LONG CO	SHIP MODEL 8011CT SURFACE	AH-1C
—	28	X/CHORD	—	73 X/CHORD
—	35	X/CHORD	—	—
—	42	X/CHORD	—	—
—	45	X/CHORD	—	—
—	53	X/C-CHORD	—	—
—	55	X/C-CHORD	—	—
—	63	X/CHORD	—	—

Figure 99. Azimuthal variation of pressure coefficient for all chordwise stations. Lower surface, 91 percent radius, level flight.



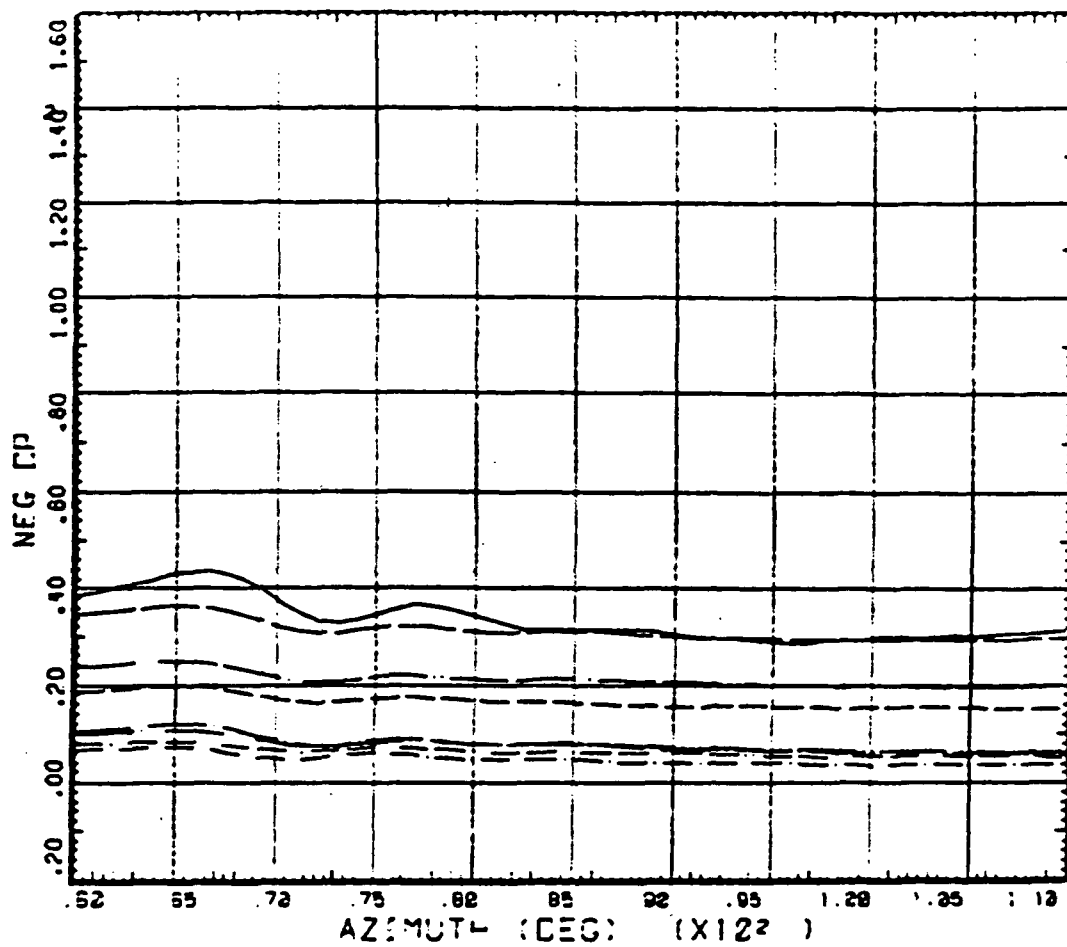
DERIVED PARAMETER: BLADE STATIC PRESSURE COEFF

CHORD STATION	R/RADIUS	CROSS WT LONG CG	SHIP MODEL	AM-1G
21	X/C-0RC	---	43	X/C-0RC
23	X/C-0RC	---	45	X/C-0RC
28	X/C-0RC	---	53	X/C-0RC
31	X/C-0RC	---	55	X/C-0RC
22	X/C-0RC	---	62	X/C-0RC
25	X/C-0RC	---	78	X/C-0RC
35	X/C-0RC	---		

Figure 100. Azimuthal variation of pressure coefficient for all chordwise stations. Upper surface, 91 percent radius, 400 fpm rate of descent.

ORIGINAL PAGE IS  
OF POOR QUALITY

ORIGINAL PAGE IS  
OF POOR QUALITY



DERIVED PARAMETER: BLADE STATIC PRESSURE COEFF

COUNTER #	3.52 R/RADIUS	CROSS WT LNG CS	SP-IP COEF BOTTOM SURFACE	AM-15 78 X/CHORD
28		X/CHORD		
34		X/CHORD		
40		X/CHORD		
46		X/CHORD		
52		X/CHORD		
58		X/CHORD		
64		X/CHORD		

Figure 101. Azimuthal variation of pressure coefficient for all chordwise stations. Lower surface, 91 percent radius, 400 fpm rate of descent.

1. Report No. CR 177435	2. Government Accession No.	3. Recipient's Catalog No.	
4. Title and Subtitle  Investigation of Helicopter Rotor Blade/Wake Interaction Impulsive Noise		5. Report Date January 1987	
7. Author(s) S. J. Miley, G. F. Hall, E. von Lavante		6. Performing Organization Code	
9. Performing Organization Name and Address  Texas A & M University College Station, Texas 77843		8. Performing Organization Report No.	
12. Sponsoring Agency Name and Address  National Aeronautics and Space Administration Washington, D. C. 20546		10. Work Unit No.	
		11. Contract or Grant No. NCA2-OR773-301	
		13. Type of Report and Period Covered Contractor Report	
		14. Sponsoring Agency Code 505-61-51	
15. Supplementary Notes  Point of Contact: Technical Monitor, Michael E. Watts, M/S 237-5 Ames Research Center, Moffett Field, CA 94035			
16. Abstract  An analysis of the Tip Aerodynamic/Aeroacoustic Test (TAAT) data was performed to identify possible aerodynamic sources of blade/vortex interaction (BVI) impulsive noise. The identification is based upon correlation of measured blade pressure time histories with predicted blade/vortex intersections for the flight condition(s) where impulsive noise was detected. Due to the location of the recording microphones, only noise signatures associated with the advancing blade were available, and the analysis was accordingly restricted to the first and second azimuthal quadrants.  The results show that the blade tip region is operating transonically in the azimuthal range where previous BVI experiments indicated the impulsive noise source to be. No individual blade/vortex encounter is identifiable in the pressure data, however, there is indication of multiple intersections in the roll-up region which could be the origin of the noise. Discrete blade/vortex encounters are indicated in the second quadrant, however, if impulsive noise was produced here, the directivity pattern would be such that it was not recorded by the microphones. It is demonstrated that the TAAT data base is valuable resource in the investigation of rotor aerodynamic/aeroacoustic behavior, particularly when coupled with suitable analytical models.			
17. Key Words (Suggested by Author(s)) Blade Vortex Interaction, Helicopter, Rotorywing TAAT Noise	18. Distribution Statement Unclassified - Unlimited  Subject category - 02		
19. Security Classif. (of this report) Unclassified	20. Security Classif. (of this page) Unclassified	21. No. of Pages	22. Price*